Spring 2013

Processing, microstructural evolution and electrochemical performance relationships in solid oxide fuel cells

Ayhan Sarikaya

Department: Materials Science and Engineering

PROCESSING, MICROSTRUCTURAL EVOLUTION AND ELECTROCHEMICAL PERFORMANCE RELATIONSHIPS IN SOLID OXIDE FUEL CELLS

by

AYHAN SARIKAYA

A DISSERTATION

Presented to the Faculty of the Graduate School of the

MISSOURI UNIVERSITY OF SCIENCE AND TECHNOLOGY

In Partial Fulfillment of the Requirements for the Degree

DOCTOR OF PHILOSOPHY

in

MATERIALS SCIENCE AND ENGINEERING

2013

Approved by:

Fatih Dogan, Advisor
Wayne Huebner
William G. Fahrenholtz
Matthew J. O'Keefe
Yangchuan Xing

PUBLICATION DISSERTATION OPTION

The Introduction and Background sections of this dissertation provide information about the research background and a review of the literature. The body of this dissertation has been compiled in the format for publication in peer-reviewed journals. Five papers have been included in the following order. The first paper, "Influence of the Microstructural Evolution on the Electrochemical Performance of LSM-YSZ Composite Cathodes for High Performance Solid Oxide Fuel Cells" was submitted to *Journal of Electroceramics*. The second paper, "Silver Composites as Highly Stable Cathode Current Collectors for Solid Oxide Fuel Cells" was published in the *Journal of Materials Research* in August 2012 in Volume 27 Issue 15 (*Focus Issue on Advanced Materials for Fuel Cells*) pages 2024 - 2029. The third paper, "Silver Based Perovskite Nanocomposites as Combined Cathode and Current Collector Layers for Solid Oxide Fuel Cells" was published in the *Journal of the Electrochemical Society* in August 2012 in Volume 159 Issue 11 pages F665-F669. The fourth paper, "Effect of Various Pore Formers on the Microstructural Development of Tape-cast Porous Ceramics" was published in *Ceramics International* in January 2013 in Volume 39 pages 403-413. The fifth paper, "Development of the Anode Pore Structure and Its Effects on the Performance of Solid Oxide Fuel Cells" was submitted to the *International Journal of the Hydrogen Energy*.

Other three parts related to the present study but not included in the body of this dissertation are given in the appendix. The first part is a paper entitled "Development of a Silver Based Stable Current Collector for Solid Oxide Fuel Cell Cathodes" published in the *Materials Research Society Symposium Proceedings* in 2012 in Volume 1385 pages

c07-10. The second part is a paper entitled “Effect of the Anode Microstructure on the Enhanced Performance of Solid Oxide Fuel Cells” published in the *International Journal of the Hydrogen Energy* in June 2012 in Volume 37 pages 11370-11377. The third part is about the extended investigations on the high temperature stability of powder-based and infiltrated nanostructured Ag composites.

ABSTRACT

The relationships between the processing parameters, microstructures and electrochemical performance of solid oxide fuel cell (SOFC) components were investigated. The operating regimes (i.e., reducing vs. oxidizing) as well as the elevated temperatures (e.g. 800^{o}C) for their operation introduce several material challenges. Therefore, composite materials are employed to withstand operating conditions while providing sufficient electrochemical performance for fuel cell operation.

Analyses on lanthanum-strontium manganite (LSM) – yttria stabilized zirconia (YSZ) compositions (45 vol%-55 vol%) by impedance spectroscopy demonstrated that two competing polarization mechanisms (i.e. charge-exchange and surface adsorption-diffusion of oxygen) limit performance. Optimization of microstructures resulted in total resistances as low as 0.040 Ohm cm^2. Studies on Ag composites revealed that incorporation of up to 25 vol% oxide particles (LSM and YSZ) with sizes comparable to the Ag grains (~0.5 μm) can minimize the densification and coarsening of the Ag matrix. While the powder based oxide additions increased the stability limit of porous Ag composites from <550°C to 800^{o}C, the use of nanostructured coatings increased the stability limit to 900^{o}C for cathodes and current collectors. Investigations of Ni-YSZ anode microstructures demonstrated that uniform distribution of percolating isometric pores (>5 μm) allows forming desired continuous percolation of all phases (Ni, YSZ and pores) lowering activation polarization below 0.100 Ohm cm^2 and maintaining significant electrical conductivity (>1000 S/cm). Identification of polarization mechanisms by deconvolution of impedance spectra and tailoring the corresponding microstructures was demonstrated as an effective method for optimization of SOFC components.

ACKNOWLEDGEMENTS

I would like to thank my advisor, Dr. Fatih Dogan, for his advice, encouragement and guidance for this study. It was a great opportunity for me to work in his research group to develop a strong academic background. He created great occasions and support for me to go to technical conferences and meetings which allowed me to develop strong ties with the ceramic and solid-state electrochemistry communities.

I would like to acknowledge Dr. Wayne Huebner for his inspiration, mentorship and continuous support throughout my course work and Ph.D. study. I would also like to thank my committee members: Dr. William G. Fahrenholtz, Dr. Matthew J. O'Keefe and Dr. Yangchuan Xing for their valuable input and stimulation in spite of their busy schedules.

I owe special thanks to Dr. Vladimir Petrovsky for his invaluable support both for experimental and theoretical aspects of my study. His wisdom and continuous guidance has a major impact on my education as well as my scientific work.

Gratitude is extended as well to my fellow graduate students Aligul Buyukaksoy, Sheng Chao and Isaiah Kellogg. Working and learning together with you was a great pleasure.

Final thanks go to my friends and family. Their support and encouragement from all over the world have always been a motivation for me to keep moving forward.

TABLE OF CONTENTS

Page

PUBLICATION DISSERTATION OPTION iii
ABSTRACT v
ACKNOWLEDGEMENTS vi
LIST OF ILLUSTRATIONS x
LIST OF TABLES xiv
SECTION
1. INTRODUCTION 1
1.1. IMPORTANCE OF SOLID OXIDE FUEL CELLS 1
1.2. WORKING PRINCIPLE OF SOLID OXIDE FUEL CELLS 2
2. BACKGROUND 8
2.1. STRUCTURE OF AN SOFC 8
2.2. ELECTROLYTE 11
2.3. CATHODE 13
2.4. ANODE 15
2.5. CURRENT COLLECTORS 16
2.6. SUMMARY OF THE STATUS OF SOFCS 18
3. PURPOSE OF THIS DISSERTATION 20
PAPER
I. INFLUENCE OF MICROSTRUCTURAL EVOLUTION ON THE ELECTROCHEMICAL PERFORMANCE OF LSM-YSZ COMPOSITE CATHODES FOR HIGH PERFORMANCE SOLID OXIDE FUEL CELLS 22
Abstract 22
1. Introduction 23
2. Experimental 25
2.1. Fabrication 26
2.2. Characterization 28
3. Results and discussion 29
4. Summary and conclusions 37

Acknowledgements 38

References 39

II. SILVER COMPOSITES AS HIGHLY STABLE CATHODE CURRENT COLLECTORS FOR SOLID OXIDE FUEL CELLS 48

ABSTRACT 48

I. INTRODUCTION 49

II. EXPERIMENTAL 50

III. RESULTS AND DISCUSSION 52

IV. CONCLUSIONS 59

ACKNOWLEDGEMENTS 59

REFERENCES 59

III. SILVER BASED PEROVSKITE NANOCOMPOSITES AS COMBINED CATHODE AND CURRENT COLLECTOR LAYERS FOR SOLID OXIDE FUEL CELLS 68

Abstract 68

Introduction 69

Experimental 72

Results and discussion 74

Summary and conclusions 79

Acknowledgements 80

References 80

IV. EFFECT OF VARIOUS PORE FORMERS ON THE MICROSTRUCTURAL DEVELOPMENT OF TAPE-CAST POROUS CERAMICS 89

Abstract 89

1. Introduction 90

2. Experimental procedure 94

3. Results and discussion 97

3.1. Particle characteristics of the pore formers 97

3.2. Effect of pore formers on the rheological properties of the ceramic slurries 99

3.3. Thermal analysis of the pore formers 100

3.4. Sintering characteristics and the analysis of the microstructures 101
4. Summary and conclusions 106
Acknowledgements 108
References 108
V. DEVELOPMENT OF THE ANODE PORE STRUCTURE AND ITS EFFECTS ON THE PERFORMANCE OF SOLID OXIDE FUEL CELLS. 121
Abstract 121
1. Introduction 122
2. Experimental 127
2.1. Fabrication 128
2.2. Characterization 131
3. Results and discussion 132
4. Summary and conclusions 142
Acknowledgements 144
References 144
SECTION
4. CONCLUSIONS 156
5. FUTURE WORK 163
APPENDICES
A. DEVELOPMENT OF A SILVER BASED STABLE CURRENT COLLECTOR FOR SOLID OXIDE FUEL CELLS 165
B. EFFECT OF THE ANODE MICROSTRUCTURE ON THE ENHANCED PERFORMANCE OF SOLID OXIDE FUEL CELLS 177
C. ANALYSIS OF THE HIGH TEMPERATURE STABILITY OF SILVER BASED POROUS COMPOSITES 204
REFERENCES 220
VITA 224

LIST OF ILLUSTRATIONS

Figure Page

1.1. Comparison of the specific power of the SOFCs with other power generation systems as a function of the power density. [3] 1

1.2. Comparison of the theoretical efficiencies of a combustion engine and a fuel cell as a function of the operating temperature. [10] 4

1.3. Schematic illustration of an SOFC and the governing reactions. [11] 6

1.4. Comparison of the current density – voltage profiles of ideal theoretical fuel cell and operating fuel cell. 7

2.1. Scanning electron micrograph of a typical cross-sectional fracture surface of a planar SOFC 8

2.2. Schematic illustration of the phases forming the electrodes and their percolation along with the formation of reaction sites (TPBs). [15] 9

2.3. Flow chart for the fabrication of SOFCs 10

2.4. Ionic conductivities of various electrolyte materials. [16] 12

2.5. Application of an interconnect for current collection on LSM-YSZ cathode layer (a) and in-plane current flow around the contact (b). 18

PAPER I

1. Scanning electron micrographs of (a-c) 45 vol% LSM – 55 vol% YSZ, (d-f) 50 vol% LSM – 50 vol% YSZ and (g-i) 55 vol% LSM – 45 vol% YSZ cathodes sintered at (a, d, g) 1100^{o}C, (b, e, h) 1150^{o}C and (c, f, i) 1200^{o}C for two hours 41

2. X-ray diffraction spectra of (a) 45 vol% LSM – 55 vol% YSZ, (b) 50 vol% LSM – 50 vol% YSZ and (c) 55 vol% LSM – 45 vol% YSZ cathodes sintered at 1250^{o}C for two hours. 42

3. (a, c) Cole-Cole plots and (b, d) Bode plots calculated from the measured impedance spectra of the symmetrical 50 vol% LSM – 50 vol% YSZ cathode cells sintered at various temperatures. Note that all of the measurements were performed at 800^{o}C in air and the equivalent circuit model used for the characterization of the impedance spectra is demonstrated in (c) 43

4. Magnitudes of the area specific polarization resistances of the characterized high and low frequency arcs from the Cole-Cole plots. Note that they are given as area specific resistances for the symmetrical cells of (a) 45 vol% LSM – 55 vol% YSZ and (b) 55 vol% LSM – 45 vol% YSZ cathodes while (d) total cathode polarization resistances are given per electrode. 44

5. Temperature dependence of the deconvoluted high and low frequency arcs of the symmetrical 50 vol% LSM – 50 vol% YSZ cathode cell sintered at 1150^{o}C. 45

6. Scanning electron micrograph of the cross-sectional fracture surface of the developed anode supported planar SOFC after measurements..... 46

7. Voltage and power density of the fabricated SOFC as functions of current density at various temperatures..... 46

8. (a) Cole-Cole and (b) Bode plots calculated from the measured impedance spectra of the symmetrical 50 vol% LSM – 50 vol% YSZ cathode cell sintered at 1150^{o}C and the fabricated SOFC at 800^{o}C. Deconvolution of the arc associated with the cathode polarization is shown for the comparison purposes. 47

PAPER II

1. SEM micrographs of (a, b) Ag-25 vol% LSM obtained after 2 hours and 170 hours of measurements at 800^{o}C, respectively. 63

2. Electrical conductivity of Ag composites with various LSM loadings at 800^{o}C in air. 64

3. SEM micrographs of (a, b) Ag-25 vol% LSM obtained after 2 hours and 170 hours of measurements at 800^{o}C, respectively.. 64

4. Area specific resistances of the YSZ electrolyte, symmetrical pure Ag cell and symmetrical Ag-25 vol% LSM cell at 800oC as a function of time..... 65

5. Cole-Cole plot of the experimental data of pure Ag measured at 800^{o}C and its fitting according to the equivalent circuit model.. 65

6. Temperature dependence of the characteristic relaxation frequency of Warburg impedance.. 66

7. (a) Characteristic relaxation frequency and (b) diffusion length as functions of time, calculated from the impedance spectra of the pure Ag and Ag-25 vol% LSM cells measured at 800^{o}C..... 67

8. Change of the effective contact area represented by the calculated coverage coefficient, α, with increasing time at 800^{o}C..... 68

PAPER III

1. Scanning electron micrographs of porous Ag-20 vol% YSZ composite (a) after 2 hours of measurements and (b) after 170 hours of measurements at 800°C in air. 83

2. Illustration of the infiltration of polymeric precursors into porous Ag electrodes and their conversion to perovskite particles. 84

3. Scanning electron micrographs of (a, b, c) LSM, (d, e, f) LSF and (g, h, i) LSCF infiltrated porous Ag-20vol% YSZ composite electrodes after 200 hours of measurements at 800°C in air. 85

4. Cole-Cole plots calculated from the measured impedance spectra of the composite electrodes and the equivalent circuit model used for their characterization. 86

5. (a) Area specific ohmic resistances (ASR1) of the symmetrical cells and (b) polarization resistances (ASR2) of the Ag based nanocomposite cathodes as a function of time. 87

6. Temperature dependences of the cathode polarization resistances (ASR2) of the nanocomposite electrodes. 88

7. Illustration of the cross-section of Ag based perovskite nanocomposite electrodes on YSZ electrolytes and the possible pathway for the transport of oxygen atoms. 88

PAPER IV

1. Scanning electron micrographs of (a) flake graphite, (b) spheroidal graphite, (c) PMMA, (d) sucrose and (e) polystyrene particles, respectively. 114

2. Number weighted particle size distributions of (a) flake graphite, (b) spheroidal graphite, (c) PMMA, (d) sucrose and (e) polystyrene particles, respectively. 115

3. Viscosities of the tape casting slurries with various pore formers as a function of applied shear rate. 116

4. Thermogravimetric analysis of (a) the hydrocarbon based pore formers and (b) the graphite based pore formers with respect to the plasticized binder (PVB). 116

5. Scanning electron micrographs of the cross sections of the sintered porous YSZ samples prepared by removal of (a) flake graphite, (b) spheroidal graphite, (c) PMMA, (d) sucrose and (e) polystyrene pore formers, respectively. 117

6. Pore size distribution of the sintered tapes characterized by the mercury intrusion porosimetry. 117

PAPER V

1. Scanning electron micrographs of flake graphite (a), spheroidal graphite (b), PMMA (c), sucrose (d) and polystyrene (e) pore former particles. 148

2. Scanning electron micrographs of the cross sectional fracture surface of the sintered and reduced Ni-YSZ anodes processed by removal of flake graphite (a), spheroidal graphite (b), PMMA (c), sucrose (d) and polystyrene (e) pore former particles. 149

3. Cumulative intruded volume of Hg as a function of pore size in sintered and reduced Ni-YSZ anodes processed by removal of various pore formers. 149

4. Top and side views of the co-sintered anode supported thin electrolyte cells with reduced warpage by decreasing the electrolyte sintering shrinkage (a to c) and the fabricated planar fuel cell with no macro defects (d). 150

5. Scanning electron micrograph of a typical cross-sectional fracture surface of a developed anode supported planar SOFC. Note that the shown porous anode layer was processed by removal of spheroidal graphite particles. 150

6. Measured current density - voltage curves and the associated power densities of the fuel cells with the anodes processed by removal of various pore formers. All measurements were performed at 800^{o}C. 151

7. Cole-Cole (a) and Bode (b) plots calculated from the impedance spectra of the fuel cells with the anodes processed by removal of various pore formers. All measurements were performed at 0.5 V and 800^{o}C 151

8. Cole-Cole (a) and Bode (b) plots calculated from the impedance spectra of the fuel cells with different anode thicknesses. All measurements were performed at 0.5 V and 800^{o}C [37] 152

9. Measured current density - voltage curves and the associated power densities of the fuel cells with thin and thick anodes processed by removal of polystyrene particles. All measurements were performed at 800^{o}C [37]. 152

LIST OF TABLES

Table Page

PAPER IV

1. Particle size and surface area characteristics of the pore formers. 118

2. Compositions of the green tapes in weight and volume percents for various pore formers. 118

3. Decomposition/oxidation parameters of the pore formers and the plasticized binder (PVB). 119

4. Dimensional changes and weight losses of the laminated dry tapes after removal of pyrolyzable components and firing at 800^{o}C for one hour..... 119

5. Dimensional changes and weight losses of the laminated dry tapes after sintering..... 120

6. Measured bulk, open and closed porosities of the sintered tapes. 120

PAPER V

1. Compositions of the green NiO-YSZ anode tapes in weigth and volume percents for various pore formers. 153

2. Measured bulk, open and closed porosities of the sintered and reduced Ni-YSZ anodes processed by removal of various pore formers. 153

3. Electrical conductivity of the sintered and reduced Ni-YSZ anodes prepared by removal of various pore formers. 154

4. Dimensional changes and weight losses of the laminated dry NiO-YSZ anode tapes after removal of pyrolyzable components and sintering. 154

5. Deconvoluted components of the measured impedance spectra of the fuel cells with the anodes processed by removal of various pore formers..... 155

1. INTRODUCTION

1.1. IMPORTANCE OF SOLID OXIDE FUEL CELLS

Solid oxide fuel cells (SOFCs) are considered as the most efficient devices for conversion of chemical energy into electricity [refs]. As the oxidation of fuels take place without sluggish combustion processes, they allow obtaining electricity directly with relatively low pollutant (e.g. nitrogen and sulfur oxides, CO_2, etc.) emissions. The common fuel used in SOFCs is hydrogen and its oxidation yields water with zero pollutant emission. Conventional power generation systems are usually based on combustion of hydrocarbon based fuels with significantly low conversion efficiencies and substantially high pollutant emissions. High temperature operation gives rise to the kinetics of electrochemical processes and realizes electrical efficiencies over 60% (over %80 when combined with heat) and superior power densities with substantial specific power as shown in Figure 1.1. [1-3]

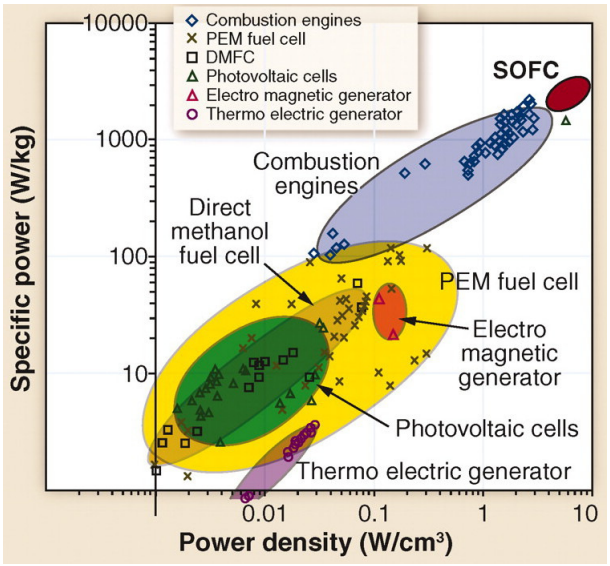

Figure 1.1. Comparison of the specific power of the SOFCs with other power generation systems as a function of the power density. [3]

Although there are several other fuel cell concepts (e.g. polymeric exchange membrane – PEM and direct methanol fuel cell – DMFC), only the structure of the SOFCs and their operation at elevated temperatures (i.e. 550^{o}C-1000^{o}C) permit utilization of fuels with different compositions (e.g. hydrocarbons) and contaminant levels due to their ability to reform the fuel internally and convert to electricity with reduced emissions satisfying the environmental concerns [4, 5]. The basic design of fuel cells contributes greatly to their sustainability. They have almost no moving parts, and in some cases are completely made of solids. The conventional power generation systems have scalability issues where the small scale applications result in a drop in their efficiency such as small scale combustion engines with efficiencies below 15%. Considering the scalability of the SOFCs without losing their power densities they are considered as a promising solution to substitute current power generation systems from small scale (e.g. laptop batteries and automotive engines) to large scale (e.g. power stations and plants). The flexible fuelling options also make them suitable power sources for off-grid distributed power generation systems such as micro grid and remote applications (e.g. phone towers). [6-8]

1.2. WORKING PRINCIPLE OF SOLID OXIDE FUEL CELLS

Efficiency of a power generation system is identified as the ratio of the useful energy to the total energy of the fuel. Conventional power generation systems transform the chemical energy of the fuel to thermal energy first by combustion and to mechanical energy followed by the conversion to the electrical energy. The theoretical efficiency of an internal combustion engine is governed by the Carnot limitation which is given as:

$$\eta_{Combustion} = 1 - \frac{T_{Low}}{T_{High}} \tag{1}$$

where the combustion engine works at T_{high} and the rejection (sink) temperature is T_{low}. On the other hand, fuel cells do not obey the Carnot limitation as they are electrochemical devices while Carnot engine is a thermal machine operating according to a temperature difference. The theoretical efficiency of a fuel cell is the ratio of the electrical work to the total chemical energy of the fuel it can be converted from.

A change in the Gibbs free energy can be defined as:

$$dG = dU - TdS - SdT + PdV + VdP \tag{2}$$

If the work term in dU is expanded to include mechanical and electrical work:

$$dU = TdS - dW \tag{3}$$

$$dU = TdS - (PdV + dW_{Electrical}) \tag{4}$$

At a constant pressure and temperature:

$$dG = -dW_{Electrical} \tag{5}$$

and thus:

$$W_{Electrical} = -\Delta G \tag{6}$$

Therefore, it can be concluded that the theoretical efficiency of a fuel cell is the ratio of the Gibbs' free energy and the enthalpy of formation of the fuel as it gives the maximum useful energy given as:

$$\eta_{Theoretical} = \frac{\Delta G}{\Delta H} \tag{7}$$

A fuel cell yields a theoretical efficiency of 70% when operated at 600^{o}C forming liquid water using pure hydrogen as fuel and pure oxygen as oxidizer. A combustion

engine working at the same temperature yields a theoretical efficiency of 63% when the rejection is at 50°C as shown in Figure 1.2. Although the theoretical efficiency of the combustion engines exceeds the efficiency of the fuel cells at temperatures above 800°C, in practice, they cannot achieve average efficiencies over 20% due to mechanical and heat losses. [3, 9]

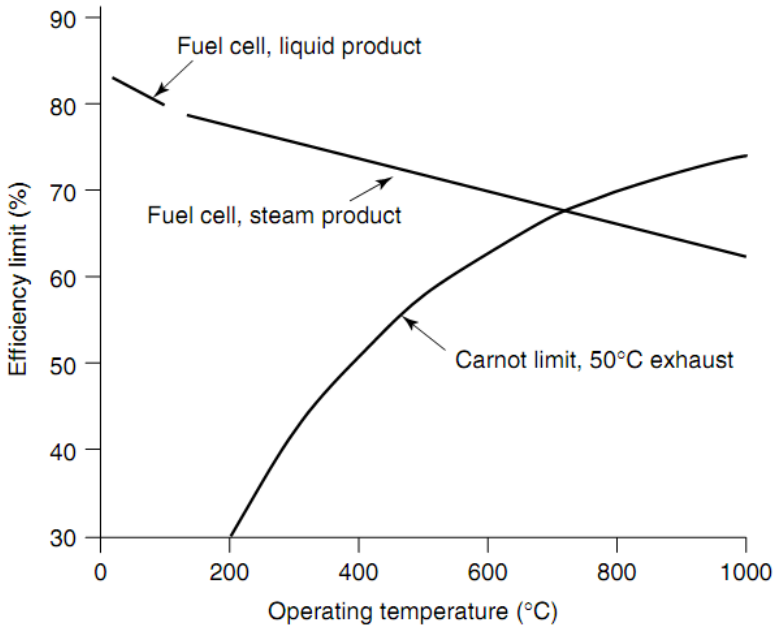

Figure 1.2. Comparison of the theoretical efficiencies of a combustion engine and a fuel cell as a function of the operating temperature. [10]

The potential of a fuel cell to conduct electrical work is defined by electrical voltage. Electrical work can be described as the movement of a charge Q through an electrical potential E.

$$W_{Electrical} = EQ \tag{8}$$

If the charge is carried by electrons:

$$Q = nF \tag{9}$$

and the Equation (5) becomes Equation (10).

$$\Delta G = -nFE \tag{10}$$

For the reaction, $H_2 + \frac{1}{2}O_2 \rightleftarrows H_2O$, ΔG° is -237 kJ/mol under standard conditions. Thus, the potential of a hydrogen–oxygen fuel cell (open circuit voltage, OCV) can be calculated as:

$$E^o = \frac{-\Delta G^o}{nF} = -\frac{-237 kj/mol}{(2 mole^- / mol react.)(96,400 C/mol)} = 1.23V \tag{11}$$

In the SOFC configuration, the fuel side (anode) is separated from the oxidizer side (cathode) with a gas-tight electrolyte which allows transfer of oxygen ions selectively as shown in Figure 1.3. Hence, an oxygen concentration gradient is developed when different oxygen partial pressures (chemical activity of oxygen) are introduced on each electrode interface. The gradient also induces formation of the electrochemical potential mentioned earlier. The direction of the oxygen ion flow is determined by concentration gradient developed on the electrolyte layer. A flow of electrons is induced from anode to the cathode side when a load is applied and electrons are drawn. Oxygen ions are required to be transferred in the opposite direction to maintain the electrochemical potential. Hence, it results in reduction of oxygen on the cathode side with higher oxygen partial pressure and their transport through electrolyte prior to oxidation of the hydrogen on the anode side with lower oxygen partial pressure.

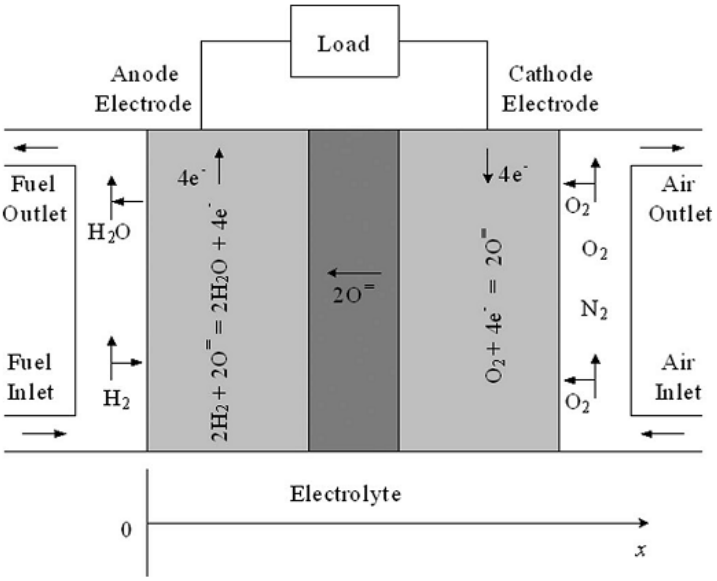

Figure 1.3. Schematic illustration of an SOFC and the governing reactions. [11]

The thermodynamic concept of the SOFC suggests its operation at a stable potential like batteries as long as the current and oxygen flows maintain the electrochemical potential. However, there are various polarization (overpotential) mechanisms limiting the kinetic flow of the charged species and causing deviation from the theoretical voltage as the electrochemical potential cannot be maintained as shown in Figure 1.4.

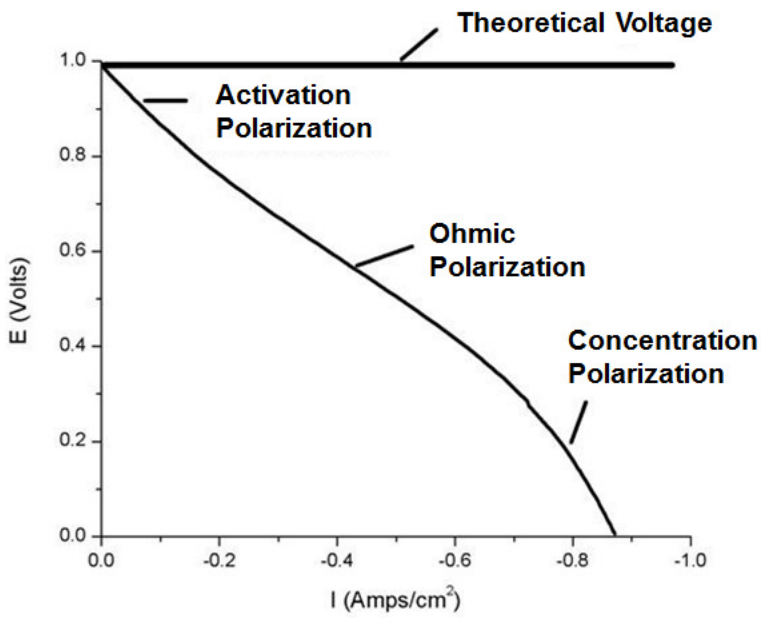

Figure 1.4. Comparison of the current density – voltage profiles of ideal theoretical fuel cell and operating fuel cell.

The electrochemical polarization mechanisms can be classified as (i) activation polarization, (ii) ohmic polarization and (iii) concentration polarization. The retarded kinetics of electrode reactions (e.g. reduction of oxygen on the cathode and oxidation of hydrogen on the anode) give rise to the activation polarization while the concentration polarization is induced by the limited transport of the reactant and/or product gases through the electrodes. The ohmic polarization arises due to the electrical resistance of the components (e.g. electrodes, electrolyte and current collectors) [12-14].

2. BACKGROUND

2.1. STRUCTURE OF AN SOFC

The fundamental electrochemical configuration of SOFCs consists of a dense electrolyte with porous electrodes on each side. The conventional SOFC utilizes a yttria stabilized zirconia electrolyte (YSZ), Ni – YSZ anode and a lanthanum-strontium manganite (LSM) – YSZ cathode as shown in Figure 2.1.

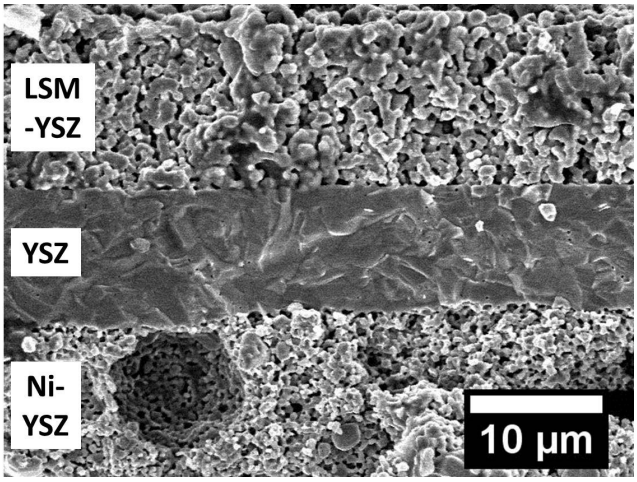

Figure 2.1. Scanning electron micrograph of a typical cross-sectional fracture surface of a planar SOFC.

The electrolyte layer is required to be dense to prevent the interpenetration of the fuel and oxidizer gases on each side while selectively conducting oxygen ions from the cathode side to the anode side. Therefore, substantial ionic conductivity is desired to give rise to the electrochemical processes of the electrodes. As electronic contact between the electrodes would result in a decrease in the operating voltage and ultimately short, the electrolyte layer has to possess negligible electronic conductivity.

Catalyzed reactions, reduction of oxygen on the cathode (LSM) and the oxidation of hydrogen on the anode (Ni), take place when the transport of all required reactants and

products is maintained. Thus, the electronic conductor – electrocatalyst (Ni or LSM), ionic conductor (YSZ) and pores are required to converge to form reaction sites on the electrodes. This reaction sites are also called triple phase boundaries (TPBs). However, formation of the reaction sites does not guarantee the electrochemical activity as the transport of the species is required through the complete electrode as shown in Figure 2.2. Hence, the continuous percolation of all three phases (i.e. electronic conductor, ionic conductor and pores) is required to actively utilize the formed reaction sites.

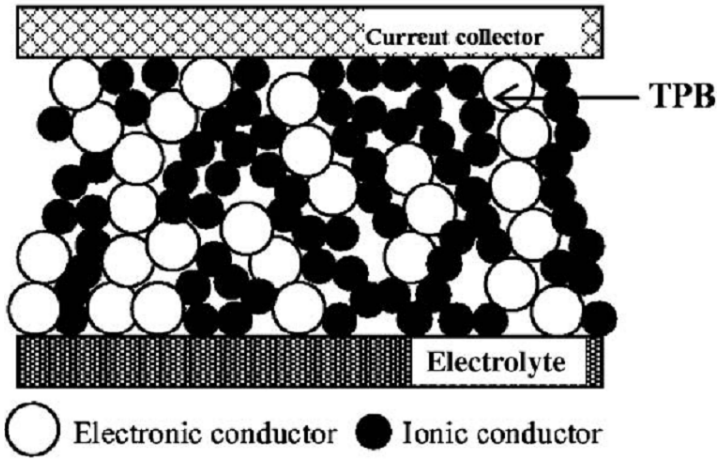

Figure 2.2. Schematic illustration of the phases forming the electrodes and their percolation along with the formation of reaction sites (TPBs). [15]

As the reactions take place, the oxygen ions are conducted from the cathode reaction sites to the anode reaction sites through the electrolyte and the charge balance is compensated by the flow of the electrons from the anode to the cathode reaction sites through the electronically conducting phases and the current collectors when an electrical load is applied.

The Kroger-Vink notation will be used throughout the dissertation to discuss the conduction mechanisms in the components. The notation involves lattice position of the defects and the species compensating the charge neutrality.

$(A_{S^C}^{C})^{B}$

A: corresponds to the species (atoms, electrons and electron holes) and vacancies

S: corresponds to the lattice position

C: corresponds to the charge of the species or the lattice position

B: indicates the net charge of the defect

The conventional route for the fabrication of SOFCs is based on processing of the desired powder compositions. The slurries of the anode and electrolyte layers are cast into tapes and laminated together prior to their co-sintering at elevated temperatures. The fabrication of the fuel cells completed by screen-printing of the cathode layers on the dense electrolyte layer and their sintering as illustrated in Figure 2.3.

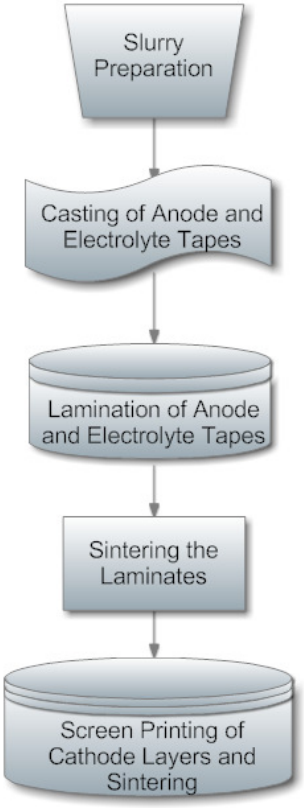

Figure 2.3. Flow chart for the fabrication of SOFCs.

Each component contributing to the order of the electrochemical reactions will be introduced in the following sections. The current problems and the required studies will also be discussed in the content of the scope of this dissertation.

2.2. ELECTROLYTE

The electrolyte provides the transfer of the oxygen ions from the cathode reaction sites to the anode reaction sites to maintain the reduction and oxidation reactions, respectively. Therefore, it is required to satisfy the fundamental requirements below:

(i) Substantial ionic conductivity

(ii) Relatively low electronic conductivity

(iii) No gas permeability

(iv) Chemical and microstructural stability in both reducing and oxidizing atmosphere at elevated operating temperatures (e.g. 800^{o}C)

In case the ionic conductivity is not sufficient, it would give rise to the ohmic polarization resistance and result in significant losses in the electrochemical performance of the fuel cells. The permeation of the gases through the electrolyte cause a drop in the gradient formed on the electrolyte due to the decrease in the oxygen partial pressure (activity of oxygen) difference between the electrode interfaces. As a result, the voltage decreases and it deteriorates the electrochemical performance of the SOFC. Electronic conductivity of the electrolyte causes a similar problem by allowing the compensation of the oxygen activity on each side of the electrolyte by violating the working principle of SOFCs which requires conductivity of the oxygen ions.

There are various candidate materials for electrolyte applications as shown in Figure 2.4. Although it does not possess the highest ionic conductivity, stabilized cubic zirconia is the most commonly employed material for electrolyte applications as it satisfies the fundamental requirements while the other highly conductive materials such as bismuth oxide fail due to substantial electronic conductivity.

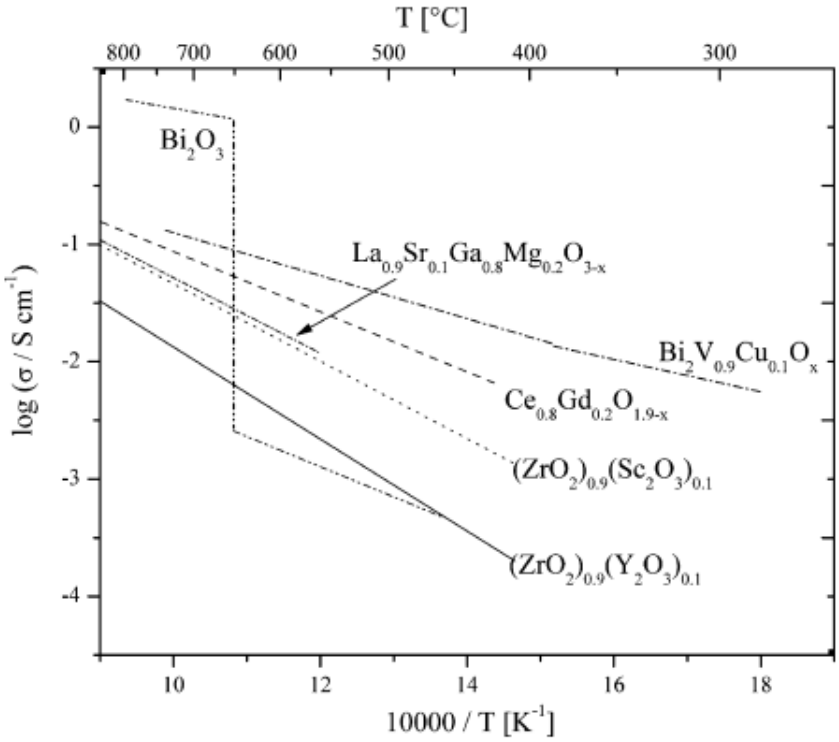

Figure 2.4. Ionic conductivities of various electrolyte materials. [16]

The properties such as thermal conductivity, stability in highly reducing and oxidizing atmospheres, thermal expansion similar to other SOFC component materials and sinterability makes 8 mol% yttria stabilized zirconia (YSZ) the most common solid-state oxygen conducting electrolyte. It is widely used as oxygen sensor in automobile combustion feedback systems and industrial process monitoring [17-20]. As the yttria (Y_2O_3) is dissolved in zirconia (ZrO_2) to stabilize its cubic phase, it does not provide

enough anions (O^{2-}) with respect to the cations (Y^{3+}) it provides while substituting Zr^{4+}. Hence, an oxygen vacancy is formed for each pair of Y^{3+} substituting Zr^{4+} in order to maintain the charge neutrality as given below. The relatively large amount of oxygen vacancies (over 10%) allows substantial ionic conductivity.

$$Y_2O_3 + 2(Zr_{Zr^{4+}}^{4+})^x + (O_{O^{2-}}^{2-})^x = 2(Y_{Zr^{4+}}^{3+})' + (V_{O^{2-}})'' + 2O_2 \quad (12)$$

There have been many attempts to decrease the contribution of the YSZ electrolyte to the total ohmic polarization resistance of the SOFCs. The use of thin electrolytes has been a favorable solution as the area specific ohmic resistance (ASR) of the electrolyte decreases proportional to its thickness. It allowed the high performance of current SOFCs. Although YSZ electrolyte is the most developed component of the SOFC configurations, application of a thin layer of YSZ results in fabrication challenges such as macro defects due to the difference in sintering shrinkages and initial green defects. Moreover, the amount of tolerable macro defects decrease drastically since maintaining the gas-tightness of defected electrolytes is more difficult at lower thicknesses.

2.3. CATHODE

Previously mentioned continuous percolation of the constituent phases and their convergence is required for efficient cathode performance. Thus, the material employed for cathode application has to possess ionic and electronic conductivity, as well as an open pore structure for delivery of oxidizer gas and catalytic activity for the reduction of oxygen.

The typical cathode material utilized in SOFCs is doped lanthanum manganite. Doping with aliovalent cations, commonly with Sr, yields its substantial electronic conductivity (~65 S/cm) [21]. While dissolved Sr^{2+} substitutes La^{3+}, Mn^{3+} donates an electron and changes its valence to 4+ to maintain the charge neutrality after the doping as given below. The localized Mn sites induce the conduction of electrons by polaron hoping.

$$SrO + (Mn_{Mn^{3+}}^{3+})^{x} = 2(Sr_{3+}^{2+})' + 2(Mn_{Mn^{3+}}^{4+})^{\bullet} + \frac{1}{2}O_2 \tag{13}$$

Although high electronic conductivity and substantial catalytic activity makes lanthanum-strontium manganite (LSM) a good candidate, its ionic conductivity is negligible. Therefore, use of LSM as a single material cannot form an efficient cathode for SOFCs.

Incorporation of ionically conductive YSZ particles into LSM cathodes has been a common practice to provide the required ionic conductivity to the reaction sites [22-24]. Even though increase in the cathode performance was observed, the interactions of the solid phases, LSM and YSZ, at elevated temperature during processing result in formation of undesirable phases and microstructures. The distinct temperatures required for the sintering of the constituent phases makes the control of the microstructural development relatively difficult, while they form insulating and catalytically inactive phases during sintering. Since the evolution of the porous composite microstructures and their relations with the resultant polarization mechanisms are not determined clearly, there is a controversy about the performance of LSM-YSZ composite cathodes [25, 26].

2.4. ANODE

The anode layer is required to provide electronic and ionic conductivity, as well as catalytic activity for oxidation of hydrogen. Permeability of gases has a significant importance in the anode layer since it does not provide only the delivery of the fuel but also provides the removal of the product gases such as water vapor.

The common anode material employed in SOFCs is Ni as it possesses the required substantial electronic conductivity and catalytic activity for oxidation of hydrogen. However, it does not provide conductivity for oxygen ions. Hence, YSZ phase is incorporated to the Ni electrodes to maintain the flow of oxygen ions to the active reaction sites.

Fabrication of porous Ni-YSZ composite anode layers is easier than the LSM-YSZ layer since their high temperature sintering does not result in formation of undesirable phases. Thus, thin electrolyte layers (<100 μm) prepared for reduction of the ohmic losses can be supported by a thicker anode layer and fabricated by co-sintering. It is not possible to support the YSZ layer with LSM-YSZ composite cathode layer and fabricate by co-sintering due to undesired high temperature interactions. Moreover, relatively high electrical conductivities (>1000 S/cm) can be achieved with porous Ni-YSZ anodes [27, 28] whereas the electrical conductivity of the porous LSM-YSZ cathodes is limited (<10 S/cm) [29, 30].

As desired percolation of three phases (i.e. Ni, YSZ and pores) form in the porous Ni-YSZ anode layers, the processing parameters identify the development of the overall microstructure. Especially the pore structure gains a significant importance when relatively thick (>500 μm) anode layers are utilized to support the electrolyte layers since

it forms a longer pathway for the delivery of the fuel gas and the removal of the product gases.

Application of thick (>500 µm) porous anode layers to support desired thin dense electrolyte layers (<20 µm) also results in fundamental material challenges during co-sintering process. Each layer induces a different shrinkage during sintering and it causes developing tensile and compressive stresses throughout the SOFC. Although the supporting anode layer can compensate tensile stresses, they would result in catastrophic failure on the thin electrolyte layers due to formation of cracks under tensile stress. Thus, there are major material issues related with the identification of the desired microstructural features for efficient anodes and the processing parameters for fabrication of the multilayer SOFCs without macro defects (e.g. cracks, warpage and delamination) [31, 32].

2.5. CURRENT COLLECTORS

The ohmic losses formed in the SOFC configuration are not limited to the contributions from the main components (cathode, anode and electrolyte). As mentioned earlier, the operation of SOFC is maintained by transfer of two species, oxygen ions and electrons. While the oxygen ions are transferred through the electrolyte, electrons are transferred from the anode to the cathode by electrical contacts (see Figure 1.3.). Efficient transport of electrons is provided by current collectors in SOFC configurations. The current collectors are applied on the electrodes and form a reliable contact to minimize ohmic polarization resistances. As the supporting Ni-YSZ anode layers are relatively conductive (>1000 S/cm), current collection can be maintained by forming

connections through a metal meshes or wire contacting the outer anode surface. However, the limited electrical conductivity (<10 S/cm) of the porous LSM-YSZ cathode layer restricts the use of metal meshes as current collector since in-plane current collection in poor electrical conductors results in significant ohmic losses [31, 33-35]. Thus, the ideal in-plane current collection is provided by applied current collector contact layers on LSM-YSZ cathodes. The fundamental requirements for efficient current collector layers are listed below.

(i) High electronic conductivity

(ii) Substantial gas permeability through its pores

(iii) Bonding to the underlying electrodes for electrical contact

(iv) Compatibility with other SOFC components

(v) Chemical and mechanical stability in oxidizing atmospheres at operating temperatures (e.g. 800^{o}C)

Although some oxides (e.g. $LaCrO_3$ and $LaCoO_3$) are considered for current collector applications due to their high temperature stability in oxidizing atmosphere, their restrained electrical conductivity limited their use. Since some precious metals such as Pt, Pd and Au satisfy the requirements for current collectors, they are used in laboratory level SOFC operations [36-39]. Pastes of their powders are applied on both electrodes and partially sintered to form the electrical contacts while preserving their porous microstructure. However, the cost of their raw materials is significantly high and they cannot be employed for realizing the SOFC technology.

There were several attempts to address the current collection issues by transferring the current out-of-plane using highly conductive stainless steel interconnects

as shown in Figure 2.5 [40]. Although some improvements were made, the ohmic losses could not be eliminated due to the limited electrical conductivity of the LSM-YSZ composite cathodes at areas where the current is transferred in-plane. The formed contacts are also not efficient as the bonding is provided only by the applied mechanical forces. Moreover, the high temperature interactions of the stainless steel components with the SOFC cathodes resulted in loss in the catalytic activities due to Cr poisoning [41, 42].

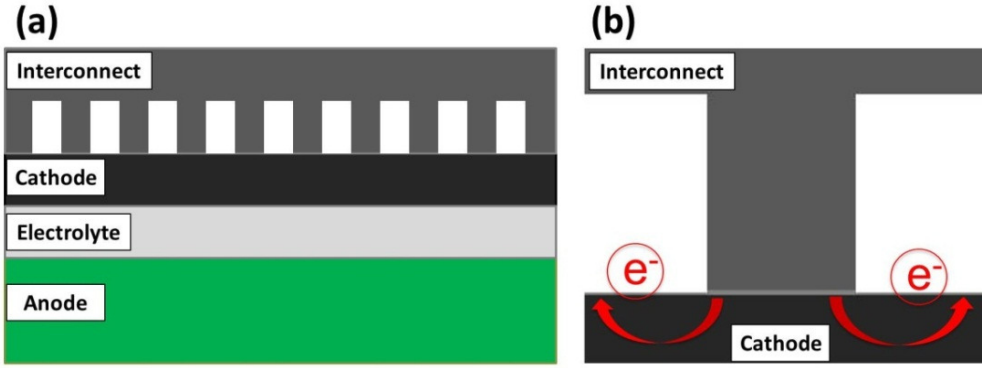

Figure 2.5. Application of an interconnect for current collection on LSM-YSZ cathode layer (a) and in-plane current flow around the contact (b).

Even though utilization of inexpensive non-oxidizing metals such as Ag was considered, stability of its desired porous structure was limited at the typical operating temperatures of the SOFCs (e.g. 800^{o}C) near its melting temperature (962^{o}C). Porous Ag reaches near its theoretical density in less than 100 hours at 650^{o}C which makes it impossible to use it as a stable component in SOFC operating conditions [43].

2.6. SUMMARY OF THE STATUS OF SOFCS

The SOFC concept is highly promising for efficient power generation. Although various materials have been investigated for development of its components, the challenging requirements of its operation exhausts the available monolithic materials as

well as composites. Except the electrolyte material of choice, YSZ, the development of the electrode materials and the current collectors is still under development and their properties are required to be investigated for realization of the SOFC technology. Therefore, the fundamental problems of the SOFC technology are out of the scope of the engineering design and mainly involve the research and scientific investigation of the component materials.

The polarization mechanisms limiting the performance of the LSM-YSZ composite cathodes and their relationships with the microstructural features should be clearly identified. Moreover, the correlations between the processing parameters and the evolution of the microstructural properties need to be determined for optimization of the reproducible LSM-YSZ cathode layers.

Since the anode supported SOFCs are more desirable due to the employed thin electrolytes with minimized ohmic losses, the effects of their microstructures on the electrochemical performance are required to be determined. Anode pore structure has a critical importance as its increased thickness limits the transport of gases between the active reaction sites and the outer surface. The correlation between the anode pore structure and the electrochemical polarization mechanisms of the SOFCs should be revealed.

Addressing the major ohmic losses on SOFCs due to electrical contacts can eliminate material and design problems as the current collection can be performed in-plane. The degradation mechanisms of the inexpensive non-oxidizing metals are required to be investigated and their microstructures should be modified to allow their use as current collector layers at elevated temperatures.

3. PURPOSE OF THIS DISSERTATION

The main purpose of this study was investigating the relationships between the processing parameters, properties of the developed microstructures and the electrochemical performance of the solid oxide fuel cell (SOFC) components. Lanthanum-strontium manganite (LSM) – yttria-stabilized zirconia (YSZ) composites were investigated for oxygen reduction activities on the cathode side of the solid oxide fuel cells (SOFCs). Electrochemical impedance spectroscopy techniques along with the microstructural characterization techniques were utilized to gain fundamental understanding on the origin of the polarization mechanisms limiting the cathode performance.

Ag based composites were studied to reveal the phenomena deteriorating their electrical and electrochemical properties and microstructural stability at elevated temperatures. A model was developed based on the impedance response of the Ag based composites to determine the mechanisms yielding polarization resistances. It allowed correlating microstructural changes with the impedance spectra at in-situ at operating temperatures and identifying their relationships. Processing parameters were modified according to the determined mechanisms to improve the Ag based composites for stable electrochemical and electrical properties. The performance of the developed Ag based composites was evaluated as current collector and combined cathode layers for SOFCs. Effect of the pore structure on the kinetics of the oxidation of hydrogen was analyzed on the Ni-YSZ composite anodes. Distinct pore structures were formed by utilizing evaluated pyrolyzable pore former particles. The evolution of the anode pore structures was investigated using microscopy techniques and mercury intrusion porosimetry.

Combining the developed components with an electrolyte using the determined processing parameters allowed evaluating the layers further on operating fuel cell conditions. The deconvolution of the impedance spectra and the analysis of the voltammetric measurements were studied to develop a complimentary understanding correlating the anode pore structure with the electrochemical polarization mechanisms. The revealed correlations between the microstructural features and the electrochemical performance of the component layers were combined to optimize the processing parameters and the performance of the SOFCs. Fabrication of complete SOFCs and their electrochemical evaluations extended the fundamental study on the component materials to their further analyses in operating conditions.

PAPER

I. INFLUENCE OF MICROSTRUCTURAL EVOLUTION ON THE ELECTROCHEMICAL PERFORMANCE OF LSM-YSZ COMPOSITE CATHODES FOR HIGH PERFORMANCE SOLID OXIDE FUEL CELLS

Ayhan Sarikaya, Vladimir Petrovsky and Fatih Dogan

Department of Materials Science and Engineering,

Missouri University of Science and Technology, Rolla, MO 65409, U.S.A.

Abstract

Microstructure of the lanthanum-strontium manganite (LSM)-yttria stabilized zirconia (YSZ) based composite cathodes plays a critical role in the performance of solid oxide fuel cells (SOFCs). Impedance spectroscopy measurements were performed on symmetrical cathode cells (cathode/electrolyte/cathode) while varying the processing parameters such as component ratios and sintering temperatures. Detailed investigations on the resulted microstructures and the impedance spectra revealed the relationships between the developed microstructural features and the induced polarization resistances. Two processes with distinct characteristic relaxation frequencies and activation energies were identified. As the high frequency process with the activation energy of ~1.35 eV was correlated with the charge transfer processes between the constituent phases, the low frequency process with the activation energy of ~1.9 eV was related with the surface processes. Characterized relationships between the developed microstructures and the components of the yielded impedance spectra allowed determining the optimum processing conditions and achieving polarization resistances as low as 0.040 Ohm cm^2 at

800°C in air. The developed cathode layer induced a similar polarization resistance when tested in anode supported SOFCs. The obtained power density (1.76 W/cm^2 at 800°C) confirmed the applied approach for identification of the performance limiting parameters and optimization of the microstructural development of the LSM-YSZ cathodes.

I. Introduction

Solid oxide fuel cells (SOFCs) are highly attractive energy conversion devices as they combine desirable features such as relatively high conversion efficiencies and flexible fuel options with significantly low pollutant emissions. Various configurations were employed to improve the performance of the SOFCs. As it allowed achieving some of the highest performances up-to-date and can be fabricated facilely using conventional processing techniques, anode supported design with a thin electrolyte and cathode is one of the most promising configurations for the realization of the SOFC technology.[1-3]

Performance of the SOFCs is significantly affected by the microstructure of their components. Use of thin electrolytes in anode supported SOFCs minimizes the ohmic losses at the operating temperatures (e.g. 800°C); however, performance losses remain significant on the electrodes. Especially sluggish kinetics of the reactions related with the reduction of oxygen at the cathodes limit the performance of the SOFCs operating at intermediate temperatures (550°C-800°C).[4-6]

A perovskite structured oxide of A-site Sr doped $LaMnO_3$ (LSM) is the most commonly used cathode material for SOFCs based on yttria-stabilized zirconia (YSZ) electrolytes due to its high electronic conductivity, chemical and thermal stability, catalytic activity for oxygen reduction and compatibility with other SOFC components.[7,8]

However, restricted ionic conductivity and relatively high activation energy of LSM limit its use in SOFCs.[9] Therefore, YSZ particles have been incorporated into LSM cathodes to increase ionic conductivity of the composite cathodes and improve their electrochemical activity by extending the triple phase boundaries (TPBs).[10-12]

Composite cathode layers are required to possess high electronic and ionic conductivity, catalytic activity as well as permeability for the transport of oxygen-rich gases (e.g. air). Continuous percolation of LSM and YSZ phases as well as pores can provide these required properties. Since the processing parameters determine formation of the LSM-YSZ composite microstructures, they substantially affect the electrochemical performance of the composite cathodes.[13-16] Size distribution and volumetric ratio of the particles as well as their dispersion identifies conditions for their percolation while the sintering process leads to integration of the constituent LSM and YSZ phases while ensuring their adhesion to the underlying YSZ electrolyte.

Broad investigations were performed on the LSM and the LSM-YSZ cathodes for the identification of the mechanisms controlling their electrochemical activity as well as the optimization of their performance.[8, 10, 17, 18] However, polarization losses due to the cathode layers remain a significant performance limiting factor in SOFCs and further investigations in this area are critical. This study was focused on identifying the relationships between the evolution of the LSM-YSZ composite microstructures and the electrochemical properties of the corresponding cathodes. Extensive use of impedance spectroscopy techniques allowed characterization of the performance limiting mechanisms inducing the polarization resistances and the relevant microstructural features. Main practical goal of these investigations was decreasing the cathode

polarization resistances to the level of the anode polarization resistances (<0.050 Ohm cm^2) in the anode supported SOFC configurations for the realization of high performance SOFCs. The identified relationships led to the optimization of the performance of the LSM-YSZ cathodes by modifying the processing parameters. The optimized cathodes were also applied on the anode supported electrolytes for their further evaluation on complete SOFCs. As optimized cathodes were combined with previously developed advanced anodes and relatively thin electrolytes, this study extended the optimization of the cathodes to the development of high performance fuel cells. Detailed analysis of the electrochemical properties of the SOFCs allowed characterization of the dominating polarization mechanisms under relatively high current densities simulating realistic operating conditions.

2. Experimental

Symmetrical cathode cells are useful for the evaluation of the cathode layers. As impedance spectroscopy and voltammetric measurements can be successfully conducted on symmetrical cells, they allow assessing the electrochemical performance of the developed cathodes. Thus, investigations of the LSM-YSZ cathodes were conducted on their symmetrical cells (cathode/electrolyte/cathode). The measurements revealed the characteristics of the development of their microstructures using various compositions and sintering temperatures. The detailed characterization of the corresponding polarization resistances by electrochemical analyses led to optimization of the cathode layers. Since properties of the cathodes may differ in operating conditions, further evaluations were required to be performed on complete (cathode/electrolyte/anode) cells.

Hence, the optimized cathode layers were applied on previously developed half-cells for analyses in operating conditions. The half-cells consisted of a porous supporting Ni-YSZ anode and a dense thin YSZ electrolyte.

2.1 Fabrication

Formation of undesired phases upon interaction of LSM and YSZ phases at elevated temperatures was widely investigated by other researchers.[7, 10, 17, 19-22] It was reported that Sr-rich LSM ($La_{1-x}Sr_xMnO_3$, x>0.3) forms $SrZrO_3$ (SZ) at temperatures above 1250^oC [10, 17] while stoichiometric LSM forms $La_2Zr_2O_7$ (LSZ) at temperatures above 1150^oC.[23] Electrical conductivities of LSZ and SZ phases are 2 x 10^{-4} S/cm and 10^{-4}–10^{-5} S/cm at 1000^oC, respectively.[24] As their conductivities are considerably lower than YSZ at 1000^oC (0.185 S/cm),[25] they form a relatively insulating interface between LSM and YSZ phases. Moreover, LSZ and SZ phases are catalytically inactive. Combination of these effects results in a significant electrochemical performance loss in LSM-YSZ composite cathodes.[9, 10] Excess La has a detrimental effect on the LSM-YSZ composites as it induces the formation of LSZ and decreases the required temperatures for its formation.[21] Lower temperatures were employed to eliminate the formation of these undesired phases. However, it was not an effective technique for the formation of the desired composite cathode microstructures as it results in poor connection between the composite phases. It was reported that A-site nonstoichiometric LSM [$(La_{1-x}Sr_x)_yMnO_3$, y<1] eliminates the formation of the LSZ phase upon interacting with YSZ at temperatures as high as 1300^oC.[14, 21, 22, 26] Therefore, A-site non-stoichiometric $(La_{0.8}Sr_{0.2})_{0.9}MnO_3$ was utilized

for this study and the sintering temperatures were limited with 1250°C to eliminate formation of any undesired phases due to its interaction with the YSZ phase.

Only commercially available materials were used for the investigations. Cathode inks were prepared for screen printing by incorporating different amounts of $(La_{0.8}Sr_{0.2})_{0.9}MnO_3$ (LSM) powder (LSM20-P and LSM20-HP, NexTech, Columbus, OH, USA) with YSZ powder (8 mol% yttria-stabilized zirconia, TZ-8Y, TOSOH, Tokyo, Japan) and dispersing it in a solvent (α-terpineol, Alfa Aesar, Ward Hill, MA, USA) by ultrasonication. An ethyl cellulose based polymeric vehicle (V-006, Heraeus, Conshohocken, PA, USA) was added to the uniformly dispersed powder mixtures and amounts of the vehicle and solvent were adjusted to obtain desirable rheological properties for screen printing. Formulated inks were screen printed on either side of 180 µm thick YSZ electrolytes (8 mol% yttria-stabilized zirconia, NexTech, Columbus, OH, USA) to form symmetrical cells. They were sintered in air at temperatures ranging from 1050°C to 1250°C. Screen printing parameters were adjusted to obtain a sintered cathode layer thickness of ~10µm for a consistent comparison.

Complete fuel cells were fabricated as described elsewhere.[27] Slurries of NiO (NexTech, Columbus, OH, USA) and YSZ powders were prepared for casting ceramic tapes. All slurries contained a dispersant (KD-1, ICI, Barcelone, Spain) and a binder (PVB-79, Monsanto, St. Louis, MO, USA) plasticized with DOP (Sigma-Aldrich, St. Louis, MO, USA). Additional pyrolyzable particles (polystyrene, Alfa Aesar, Ward Hill, MA, USA) were incorporated to the NiO-YSZ anode mixtures to obtain a desired pore structure. Tapes of NiO-YSZ and YSZ were laminated and co-sintered at 1350°C for two hours prior to screen printing and sintering of the cathode layers.

2.2 Characterization

Microstructural properties of the developed cathode layers were investigated using scanning electron microscopy (SEM) techniques. An image analysis software (ImageJ, NIST, Bethesda, MD, USA) was utilized to characterize the obtained microstructures and to reveal the effect of the compositon and sintering temperature on the cathode microstructures. Homogenous mixtures of LSM and YSZ powders were also prepared and sintered at various temperatures ranging from 1050^{o}C to 1250^{o}C. X-ray diffraction (XRD) analysis was performed on these samples for the identification of existing phases.

Electrochemical performance of the cathode layers were investigated in symmetrical cell and complete fuel cell configurations. A combined potentiostat (CellTest 1470, Solartron, Mobrey, UK) and frequency response analyzer (1255B, Solartron, Mobrey, UK) setup was employed for voltammetric and impedance spectroscopy measurements. Pt and/or LSM pastes were used on cathode layers while Pt paste was also utilized on the anode layer to attach Pt wires and maintain reliable electrical contacts. Measurements of the symmetrical cells were performed in air and the performance of the complete fuel cells were investigated at the operating conditions. Since operation of SOFCs in stacks leads to a significant decrease in the hydrogen content and an increase in the water content in the fuel flow through the consecutive cells, measurements under ideal pure hydrogen on the anode side and pure oxygen on the cathode side were not considered realistic. Therefore, air flow was maintained on the cathode side of the complete fuel cells while a diluted hydrogen mixture (10% H_2 in Ar) was used as fuel and supplied to the anode side during their operation and measurements.

3. Results and discussion

Figure 1 demonstrates the microstructures of various LSM-YSZ compositions (45:55 vol% – 55:45 vol%; LSM-YSZ) after sintering at temperatures ranging from 1100^{o}C to 1200^{o}C for two hours. Image analysis software was employed for the characterization of the grains and the pores. Average grain size of the composite cathodes exhibited an increase with the sintering temperature and the amount of the incorporated LSM. The average grain size of 45 vol% LSM- 55 vol% YSZ increased from 0.3µm (Figure 1a) to 0.6µm (Figure 1c) as the sintering temperature was increased from 1100^{o}C to 1200^{o}C. A distinguishable increase was observed in the average grain size of the LSM-YSZ composites with increased LSM content. However, the sintering temperature had a more pronounced effect on the final grain size. The average grain size of 45 vol% LSM- 55 vol% YSZ increased from 0.3µm (Figure 1a) to 0.35µm (Figure 1g) as the LSM content was increased from 45 vol% to 55 vol% for the cathodes sintered at 1100^{o}C. Therefore, a slight coarsening of the pore and grain structure took place with increasing LSM content while identical amounts of open porosity (~35 vol%) was maintained with various LSM-YSZ compositions processed at a particular sintering temperature.

The sintering temperatures of LSM-YSZ composite cathodes were limited with 1250^{o}C in this study to eliminate formation of the insulating phases. XRD analysis was performed in order to monitor possible formation of LSZ and SZ phases. Only LSM and YSZ phases were detected and undesired zirconates were not observed as shown in Figure 2. These findings were in a good agreement with the expected stable behavior of A-site non-stoichiometric LSM.

Although SEM micrographs revealed detailed information about the evolution of the composite microstructures, further analyses were required for the assessment of their electrochemical performance. Therefore, the measured impedance spectra of the symmetrical LSM-YSZ cathode cells were investigated. Cole-Cole and Bode plots were utilized for the investigations on the obtained data as shown in Figure 3. An equivalent circuit model was determined for the characterization of the impedance spectra. Nonlinear least squares fitting technique was employed for the identification of the corresponding parameters. The model consists of a resistor and two constant phase elements in series as shown in Figure 3c. The constant phase elements represent processes with distinct characteristic relaxation frequencies while the resistor in series resembles the processes with relatively high characteristic relaxation frequencies which could not be resolved using conventional impedance spectroscopy techniques. Considering the temperature range (550^{o}C-800^{o}C) where the measurements were performed, the fast processes were expected to involve the conductance of the electrolyte and the contacts (i.e. current collection resistance) which in turn induced the ohmic resistance of the cells. Resistor (R1) in the equivalent circuit model represents the ohmic resistance of the symmetrical cell and corresponds to the high frequency intercept of the Cole-Cole plots.[28, 29] Since the impedance spectroscopy technique is not capable of distinguishing contributions of different components to the ohmic resistance, the resistance of the electrolyte was measured separately by four-probe DC electrical resistivity technique to determine the current collection resistance.[28] An area specific resistance of 0.25 Ohm cm^2 was estimated for the thickness of the electrolyte (180μm) utilized for the fabrication of the symmetrical cells. As it is shown in Figure 3 for 50

vol% LSM – 50 vol% YSZ cathodes sintered at various temperatures, high frequency intercepts of the Cole-Cole plots correspond to 0.25 Ohm cm^2. Similar behavior was observed with all compositions investigated in this study. Therefore, the current collection resistance was negligible for all of the fabricated composite cathodes.

Distinct characteristic relaxation frequencies of the processes inducing polarization in the composite cathodes gave rise to two distinguishable polarization arcs in the Cole-Cole plots and two corresponding characteristic relaxation frequencies in the Bode plots as shown in Figure 3. These properties led to reliable fitting of the impedance spectra to the proposed equivalent circuit model.

Magnitudes of the high and low frequency arcs were compiled to demonstrate their change with the cathode composition and the sintering temperature as shown in Figure 4. The magnitude of the high frequency arc decreased while the connection of the LSM and YSZ phases of the composite cathodes was developed upon sintering. Percolation of both LSM and YSZ phases were required for adequate electronic and ionic conductivity, respectively. Although it would allow sintering of the LSM particles and formation of their percolation, temperatures below 1100^oC were not sufficient to provide the required sintering of the YSZ phase. Moreover, an efficient interface could not be formed between LSM and YSZ particles. Therefore, the charge transfer between LSM and YSZ phases retarded the electrochemical performance of the cathodes and gave rise to the electrode polarizations in the symmetrical cells sintered below 1100^oC. As the percolated LSM phase lacks ionic conductivity, the electrochemical activity of the cathodes was limited with the TPBs interfacing the electrolyte and the LSM grains. Thus, all compositions exhibited similar polarization resistances with the symmetrical cells sintered below

1100^{o}C.[10] Although increasing LSM content improved the sintering at lower temperatures as observed in the scanning electron micrographs, it was not sufficient to complete the development of the composite cathode microstructures with percolating LSM and YSZ phases. Increasing LSM content also led to the growth of the grains. Thus, the surface processes tended to retard the electrochemical performance of their symmetrical cells sintered at lower temperatures and gave rise to the low frequency arc as shown in Figure 4c. Sintering temperature has a more pronounced effect on the growth of the grains as it was observed in the scanning electron micrographs. The effect of grain growth gave rise to significant changes in the microstructure of the composite cathodes sintered above 1150^{o}C and resulted in retarded surface kinetics and larger low frequency arcs. On the other hand, the elevated sintering temperatures allowed achieving a well-connected network of the YSZ grains. The formed network of the YSZ grains led to an expansion of the TPBs from YSZ electrolyte – LSM grain interface to three-dimensional interface of the percolating YSZ and LSM networks. Hence, the high frequency arc demonstrated a decreasing trend with increasing temperature while the YSZ and LSM point-to-point contacts evolve to face-to-face contacts. However, further increase of the sintering temperature resulted in the growth of both LSM and YSZ grains with smaller and closed porosity. Therefore, this further development gave rise to loss of the TPBs. These changes result in a significant increase in the high frequency arc since it also resembles the transfer of the charges between the TPBs and the YSZ grains. It can be concluded that the trade-off between the development of the LSM-YSZ composite microstructure with percolating constituent phases and densification/coarsening of its microstructure determines the magnitude of the polarization resistances of the LSM-YSZ

cathodes.[22, 30, 31] While the efficient contact between LSM and YSZ grains as well as their percolation can enhance the high frequency processes and minimize the corresponding arc, their fine grains with high surface area can improve the low frequency processes and lower the related polarization resistance. Hence, the desired features of an LSM-YSZ cathode, including surface area, percolated open pore structure and integrity of LSM and YSZ phases, can be satisfied by optimizing the processing parameters.

The polarization arcs observed in the impedance spectra of the LSM-YSZ composite cathodes were investigated and reported also by other researchers.[8, 31, 32] The charge transfer between the LSM and YSZ phases induce a polarization arc with a characteristic relaxation frequency in the range of 10^3 Hz-10^5 Hz and a corresponding activation energy in the range of 0.98eV-1.4eV. Further analyses of the observed polarization arcs were performed by identifying their activation energies in this study. Hence, temperature dependences of the impedance spectra were measured for each symmetrical cell configuration and the activation energies of the deconvoluted polarization arcs were calculated as shown in Figure 5. Since the observed high frequency arcs and their activation energies correspond to the reported mechanism, it suggests that the charge transfer between the LSM and YSZ phases induce this particular polarization arc. It was also reported that the surface processes (i.e. dissociative adsorption and surface diffusion of oxygen) give rise to a polarization arc with a relatively low characteristic relaxation frequency (10^1 Hz-10^2 Hz) and an activation energy in the range of 1.8eV-2.0eV.[8, 31, 33] Since the low frequency arc determined in this study demonstrated activation energies (Figure 5) and relaxation frequencies (Figure 3) in this range, it suggests that the surface processes induced the low frequency polarization arc identified in the impedance spectra.

Therefore, the revealed relationships between the deconvoluted polarization arcs, the microstructure of the LSM-YSZ composite cathodes and their processing parameters are in a good agreement.

The magnitudes of the area specific polarization resistances (ASRs) given in Figure 4(a-c) represent the impedance spectra of the symmetrical cells. Therefore, they correspond to the polarization resistances of two electrodes. Total polarization resistance of an individual cathode can be calculated by dividing the sum of the area specific polarization resistances of high and low frequency arcs to two. Although the total polarization resistance of the composite cathodes did not exhibit a significant difference with their symmetrical cells sintered between 1100^{o}C and 1200^{o}C, the cathode of 50 vol% LSM – 50 vol% YSZ sintered at 1150^{o}C demonstrated the lowest total cathode polarization resistance at 800^{o}C in air as shown in Figure 4d.

Pt paste was screen-printed on the LSM-YSZ cathodes in order to provide efficient current collection and contact for the Pt wires. The porous Pt current collector layer could contribute to the electrochemical performance of the underlying cathode layers. Thus, Pt current collector was replaced with a porous LSM layer to identify its effects on the performance of LSM-YSZ cathodes. A mixture of coarser LSM particles (0.5µm) with flake graphite was utilized for the application of a porous LSM current collection layer. A ratio of 70 vol% LSM – 30 vol% graphite was used for the preparation of the screen-printing paste. It was applied on the LSM-YSZ cathodes sintered at 1150^{o}C. Polarization resistances identical to Pt current collector were measured with the porous LSM current collector. The thickness of the LSM current collector did not give rise to the ohmic losses. Thus, it was concluded that the current collector layer did not have any effect on

the polarization resistance of the LSM-YSZ cathodes. Moreover, it demonstrated that the electrochemical activity of the investigated LSM-YSZ cathodes took place in the applied thickness (~10 µm) and did not extend to the cathode – current collector interface. However, the surface roughness of the porous LSM current collector allowed a better mechanical integration for the Pt layer than the underlying LSM-YSZ cathode. It allowed more reliable fabrication of the cells. Therefore, further experiments were performed using a porous and co-sintered porous LSM layer as a current collector for the optimized cathode of 50 vol% LSM – 50 vol % YSZ sintered at 1150^{o}C.

The optimized cathodes were performed in complete SOFCs for further evaluation of their properties. Cathode layer with the minimum polarization resistance was applied on the previously developed relatively thin YSZ electrolyte supported by a porous Ni-YSZ anode for detailed evaluations. 50 vol% LSM – 50 vol% YSZ cathode was screen-printed on the 10 µm thick electrolyte after co-sintering the electrolyte and the anode layers. The thickness of the supporting anode layer was around 300 µm after sintering. Applied LSM-YSZ cathode layer and the LSM current collector were co-sintered at 1150^{o}C. As a result, component layers were integrated to each other and complete fuel cells were obtained as shown in Figure 6.

Voltammetric measurements of the fabricated fuel cell with the optimized LSM-YSZ composite cathode exhibited relatively high power densities considering the operating conditions. Although a relatively diluted hydrogen mixture (10% H_2 in Ar) was utilized as fuel, power densities over 1.75 W/cm^2 were achieved as shown in Figure 7. Open circuit voltages over 1 V validated the gas-tightness of the thin electrolytes, while the obtained power densities confirmed the electrochemical performance of the electrodes.

The linearity of the current-voltage characteristics and the current densities of the SOFC over 5 Amps/cm^2 demonstrated that anode and cathode layers as well as their corresponding current collectors did not induce any major losses related with the transport of the reactant and product gases.

The developed SOFC was investigated at the peak power density regime as all performance limiting parameters could be revealed in the corresponding conditions. Therefore, impedance measurements were performed on the fuel cell while operating at 0.5 V. Measured impedance spectra of the developed fuel cell demonstrated that there were two polarization arcs with distinct characteristic relaxation frequencies as shown in Figure 8. It allowed distinguishing the polarization arcs from each other by fitting the experimental data to the previously proposed equivalent circuit model (Figure 3c). Deconvolution of the impedance spectra revealed that the high frequency arc (10^3-10^4) represents the anode activation processes while the cathode processes gave rise to the low frequency arc (10^1-10^2) as suggested by the activation energies as well as corresponding frequencies reported by other researchers.[8, 31, 34] Impedance spectrum of the cathode layer measured in the symmetrical cell configuration was superimposed on the impedance spectrum of its complete fuel cell for a comparison. Resistance of the deconvoluted cathode polarization arc was lower than the total polarization resistance of the cathode measured in symmetrical cell configuration. Even though the high frequency arc induced by the cathode could not be distinguished in the SOFC configuration due to the dominating anode processes in the corresponding frequency range, low frequency arc was observed clearly. The slight decrease was observed in the characteristic frequency of the low frequency arc of the impedance spectrum of the cathode on the fuel cell as shown in

Figure 8b. Thus, it was obvious that the polarization characteristics of the developed LSM-YSZ composite cathode underwent distinguishable changes when evaluated on complete SOFC. The fuel cell was measured under operating electrical voltage (0.5 V) and current load instead of open circuit voltage conditions of the symmetrical cell configuration. The decrease in the polarization resistance of the cathode as well as the decrease in the characteristic frequency of the corresponding dominating arc suggests that the electrochemical performance of the LSM-YSZ composite cathode improved when employed in a fuel cell with relatively low total cell resistance. These findings are in a good agreement with the reported conditioning effect of the cathodic current treatment on the LSM based SOFC cathodes.[9, 31, 35]

4. Summary and conclusions

The effects of the processing parameters on the developed composite LSM-YSZ microstructures were identified. Analysis of the symmetrical cathode cells by impedance spectroscopy was an effective technique since it allowed correlating microstructural properties of the LSM-YSZ composites with the electrochemical performance of their cathodes. Two distinct polarization mechanisms were identified as a result of the analyses performed on the symmetrical cell configuration. Both polarization resistances decreased as the composite microstructures were developed; however, further densification and coarsening of the composite grains gave rise to the magnitude of the polarization resistances. A strong correlation exists between the processing parameters of the LSM-YSZ composites and the electrochemical performance of their cathodes. The findings demonstrated that the sintering temperature and the composition were influential

parameters. They result in formation of the microstructures with distinct features. Therefore, they give rise to significant differences in the magnitudes of the high and low frequency polarization resistances. The polarization induced by the high frequency processes (i.e. charge transfer) requires efficient connection between the constituent phases and their continuous percolation. Sintering at elevated temperatures as well as higher LSM content may help these developments. However, growth of the composite grains is inevitable during high temperature sintering and it leads to retarded surface processes and loss of TPBs. As a result, it gives rise to the polarization resistances induced by the low frequency processes. These competing phenomena lead to the minimum total polarization resistances of each cathode configuration depending on the particle characteristics, composition and sintering parameters. In this study, a minimum total cathode polarization resistance of ~0.040 Ohm cm^2 was achieved at 800^oC in air on the symmetrical cathode cells fabricated using the selected initial powders and optimized processing parameters. Further evaluation of the cathode configuration with the optimum performance was carried out on complete SOFCs based on anode supported thin YSZ electrolytes. The results validated the pursued optimization approach as relatively high power densities (~1.76 W/cm^2) were demonstrated at 800^oC using a diluted hydrogen mixture (10% H_2) as fuel and air as oxidizer.

Acknowledgements

This work was supported by a grant of the AFRL under contract no. FA4819-09-C-0018. Utilization of SEM facilities at the Graduate Center for Materials Research (MRC) of Missouri S&T is greatly acknowledged.

References

1. F. Zhao and A. V. Virkar, *J. Power Sources*, **141**, 79 (2005).

2. N. Q. Minh, *Solid State Ionics*, **174**, 271 (2004).

3. H. Yakabe, M. Hishinuma, M. Uratani, Y. Matsuzaki and I. Yasuda, *J. Power Sources*, **86**, 423 (2000).

4. C. Xia and M. Liu, *Adv. Mater.*, **14**, 521 (2001).

5. L. Nie, M. Liu, Y. Zhang and M. Liu, *J. Power Sources*, **195**, 4704 (2010).

6. T. Tsai, E. Perry and S. Barnett, *J. Electrochem. Soc.*, **144**, L130 (1997).

7. Y. Ji, J. A. Kilner and M. F. Carolan, *Solid State Ionics*, **176**, 937 (2005).

8. J.-D. Kim, G.-D. Kim, J.-W. Moon, Y.-I. Park, W.-H. Lee, K. Kobayashi, M. Nagai and C.-E. Kim, *Solid State Ionics*, **143**, 379 (2001).

9. Y. J. Leng, S. H. Chan, K. A. Khor and S. P. Jiang, *J. Appl. Electrochem.,* **34**, 409 (2004).

10. H. S. Song, W. H. Kim, S. H. Hyun and J. Moon, *J. Electroceramics,* **17**, 759 (2006).

11. O. Yamamoto, *Electrochim. Acta*, **45**, 2423 (2000).

12. J. P. P. Huijsmans, F. P. F. van Berkel and G. M. Christie, *J. Power Sources*, **71**, 107 (1998).

13. M. J. Jorgensen, S. Primdahl, C. Bagger and M. Mogensen, *Solid State Ionics*, **139**, 1 (2001).

14. T. Kenjo and M. Nishiya, *Solid State Ionics*, **57**, 295 (1992).

15. M. Juhl, S. Primdahl, C. Manon and M. Mogensen, *J. Power Sources*, **61**, 173 (1996).

16. A. Mitterdorfer and L. J. Gauckler, *Solid State Ionics*, **111**, 185 (1998).

17. C. C. T. Yang, W. C. J. Wei and A. Roosen, *J. Am. Ceram. Soc.*, **87**, 1110 (2004).

18. S. Bebelis, N. Kotsionopoulos, A. Mai and F. Tietz, *J. Appl. Electrochem.,* **37**, 15 (2007).

19. C. Clausen, C. Bagger, J. B. Bilde-Sorensen and A. Horsewell, *Solid State Ionics*, **70-71**, 59 (1994).

20. T. Tsai and S. A. Barnett, *Solid State Ionics*, **93**, 207 (1997).

21. S. P. Jiang, J. G. Love, J. P. Zhang, M. Hoang, Y. Ramprakash, A. E. Hughes and S. P. S. Badwal, *Solid State Ionics*, **121**, 1 (1999).

22. A. Chen, J. R. Smith, K. L. Duncan, R. T. DeHoff, K. S. Jones and E. D. Wachsman, *J. Electrochem. Soc.*, **157**, B1624 (2010).

23. C. Chervin, R. S. Glass and S. M. Kauzlarich, *Solid State Ionics*, **176**, 17 (2005).

24. F. W. Poulsen and N. van der Puil, *Solid State Ionics*, **53-56**, 177 (2005).

25. F. T. Ciacchi, K. M. Crane and S. P. S. Badwal, *Solid State Ionics*, **73**, 49 (1994).

26. W. Huebner, D. M. Reed, H. U. Anderson, in Proceedings of the Fifth International Symposium SOFC, U. Stimming, S. C. Singhal, H. Tagawa and W. Lehnert, Editors, PV 97-40, p. 411, The Electrochemical Society Proceedings Series, Pennington, NJ (1997).

27. A. Sarikaya, V. Petrovsky and F. Dogan, *Int. J. Hydrogen Energ.*, **37**, 11370 (2012).

28. A. Sarikaya, V. Petrovsky and F. Dogan, *J. Mater. Res.*, **27**, 2024 (2012).

29. Z. Wang, N. Zhang, J. Qiao, K. Sun and P. Xu, *Electrochem. Commun.*, **11**, 1120 (2009).

30. J. Mertens, V. A. C. Haanappel, C. Wedershoven and H.-P. Buchkremer, *J. Fuel Cell Sci. Technol.*, **3**, 415 (2006).

31. M. J. Jorgensen and M. Mogensen, *J. Electrochem. Soc.*, **148**, A433 (2001).

32. E. P. Murray, T. Tsai and S. A. Barnett, *Solid State Ionics*, **110**, 235 (1998).

33. E. Siebert, A. Hammouche and M. Kleitz, *Electrochem. Acta*, **40,** 1741 (1995).

34. A. Hauch, S. D. Ebbesen, S. H. Jensen and M. Mogensen, *J. Electrochem. Soc.*, **155**, B1184 (2008).

35. X. J. Chen, K. A. Khor and S. H. Chan, *J. Power Sources*, **123**, 17 (2003).

Figures:

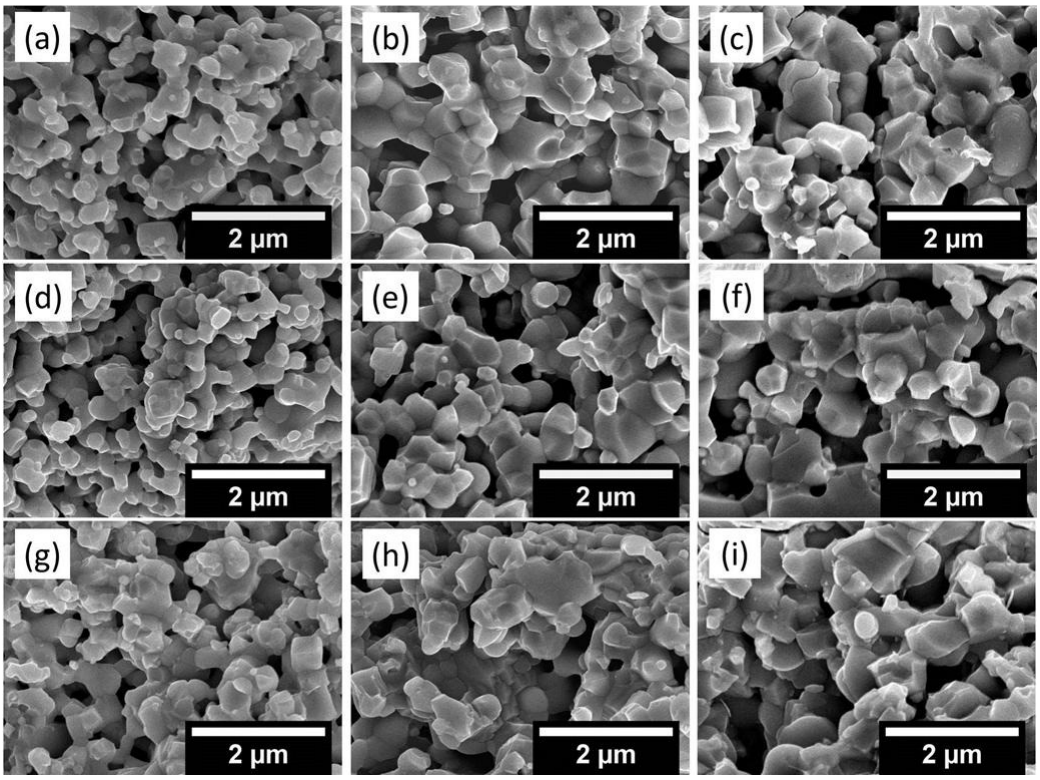

Figure 1. Scanning electron micrographs of (a-c) 45 vol% LSM – 55 vol% YSZ, (d-f) 50 vol% LSM – 50 vol% YSZ and (g-i) 55 vol% LSM – 45 vol% YSZ cathodes sintered at (a, d, g) 1100oC, (b, e, h) 1150^{o}C and (c, f, i) 1200^{o}C for two hours.

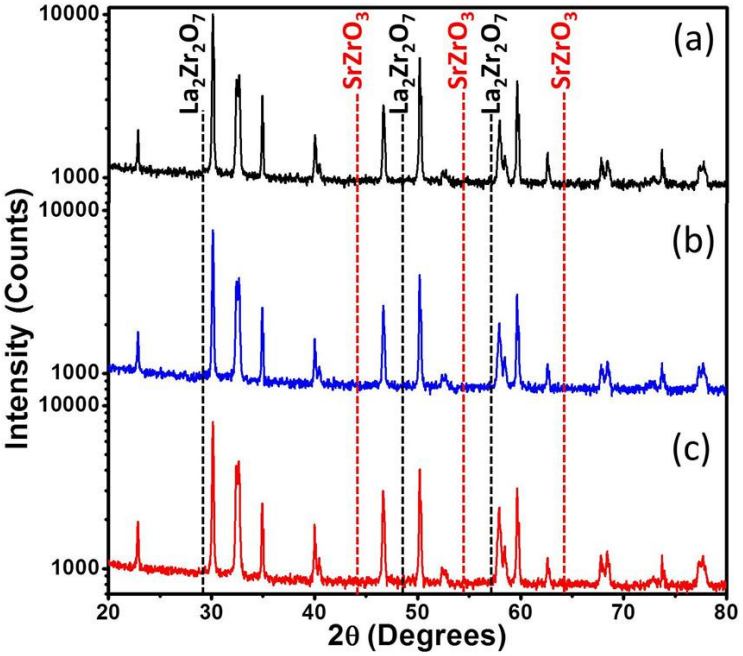

Figure 2. X-ray diffraction spectra of (a) 45 vol% LSM – 55 vol% YSZ, (b) 50 vol% LSM – 50 vol% YSZ and (c) 55 vol% LSM – 45 vol% YSZ cathodes sintered at 1250oC for two hours.

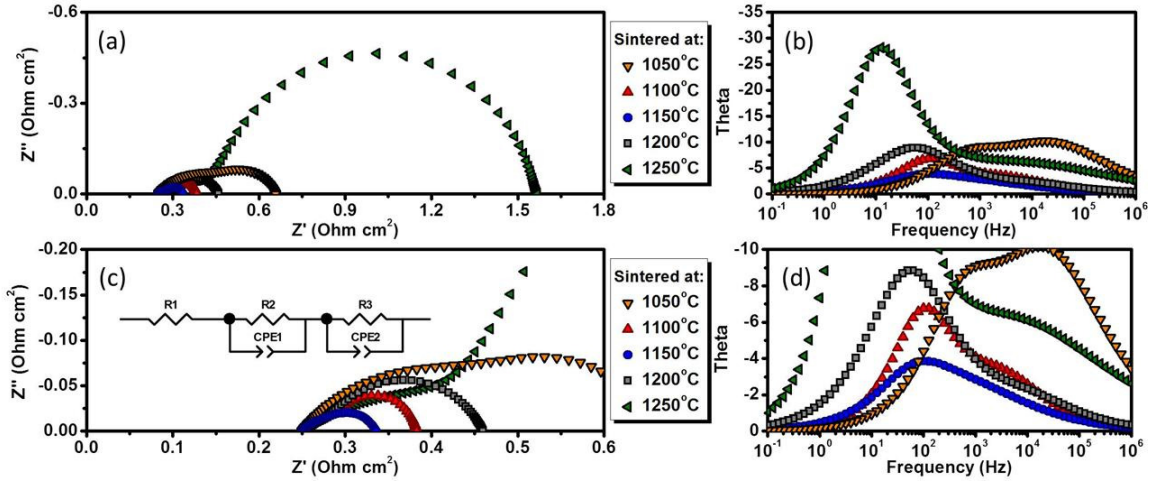

Figure 3. (a, c) Cole-Cole plots and (b, d) Bode plots calculated from the measured impedance spectra of the symmetrical 50 vol% LSM – 50 vol% YSZ cathode cells sintered at various temperatures. Note that all of the measurements were performed at 800°C in air and the equivalent circuit model used for the characterization of the impedance spectra is demonstrated in (c).

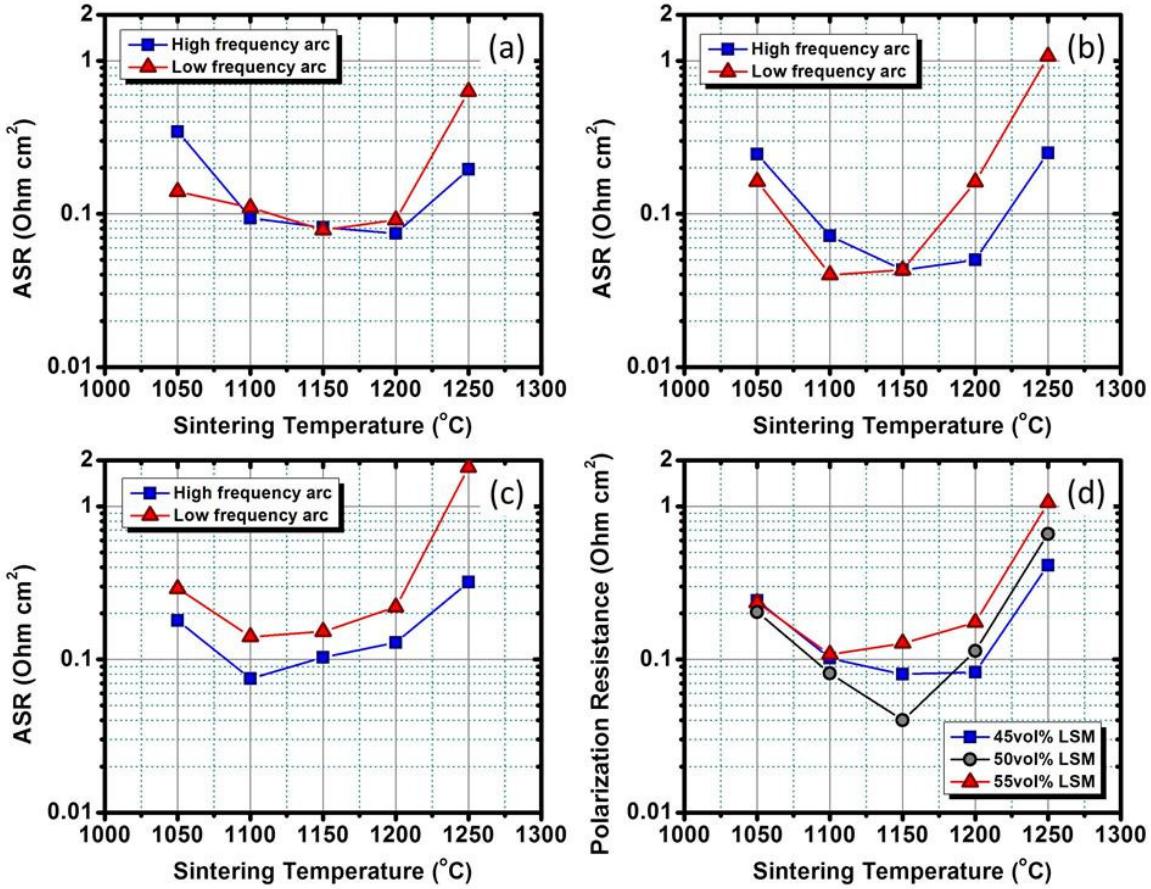

Figure 4. Magnitudes of the area specific polarization resistances of the characterized high and low frequency arcs from the Cole-Cole plots. Note that they are given as area specific resistances for the symmetrical cells of (a) 45 vol% LSM – 55 vol% YSZ and (b) 55 vol% LSM – 45 vol% YSZ cathodes while (d) total cathode polarization resistances are given per electrode.

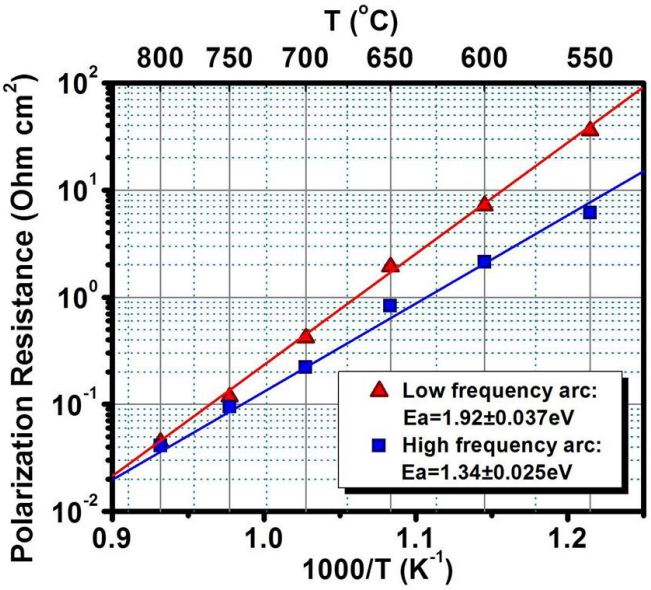

Figure 5. Temperature dependence of the deconvoluted high and low frequency arcs of the symmetrical 50 vol% LSM – 50 vol% YSZ cathode cell sintered at 1150°C.

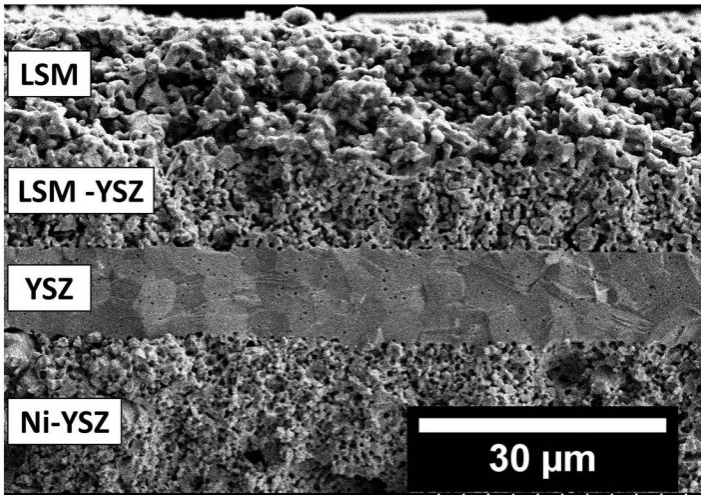

Figure 6. Scanning electron micrograph of the cross-sectional fracture surface of the developed anode supported planar SOFC after measurements.

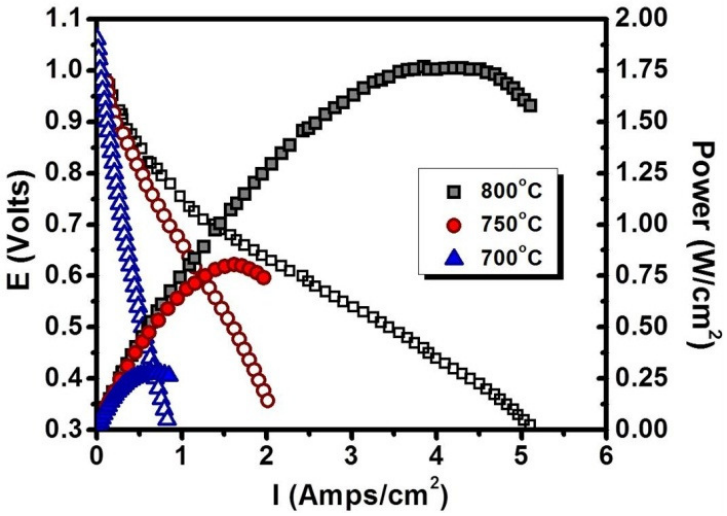

Figure 7. Voltage and power density of the fabricated SOFC as functions of current density at various temperatures.

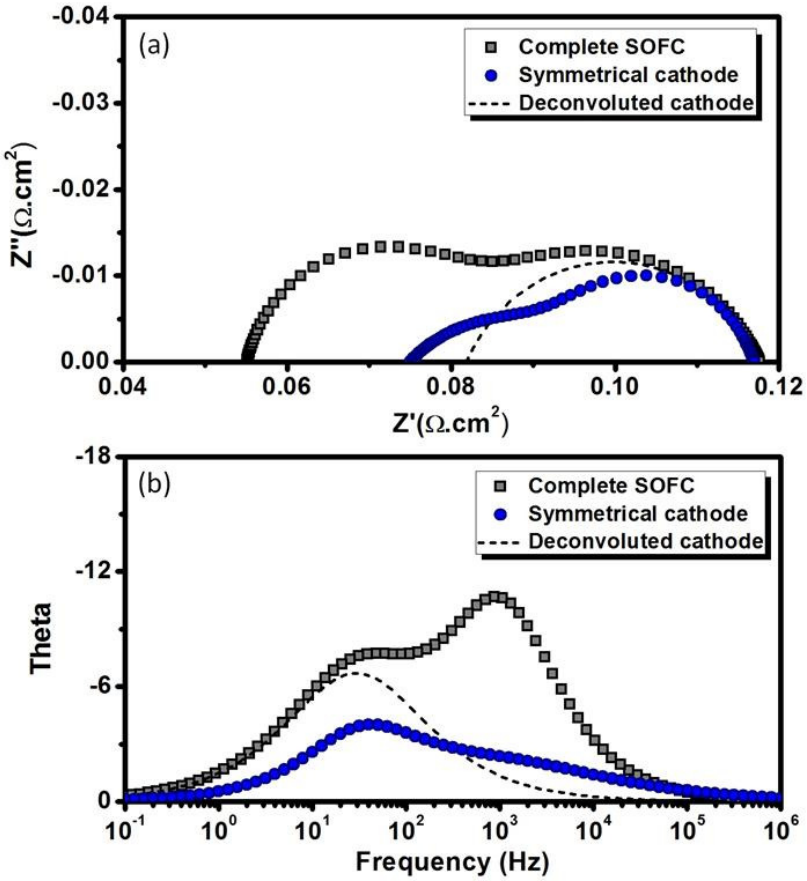

Figure 8. (a) Cole-Cole and (b) Bode plots calculated from the measured impedance spectra of the symmetrical 50 vol% LSM – 50 vol% YSZ cathode cell sintered at 1150^{o}C and the fabricated SOFC at 800^{o}C. Deconvolution of the arc associated with the cathode polarization is shown for the comparison purposes.

II. SILVER COMPOSITES AS HIGHLY STABLE CATHODE CURRENT COLLECTORS FOR SOLID OXIDE FUEL CELLS

Ayhan Sarikaya, Vladimir Petrovsky and Fatih Dogan

Department of Materials Science and Engineering,

Missouri University of Science and Technology, Rolla, MO 65409, U.S.A.

ABSTRACT

Time stability of the solid oxide fuel cells (SOFCs) has been a significant concern towards realization of their practical applications. Its operation at elevated temperatures and in oxidizing atmospheres makes the cathode current collector one of the most vulnerable components of the SOFCs. Silver and silver-based metal oxide (lanthanum-strontium manganite and yttria-stabilized zirconia) composites were investigated for the development of low-cost current collectors with long-term stability. While densification of pure silver limited its use as current collector, incorporation of oxide particles to the silver matrix led to formation of porous composites. However, addition of YSZ particles did not result in a stable porosity. Analysis of the impedance spectra allowed further investigations on the obtained microstructures and the formed contacts. No microstructural degradation has been observed in the porous Ag-LSM composite current collector and its electrical properties remained stable for over 5000 hours of measurements at 800^{o}C in air.

I. INTRODUCTION

Ohmic losses which arise due to the high resistance of the contact materials have been a vital concern for the development of solid oxide fuel cells (SOFCs).[1-3] Stability and efficiency of the current collection on the cathode side of the SOFCs is a relatively more challenging issue than the anode side especially for the intermediate temperature (600°C-800°C) SOFCs due to high temperature oxidation.[4-6] Common current collectors include ceramics (e.g. $LaCoO_3$ and $LaCrO_3$) and noble metals (e.g. Pt, Pd, Au and Ag).[7] Although ceramic materials have high stability in oxidizing conditions, their lower electrical conductivities limit their use. Noble metals such as Pt, Au or Pd are used as common current collectors stable at high temperatures while their relatively high cost makes them less desirable for use in SOFC applications.[7-10] Its relatively low cost and advantageous attributes such as high conductivity, high ductility and self-healing at operating temperatures makes Ag a good candidate for the current collection.[8,11] However, operational conditions deteriorate its structural stability and limit its use in SOFCs.[8,11-13] Operational temperatures of SOFCs (e.g. 800°C) allow sintering of Ag particles and result in nearly full density of initially porous microstructure within a relatively short time (<170 hours) with respect to the target lifetime of 40,000 hours[14] due to relatively low melting temperature of pure Ag (962°C), as shown in Fig. 1(a) and (b).[15]

Development of a porous and structurally stable Ag based current collector was aimed by this study. Since the degradation of the cathode and anode layers limits the detailed analysis of the degradation mechanisms of the current collectors, Ag based current collectors were applied on stable electrolytes as symmetrical electrodes to analyze their stability. Thus, the electrodes in this study should not be confused with actual anode

and cathode materials of SOFCs. A systematic approach was developed to analyze the stability of the current collector compositions. The measured electrical conductivities and impedance spectra were utilized to identify the rate limiting polarization mechanisms of the symmetrical cells. Identification of the bulk diffusion of the oxygen in the solid Ag as the unique polarization mechanism led to the correlation of diffusion length with the coarsening of the Ag grains and the real part of the complex polarization with the effective contact area. Porous Ag current collector was obtained by incorporating up to 25 vol% LSM (lanthanum-strontium manganite) particles while maintaining the percolation of Ag grains for sufficiently high electrical conductivity and wetting of the underlying electrolyte layer to achieve efficient current collection and stable electrical contact.

II. EXPERIMENTAL

Ag and Ag based composite inks were prepared for screen printing of the symmetrical current collectors. Since the previous studies showed that high surface area of Ag results in structural instability, [8,16] a relatively coarse (d_{50}=1.1 μm) Ag powder (Alfa Aesar, Ward Hill, MA, USA) was used for the investigations. Initial powders of the conventional LSM - yttria-stabilized zirconia (YSZ) cathode were incorporated to the pure Ag. Utilized LSM (NexTech, Columbus, OH, USA) and YSZ (8 mol% yttria-stabilized zirconia, TZ-8Y, TOSOH, Tokyo, Japan) powders have the average particle sizes of 0.5 μm and 25nm, respectively. The preparation of the inks consists of the dispersion of the oxide powders (LSM or YSZ) in a solvent (α-terpineol, Alfa Aesar, Ward Hill, MA, USA) by ultrasonication and mixing the dispersed suspension with Ag

powder and a polymeric vehicle (V006, Hearaeus, Conshohocken, PA, USA). The rheological properties of the inks were optimized for screen printing of symmetrical current collectors on YSZ electrolyte by adjusting the solvent and polymeric vehicle amounts. Symmetrical cells were prepared by screen printing of current collector inks on both sides of 180 µm thick YSZ electrolyte (8 mol% yttria-stabilized zirconia, NexTech, Columbus, OH, USA).

Electrochemical performance investigations and electrical conductivity measurements of the cells were performed using a combined potentiostat and frequency response analyzer setup (Solartron, 1470 CellTest, Mobrey, UK). Four-probe electrical conductivity measurements were carried out on 0.5cm x 3.0cm rectangular samples using four Ag leads fixed perpendicular to the longer edge of the samples at certain intervals. Electrical conductivity measurements of the YSZ electrolyte were made on rectangular YSZ samples while Ag and Ag based composites were applied on an insulating substrate (e.g. alumina) for the conductivity measurements. Impedance measurements were carried out using two-probe configuration by fixing Ag leads on either electrode of the symmetrical cells. Impedance spectra were measured in the frequency range of 0.1Hz-1MHz using an excitation voltage of 20mV and all electrical measurements were carried out in air to simulate the operational conditions of the cathode side of SOFCs. Scanning electron microscopy (SEM) techniques were employed for the microstructural characterization of the current collectors.

III. RESULTS AND DISCUSSION

SEM micrographs shown in Fig. 1 demonstrate the microstructural development of pure Ag and Ag-20 vol% YSZ composite after measurements for various times at 800^{o}C. Although pure Ag reached nearly full density by closing the initially open pores in a relatively short time, Ag-20 vol% LSM composite maintained its porous microstructure without any distinguishable grain growth and coarsening over 170 hours, as it was reported before.[15] Addition of the same volume of YSZ powder to the pure Ag formed initially open pores; however, the porous microstructure was not stable and Ag left the composite forming individual grains on the surface as shown in Fig. 1(d).

Although conductivity of 46,000 S.cm^{-1} was measured with the pure Ag at 800^{o}C, it showed a decreasing trend with increasing amount of LSM powder as shown in Fig. 2. As it is seen in the percolation curve, additions of LSM powder above 25 vol% would lower the conductivity below the target limit of the electrical conductivity which was 100 S.cm^{-1} for this study. Thus, the Ag-25 vol% LSM composition was analyzed as the highly loaded composite mixture to investigate the stability of Ag-LSM current collectors.

Ag-25 vol% LSM composite maintained its initially open porosity and microstructural stability after 170 hours of continuous electrochemical measurements simulating its operational conditions, as shown in Fig. 3. The microstructure of Ag-25 vol% LSM was similar to the microstructure of Ag-20 vol% LSM observed by the authors previously.[17]

Although electrical conductivity of the Ag-25 vol% LSM composite current collector was sufficiently high, its performance by means of forming an efficient contact with the underlying layer was crucial for the current collection in operational SOFC

configurations. The analysis of the obtained impedance spectra was utilized for further investigations of the contact interface between the current collector and the electrolyte.

Impedance spectra consist of ohmic and polarization resistances. Since ohmic resistance of symmetrical cells can be obtained from the high frequency x-axis intercepts of Cole-Cole plots,[17] ohmic and polarization resistances can be distinguished in the impedance spectra. The measured ohmic resistance involves the electrical resistances of symmetrical current collectors and the electrolyte. However, impedance spectroscopy is not capable of differentiating the contributing ohmic components. Therefore, the resistance of the electrolyte was required to be excluded from the obtained ohmic resistance in order to determine the resistance of the current collector accurately. The electrical resistance of the YSZ electrolyte was measured by four-probe electrical conductivity measurement technique and an area specific ohmic resistance (ASR) of 0.25 $Ohm.cm^2$ was calculated for 180 μm thick electrolytes at 800^oC. Since YSZ electrolyte, symmetrical pure Ag cell and symmetrical Ag-25 vol% LSM cell demonstrated the same ASR of 0.25 $Ohm.cm^2$ as shown in Fig. 4, it can be concluded that the contact resistance was stable and negligible for both Ag based current collectors.

Further analysis of the impedance data by complex nonlinear least square fitting to equivalent circuit models revealed that the impedance spectra could be interpreted using an equivalent circuit which consists of a resistor and a finite-length Warburg element with transmissive boundary conditions in series as shown in Fig. 5. It is in good agreement with the configuration of the symmetrical cell since the proposed Warburg element represents the diffusion of charged particles to a planar electrolyte.[18]

The Warburg impedance which is attributed to finite-length diffusion with transmissive boundary conditions is described by Eq. (1):

$$W = R_w \frac{\tanh\sqrt{j\omega\tau_w}}{\sqrt{j\omega\tau_w}} \quad (1)$$

where R_w is the Warburg polarization resistance and τ_w is the time constant.

The characteristic relaxation frequency of the corresponding Warburg polarization mechanism can be calculated using the following equation and correlated with the mean diffusion time of oxygen, τ, obtained from the fitting:

$$f_w = \frac{1}{(2\pi\tau_w)} \quad (2)$$

Although a good fit of the measured impedance spectra to the finite-length Warburg element with less than 1% deviation suggests that the observed polarization mechanism is dictated by diffusion, the nature of the diffusion was required to be identified for further analysis of the current collectors. Therefore, the characteristic relaxation frequencies were obtained from the fitting of the impedance spectra measured at various temperatures. Analysis of the temperature dependence of the characteristic relaxation frequency allowed determination of the activation energy for the dominating diffusion mechanism.[19-20]

The solubility and mobility of oxygen within the bulk solid Ag have been studied by other researchers.[21-25] Their investigations revealed that oxygen has high solubility and mobility in solid Ag. The activation energy for the dominating polarization mechanism, calculated from the temperature dependence of the characteristic relaxation frequency, was in a good agreement with their results and revealed that the rate-determining mechanism was the diffusion of oxygen atoms through bulk Ag as shown in Fig. 6.

Although the decreasing porosity of pure Ag could also give rise to the limitation of the transport of gases, relatively low activation energies should have been observed if the polarization was induced by the gas phase diffusion.[26] Therefore, it suggests that the bulk diffusion is the controlling transport mechanism for oxygen in solid Ag.

Thus, the following equation was used for the diffusion coefficient, $D_{O,Ag(s)}$, with reasonable accuracy: [23]

$$D_{O,Ag_{(S)}} = 4.9\times10^{-3}\exp(\frac{-0.503eV}{RT}) \quad (3)$$

Since the characteristic relaxation frequency, f_w, is not dependent on the surface area in the symmetrical cell configuration, the diffusion length of oxygen as charge carrier can be calculated according to the following equation:[27]

$$L_d = \sqrt{D\tau_w} = \sqrt{\frac{D}{2\pi f_w}} \quad (4)$$

Results of the impedance spectroscopy measurements on the symmetrical cell with pure Ag revealed that the relaxation frequency corresponding to the electrode polarization decreases with time as shown in Fig. 7(a). Diffusion length, L_d, was associated with the characteristic relaxation frequency using the diffusion constant, $D_{O,Ag(s)}$, at the measurement temperature (800^{o}C) by employing Eq. (4). Densification of initially porous Ag is reflected in the change of diffusion length which is correlated with the relaxation frequencies obtained from the fitting of impedance spectra. The shift to the lower relaxation frequencies is attributed to longer diffusion length of oxygen through larger grains of dense solid Ag as compared to shorter diffusion length of oxygen through smaller grains of initially porous Ag, as shown in Fig. 7(b). Calculated diffusion lengths are in good agreement with the grain sizes observed in the analysis of the densifying

microstructure of pure Ag, as shown in Fig. 1(a-b). The thickness of the dense pure Ag current collector on the YSZ electrolyte was measured after 600 hours of measurements at 800°C. Its measured thickness of ~38μm showed a good agreement with the calculated diffusion length of 43.4μm.

The electrical resistance of a current collector is formulated by the following equation:

$$R = \frac{1}{\sigma} \times \frac{L}{A} \tag{5}$$

The electrode polarization due to the diffusion of oxygen through bulk Ag resulted in the complex impedance, expressed by the Warburg element. The real part of this complex impedance can be resolved as Warburg resistance, Rw. Thus, it would yield an ASR normalized to the surface area of the symmetrical current collector. In this case, the conductivity component, σ, of the Eq. (5), can be described as the conductivity due to the diffusion of oxygen through solid Ag and the length component (L) can be interpreted as the diffusion length (L_d) that is expressed by the following equation:

$$ASR = \frac{1}{\sigma} \times L_d \tag{6}$$

The normalized surface area of the current collector could be assumed completely covered with a fully dense pure Ag upon densification and saturation of the diffusion length after 600 hours at 800°C in air as shown in Fig. 7. However, Ag-25 vol% LSM was not capable of providing the same coverage of the contact surface due to its porous microstructure. Thus, a coverage coefficient, α, was introduced to the Eq. (6) where it

reaches to the unity in the case of the total coverage of the electrolyte surface area with dense Ag as formulated by the following equation:

$$ASR = \frac{1}{\sigma} \times \frac{L_d}{\alpha} \quad (7)$$

The polarization resistance of pure Ag current collector demonstrated an increasing trend with time while the Ag-25 vol% LSM current collector exhibited a decreasing polarization resistance; however, the polarization resistances of both Ag based current collectors stabilized after around 300 hours of measurements at 800^{o}C. Since the conductivity due to the diffusion of oxygen atoms through solid Ag, σ, is constant for all Ag based current collectors, effective contact area can be estimated using the coverage coefficient, α, calculated using the measured ASRs and determined diffusion lengths. Therefore, the coverage coefficients of both Ag and Ag-25 vol% LSM current collectors increased with time and reached to stable values during the measurements at 800^{o}C, as shown in Fig. 8. This suggests that the Ag-25 vol% LSM composite current collector developed a better contact with the underlying electrolyte with time and covered 1.5% (α=0.015) of the available surface area while pure Ag also developed a better contact with increasing time and covered 100% (α=1) of the available surface area approximately within the same time period.

Since the samples were not exposed to elevated temperatures prior to the measurements, microstructural changes (e.g. densification and coarsening) took place as they were heated up to the measurement temperatures (e.g. 800^{o}C). As the connectivity between Ag grains and their contact with the YSZ electrolyte were developed, oxygen atoms were transferred through shorter diffusion lengths. These initial microstructural changes in Ag-25 vol% LSM composite current collector resulted in an increase in the

measured characteristic relaxation frequency which stabilized after ~300 hours. The initial increase and the saturation in the characteristic relaxation frequency are attributed to a decrease in the diffusion length followed by the stabilization of the obtained porous microstructure as shown in Fig. 7(b). On the other hand, the symmetrical cell of pure Ag exhibited a decrease in the characteristic relaxation frequency with time during the initial stage of the measurements (~300 hours) which can be interpreted as the coarsening of Ag grains and further densification of bulk Ag. There were no further changes in the characteristic relaxation frequency for the rest of measurements (>4700 hours). The densification of the Ag on the electrolyte surface led to the coverage of the total available contact area. Thus, the identified coverage coefficient, α, reached to the unity with time and a good contact was maintained during the measurements as shown in Fig. 8. In the case of Ag-25 vol% LSM composite current collector, α showed a significant increase over a period of time (~300 hours) but could not reach the unity and stabilized at 0.015. The fact that there is no degradation in the smaller contact area obtained by incorporation of LSM particles into Ag confirms the observed stable porous microstructure of the Ag-25 vol% LSM current collector shown in Fig. 3(a-b).

Although densification of Ag was hindered by the uniformly dispersed LSM particles inhibiting the grain growth, percolation of Ag grains was maintained by neck formation between Ag particles and conductive nature of Ag matrix remained unaffected by addition of LSM. A stable contact at the electrolyte interface was formed without coarsening of Ag grains or delamination of the composite electrode, although the Ag matrix contained a relatively high amount of LSM particles (25 vol%). Ag-LSM composite current collector showed no ohmic loss and a stable contact for a relatively

long period of time without any microstructural changes. The use of Ag-LSM current collector and Cr blocking feature of LSM may also realize the use of relatively inexpensive Cr containing ferritic steel as interconnect material to build SOFC stacks.[7]

IV. CONCLUSIONS

Analysis of the microstructures using scanning electron microscopy and electrical measurements of symmetrical cells by impedance spectroscopy demonstrated that highly stable silver based current collectors for cathodes of SOFCs were obtained by incorporation of LSM particles into the Ag matrix. Addition of LSM terminated the densification of Ag particles and led to a stable porous microstructure of the composite current collector while the ohmic resistance remained unchanged after >5000 hours of measurements at 800^{o}C in air. Further studies will focus on evaluation of Ag-LSM current collectors on symmetrical cathode layers, complete fuel cells and stacks.

ACKNOWLEDGEMENTS

This work was supported by a grant of the AFRL under contract no. FA4819-09-C-0018. Utilization of SEM facilities at the Graduate Center for Materials Research (MRC) of Missouri S&T is greatly acknowledged.

REFERENCES

1. W. Schafer, A. Koch, U. Herold-Schmidt, and D. Stolten: Materials, interfaces and production techniques for planar solid oxide fuel cells. *Solid State Ionics,* **86-88,** 1235 (1996).

2. S. Koch and P.V. Hendriksen: Contact resistance at ceramic interfaces and its dependence on mechanical load. *Solid State Ionics* **168,** 1 (2004).

3. XD. Zhou, L.R. Pederson, J.W. Templeton, and J.W. Stevenson: Electrochemical performance and stability of the cathode for solid oxide fuel cells. *J. Electrochem. Soc.* **157**, B220 (2010).

4. K. Huang, P.Y. Hou, J.B. Goodenough: Characterization of iron-based alloy interconnects for reduced temperature solid oxide fuel cells. *Solid State Ionics* **129**, 237 (2000).

5. J. Piron-Abellan, V. Shemet, F. Tietz, L. Singheiser, and W.J. Quadakkers: Ferritic steel interconnect for reduced temperature SOFC, in Proceedings of the Seventh International Symposium on Solid Oxide Fuel Cells, edited by H. Yokokawa, and S.C. Singhal (PV 2001-16, The Electrochemical Proceedings Series, Pennington, NJ, USA, 2001) p. 811.

6. Z. Yang, K.S. Weil, D.M. Paxton and J.W. Stevenson: Selection and evaluation of heat-resistant alloys for SOFC interconnect applications. *J. Electrochem. Soc.* **150**, A1188 (2003).

7. L.T. Wilkinson, and J.H. Zhu: Ag-perovskite composite materials for SOFC cathode–interconnect contact. *J. Electrochem. Soc.* **156**, B905-B912 (2009).

8. Z. Yang, G. Xia, P. Singh, and J.W. Stevenson: Electrical contacts between cathodes and metallic interconnects in solid oxide fuel cells. *J. Power Sources* **155,** 246 (2006).

9. S.P. Simner, M.D. Anderson, J.E. Coleman, and J.W. Stevenson: Performance of a novel La(Sr)Fe(Co)O_3–Ag SOFC cathode. *J. Power Sources* **161,** 115 (2006).

10. S.P. Simner, M.D. Anderson, L.R. Pederson, and J.W. Stevenson: Performance variability of La(Sr)FeO_3 SOFC cathode with Pt, Ag, and Au current collectors. J. Electrochem. Soc. **152**, A1851 (2005).

11. T.B. Sheppard and B.S.J. Kang: Development of Candidate Silver Cermet Contact Materials for Cathode Side in Solid Oxide Fuel Cell, in Proceedings of Materials Science and Technology Conference (MS&T) 2007, (PV 2007-2, Detroit, MI, USA, 2007) p. 1209.

12. P. Singh, Z. Yang, V. Viswanathan, and J.W. Stevenson: Observations on the structural degradation of silver during simultaneous exposure to oxidizing and reducing environments. *J. Mater. Eng. Perform.* **13**, 287 (2004).

13. M. Camaratta and E.D. Wachsman: Silver-bismuth oxide cathodes for IT-SOFCs; Part I-microstructural instability. *Solid State Ionics* **178,** 1242 (2007).

14. H.U. Anderson and F. Tietz, in High Temperature Solid Oxide Fuel Cells: Fundamentals, Design and Applications, edited by S. C. Singhal and K. Kendall, (Elsevier Advanced Technology, Oxford, UK, 2003) p. 183.

15. A. Sarikaya, V. Petrovsky, and F. Dogan: Development of a silver based current collector for SOFC cathodes. (Mater. Res. Soc. Symp. Proc. Fall 2011) *(submitted)*.

16. W.A. Meulenberg, O. Teller, U. Flesch, H.P. Buchkremer, and D. Stöver: Improved contacting by the use of silver in solid oxide fuel cells up to an operating temperature of 800°C. *J. Mater. Sci.* **36,** 3189 (2001).

17. Z. Wang, N. Zhang, J. Qiao, K. Sun, and P. Xu: Improved SOFC performance with continuously graded anode functional layer. *Electrochem. Commun.* **11**, 1120 (2009).

18. E. Barsoukov and J.R. Macdonald, *Impedance Spectroscopy: Theory, Experiment, and Applications*, (John Wiley & Sons, Inc., Hoboken, NJ, USA, 2005) p. 84.

19. S. Lanfredi, and A.C.M. Rodrigues: Impedance spectroscopy study of the electrical conductivity and dielectric constant of polycrystalline LiNbO3. *J. Appl. Phys.* **86**, 2215 (1999).

20. P. Jasinski, V. Petrovsky, T. Suzuki, and H.U. Anderson: Impedance studies of diffusion phenomena and ionic and electronic conductivity of cerium oxide. *J. Electrochem. Soc.* **152**, J27 (2005).

21. H. Möbius and B. Rohland: Oxygen-ion-conducting solid electrolytes and their applications. XIV. Effect of the electrode material on the results of electrical conductivity measurements in solid electrolytes. *Z. Chem.* **6,** 158 (1966).

22. S. Badwal, M. Bannister, and M. Murray: Non-stoichiometric oxide electrodes for solid state electrochemical devices. *J. Electroanal Chem.* **168,** 363 (1984).

23. T.A. Ramanarayanan and R.A. Rapp: The diffusivity and solubility of oxygen in liquid tin and solid silver and the diffusivity. *Metall. Mater. Trans. B.* **3,** 3239 (1972).

24. I. Kontoulis and B.C.H. Steele: Determination of oxygen diffusion in solid Ag by an electrochemical technique. *Solid State Ionics* **47**, 317 (1991).

25. JH. Park: Measuring oxygen diffusivity and solubility in solid silver with a gas-tight electrochemical cell. *Mater. Lett.* **9**, 313 (1990).

26. M. Kanezashi, J. O'Brien-Abraham, Y.S. Lin, and K. Suzuki: Gas permeation through DDR-type zeolite membranes at high temperatures. *AlChE. J.* **54**, 1478 (2008).

27. CT. Sah, *Fundamentals of Solid-State Electronics*, (World Scientific Publishing, Singapore, 1991) p. 436.

Figures:

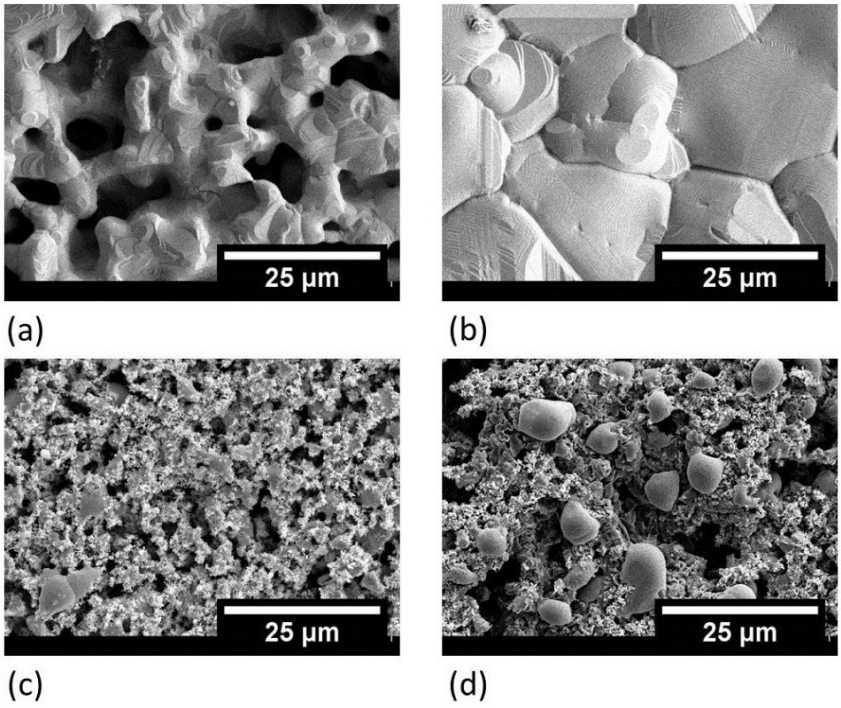

Figure 1. SEM micrographs of (a, b) pure Ag 15 and (c, d) Ag-20 vol% YSZ, both obtained after 2 hours and 170 hours of measurements at 800^{o}C, respectively.

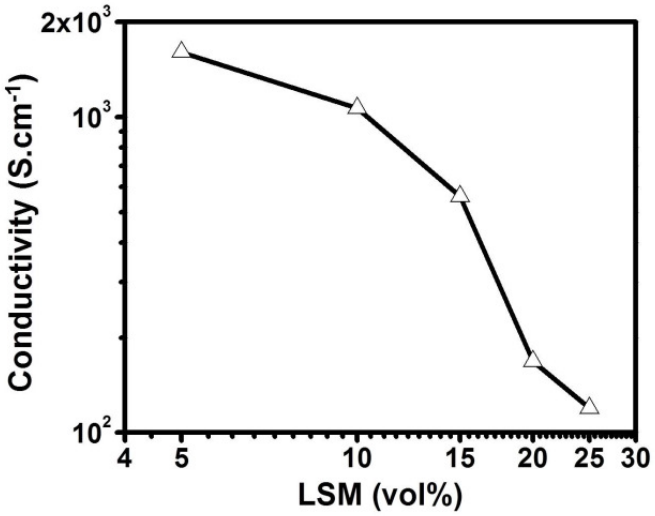

Figure 2. Electrical conductivity of Ag composites with various LSM loadings at 800°C in air.

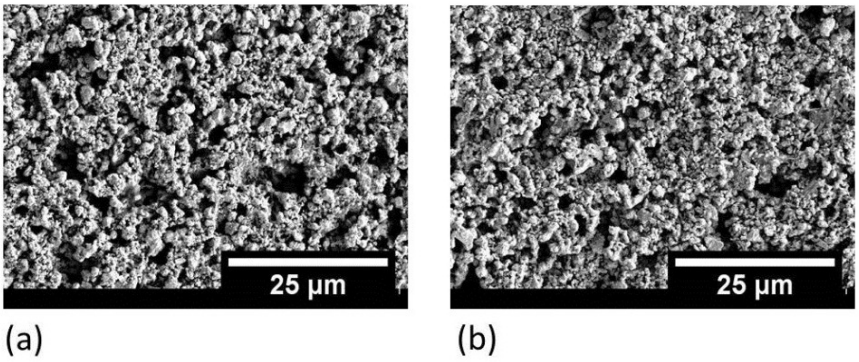

Figure 3. SEM micrographs of (a, b) Ag-25 vol% LSM obtained after 2 hours and 170 hours of measurements at 800°C, respectively.

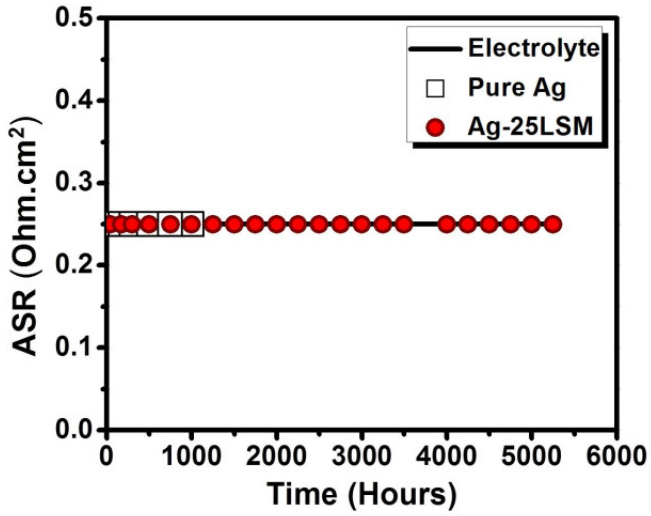

Figure 4. Area specific resistances of the YSZ electrolyte, symmetrical pure Ag cell and symmetrical Ag-25 vol% LSM cell at 800°C as a function of time.

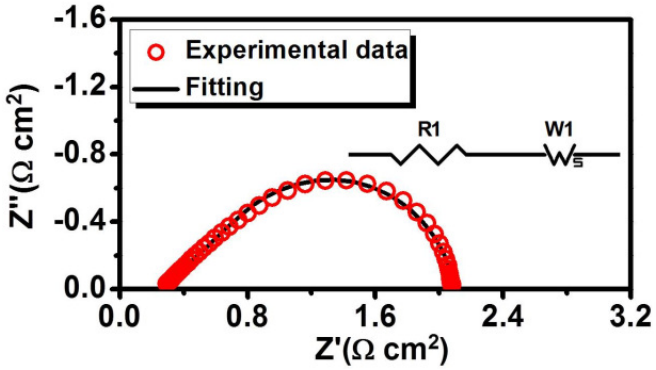

Figure 5. Cole-Cole plot of the experimental data of pure Ag measured at 800°C and its fitting according to the equivalent circuit model.

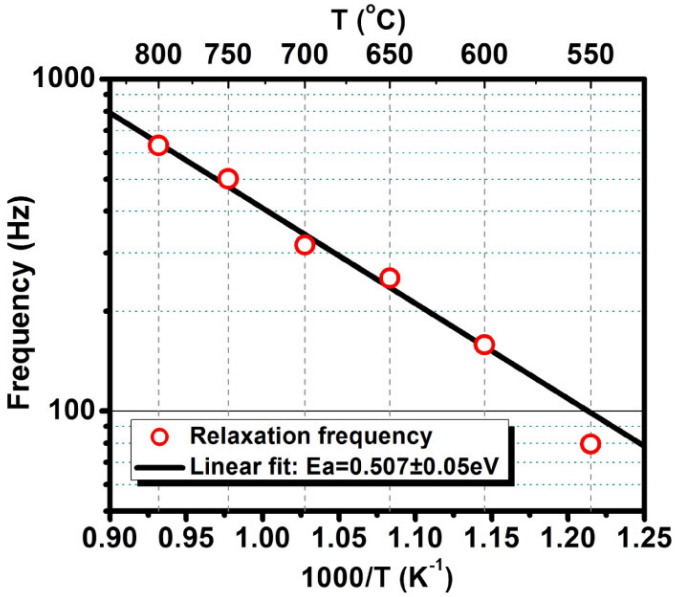

Figure 6. Temperature dependence of the characteristic relaxation frequency of Warburg impedance.

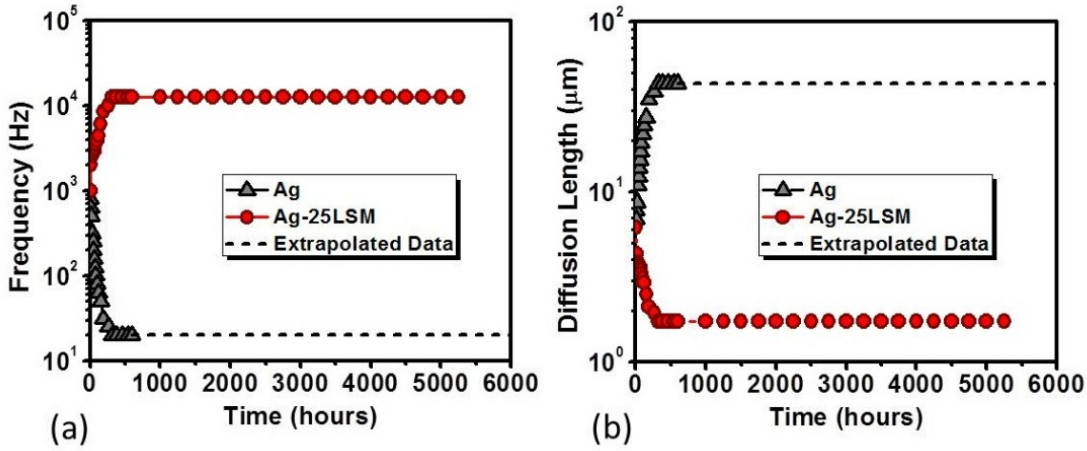

Figure 7. (a) Characteristic relaxation frequency and (b) diffusion length as functions of time, calculated from the impedance spectra of the pure Ag and Ag-25 vol% LSM cells measured at 800°C.

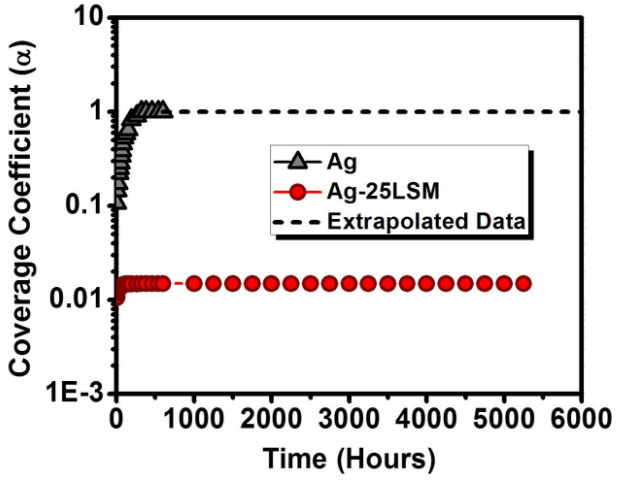

Figure 8. Change of the effective contact area represented by the calculated coverage coefficient, α, with increasing time at 800°C.

III. SILVER BASED PEROVSKITE NANOCOMPOSITES AS COMBINED CATHODE AND CURRENT COLLECTOR LAYERS FOR SOLID OXIDE FUEL CELLS

Ayhan Sarikaya, Vladimir Petrovsky and Fatih Dogan

Department of Materials Science and Engineering,

Missouri University of Science and Technology, Rolla, MO 65409, U.S.A.

Abstract

Properties of silver at elevated temperatures limit its use as a porous electrode or current collector in solid oxide fuel cell (SOFC) configurations. Its relatively low melting temperature (962^{o}C) leads to accelerated densification of silver at operating temperatures of intermediate temperature SOFCs (550^{o}C-800^{o}C). In previous studies, powder based silver composites demonstrated stable microstructures with desirable porosity and electrical conductivity during long-term testing. Although the characterized features of the silver based composites allowed their use as efficient and stable cathode current collectors, they demonstrated limited electrochemical performance as a cathode layer. In this study, nanostructured coatings of various perovskite based cathode materials (lanthanum-strontium manganite (LSM), lanthanum-strontium ferrite (LSF), lanthanum-strontium cobalt-ferrite (LSCF)) were deposited into porous silver composites by infiltration of polymeric precursors to enhance their electrode efficiencies. As a result, novel metal-matrix perovskite nanocomposites were obtained. The properties of the Ag based nanocomposites allowed their use as a combined cathode and current collector layer with significantly improved electrochemical performance and long term stability at 800^{o}C in air.

Introduction

Solid oxide fuel cells (SOFCs) are promising energy conversion devices which possess a unique combination of desirable features such as high efficiency, flexible fuel options and near-zero emissions.[1,2] Their feasible operation requires relatively high temperatures (500^{o}C-800^{o}C) which allow significantly fast reaction kinetics and enhanced electrolyte performances.[3,4]

The performance limitations in SOFCs can be specified as (i) activation polarization, (ii) ohmic losses and (iii) concentration polarization. Activation polarization arises due to the processes involved with the electrode reactions, while sum of the electrical resistance of the cell components (e.g. anode, cathode, electrolyte and current collectors) leads to ohmic losses. As the operation of the SOFCs requires efficient transport of reactant and product gases through the electrodes and the current collectors, retarded transport of gases would give rise to concentration polarization and decrease the fuel cell performance.[5-7] Therefore, anode and cathode layers are required to provide sufficient catalytic activity, ionic and electronic conductivity as well as open porosity for transport of gases. The current collectors of the electrodes also need to satisfy the requirements of enhanced electrical conductivity and porosity for the same reasons.

Although relatively high operational temperatures allow improved electrochemical reaction kinetics and yield enhanced performance of SOFCs, they limit stability of the materials used for their fabrication as they undergo microstructural degradations (e.g. densification and coarsening) or form undesired phases upon interactions with each other.[8,9] Noble metals are used as current collectors on the cathode side of the SOFCs due to their stability in oxidizing atmospheres at elevated temperatures.[10] However, their high

cost diverted researchers to studies on other alternative materials for current collector applications. Hence, oxide based materials (e.g. $LaCrO_3$ and $LaSr_xCo_{1-x}O_3$) were widely studied and employed as current collectors since they are relatively stable in oxidizing atmospheres at elevated temperatures. However, limited electrical conductivity of oxide based current collectors result in a substantial decrease in the power output of the SOFC systems due to ohmic losses during operation.

Silver has been an attractive material to minimize the ohmic losses and polarization resistances in solid oxide fuel cell (SOFC) configurations due to its highest electrical conductivity among all metals, significant ionic conductivity, solubility/diffusivity of oxygen, and catalytic activity for oxygen reduction.[11-15] Therefore, silver and silver composites were widely investigated for possible SOFC applications. However, low melting point of silver (962^{o}C) close to the operating temperatures (e.g. 800^{o}C) resulted in its densification to near complete density within a short time period and limited its use as a current collector or a cathode layer.[16]

Recent studies on silver based composites revealed that highly conductive porous electrodes can be developed by incorporating oxide particles into the silver matrix. Additions of lanthanum-strontium manganite (LSM) particles yielded stable porous microstructures while time stability could not be achieved by incorporating yttria-stabilized zirconia (YSZ) particles at 800^{o}C in air.[17] Incorporation of YSZ particles into the Ag matrix formed initially uniform and open porosity; however, structural integrity of the component materials could not be obtained. Ag grains were separated from the composite resulting in a significant grain growth as shown in Figure 1.[16] Although the electrical properties of powder based stable Ag-LSM composites allowed their use as

current collectors for SOFC cathodes, the polarization resistances were relatively high and limited their use as cathodes.

Infiltration of polymeric precursors has been an effective technique to deposit uniform layers of oxide materials both on flat substrates and porous scaffolds at temperatures significantly below the sintering temperatures of their powders (<500^{o}C).[18,19] Considering that the precursors of the catalyst materials can be easily prepared and applied, the scaffold is required to provide the other properties to form efficient electrodes. The required properties of the scaffolds include open porosity and ionic and/or electronic conductivity. Thus, polymeric precursors of NiO and LSM were successfully utilized to form nanocomposite electrodes through infiltration into porous YSZ scaffolds.[20,21]

Previously developed Ag-YSZ porous electrodes were used as scaffolds in this study, considering that they demonstrated desirable properties such as high electronic/ionic conductivity and open porosity.[16,17] Although relatively stable and porous Ag based composites were obtained with additions of LSM particles into Ag matrix, they were not utilized to avoid possible interactions between the powder based LSM and the infiltrated oxide based catalyst particles. Since they all are perovskite based materials, their interactions at elevated temperatures could lead to formation of solid solutions and undesired phases which in turn would make the interpretation of the contributing effects considerably difficult. Numerous investigations were performed on the interactions of YSZ with perovskite based cathode materials.[22,23] Although these studies demonstrated formation of undesired phases at elevated temperatures, formation of those phases at temperatures as low as 800^{o}C were not revealed. In the present study, precursors of

various perovskite-based cathode materials such as $La_{0.8}Sr_{0.2}MnO_3$ (LSM), $La_{0.6}Sr_{0.4}FeO_3$ (LSF) and $La_{0.6}Sr_{0.4}Co_{0.2}Fe_{0.8}O_3$ (LSCF) were infiltrated into porous Ag-20 vol% YSZ (Figure 1a) electrodes to obtain their composites at 800°C. Detailed analyses of the microstructures of the novel metal matrix (Ag) perovskite nanocomposite electrodes and their electrochemical properties revealed the effects of the infiltrated catalytically active oxides on the performance and stability of porous Ag electrodes.

Experimental

An ink of Ag-20 vol% YSZ composition was prepared for screen-printing using a two-stage process. A relatively fine (d_{50}=25nm) YSZ powder (8 mol% yttria-stabilized zirconia, TZ-8Y, TOSOH, Tokyo, Japan) and a coarse (d_{50}=1.1µm) Ag powder (Alfa Aesar, Ward Hill, MA, USA) were dispersed in a solvent (α-terpineol, Alfa Aesar, Ward Hill, MA, USA) by ultrasonication at the first stage. An ethyl cellulose based polymeric vehicle (V006, Hearaeus, Conshohocken, PA, USA) was added to the mixture and its rheological properties were optimized for screen printing by adjusting the ratios of the solvent and the vehicle. Prepared ink was screen printed on both sides of 180µm thick YSZ electrolytes (8 mol% yttria-stabilized zirconia, NexTech, Columbus, OH, USA) to form symmetrical cells. Ag wires were attached to the applied Ag-20 vol% YSZ electrodes and the cells were sintered for 2 hours at 800°C in air.

Precursors of perovskite based materials (LSM, LSF and LSCF) were prepared as described elsewhere.[18,19] Considering the stoichiometry of their constituent cations, appropriate amounts of lanthanum (III) nitrate hexahydrate, anhydrous strontium nitrate, manganese (II) nitrate tetrahydrate, cobalt (II) nitrate hexahydrate and iron (III) nitrate

nonahydrate salts (Alfa Aesar; Ward Hill, MA, USA) were dissolved in deionized water. Ethylene glycol was added to the aqueous solutions to obtain a cation to ethylene glycol molar ratio of 0.04. The mixture was heated to 100^{o}C while it was continuously stirred until the chelate polymers were obtained and the water content is completely removed. In order to improve the wetting behavior of the polymeric precurcors, 2-butoxyethanol was with the weight ratio of 2:1.

Obtained polymeric precursors were infiltrated into the porous Ag-20vol% YSZ electrodes of the symmetrical cells. The infiltrated cells were dried at 70^{o}C in air and heated up to 450^{o}C as illustrated in Figure 2. These steps were repeated for 20 times for each cell.

Scanning electron microscopy (SEM) techniques were employed for the analysis of the microstructures of the obtained electrodes. Investigations allowed further examination of the microstructures and the stability of the formed composite electrodes. The amount of the porosity in the obtained composites was determined by an image analysis software (ImageJ, NIST, Bethesda, MD, USA). Four-probe electrical conductivity measurements were conducted on the composite electrodes that were deposited on an insulating substrate (Al_2O_3). Electrochemical performance analyses were performed on the symmetrical cells using a combined potentiostat (CellTest 1470, Solartron, Mobrey, UK) and frequency response analyzer (1255B, Solartron, Mobrey, UK). An excitation voltage of 20 mV was applied for impedance measurements in a frequency range of 0.1 Hz to 1 MHz.

Results and discussion

Uniform distribution of the grains and a percolating pore structure were observed on the Ag based composite electrodes after 200 hours of measurements at 800^{o}C in air as shown in Figure 3. Infiltrated particles of LSM, LSF and LSCF maintained integrity of silver scaffold within the composites and improved the stability of the porous microstructure.

Detailed analysis of the microstructures after measurements demonstrated that the infiltrated catalytically active particles formed a continuous layer of fine grains (30-100nm) covering the surface of the initial Ag-YSZ composite as shown in Figure 3. Since these perovskites are relatively stable at elevated temperatures in air, they reinforced the porous microstructure of the Ag matrix and improved its stability. A porosity of 50 vol% was estimated in the initial Ag-20 vol% YSZ scaffold while all composites exhibited nearly the same porosity (~30 vol%). Considering the loading of the polymeric precursors and the yield of deposition steps, 20 vol% of the composites was expected to be occupied by the deposited oxide layers.

Since high temperature evaporation of Ag was a major concern for its use in SOFC applications, several studies were conducted to eliminate this problem. It was reported by other researchers that the evaporation of Ag thin films can be minimized and their stability can be improved by capping with an oxide layer.[24-27] Findings of the current study are in a good agreement with their conclusions that the stability of the porous microstructures of Ag based composites was improved by addition of the nanostructured continuous layers of oxides.

Further investigations on the nanocomposite electrodes were performed using their symmetrical cells. Impedance measurements on the cells allow analyzing the electrochemical performance of cathode/current collector layers.[16] The obtained data were represented in the form of Cole-Cole plots as shown in Figure 4. The impedance spectra consist of ohmic and polarization resistances. Therefore, all impedance spectra were fitted to various possible equivalent circuit models using nonlinear least square fitting method for identification of corresponding parameters. As a result, a reliable fit was achieved to the equivalent circuit model which consists of a resistor and a finite-length Warburg element with transmissive boundary conditions in series as shown in Figure 4.

The value of the R1 resembles the area specific ohmic resistance (ASR1) of the symmetrical cells. It also corresponds to the high frequency x-axis intercept of the Cole-Cole plots and involves the electrical resistances of the electrolyte and cathode/current collector layers.[16,28] However, impedance spectroscopy technique is not capable of resolving the contributions of the components to the ohmic resistance due to their relatively high characteristic relaxation frequencies at the operating temperatures (e.g. 800^{o}C). Hence, the previously determined area specific resistance of the electrolyte (0.25 Ohm cm^{2}) was subtracted from the measured ASR1 to estimate the current collection resistance (contact resistance) of the Ag based composite electrodes on the YSZ electrolytes.[16,17]

The Ag-20 vol% YSZ scaffold was highly conductive (~340 S.cm^{-1} at 800^{o}C in air) and the deposited oxide layers were not expected to improve the electrical conductivity further due to their limited intrinsic conductivities. However, analysis of the measured

impedance spectra revealed that the ASR1 values of the symmetrical cells were initially slightly higher (<0.008 Ohm cm^2) than the resistance of the electrolyte as shown in Figure 5a. The observed contact resistances of the composite cathode/current collector layers were decreased and achieved a negligible level with time. These observations are in a good agreement with our previous investigations and attributed to the improved wetting of the electrolyte by the composite layers at elevated temperatures.[16,17]

The characteristic resistance of the identified Warburg element corresponds to the resistance between the high and low frequency x-axis intercepts of the Cole-Cole plots. It represents the total polarization resistance of the composite cathode/current collector layers on the symmetrical cell.[16,17,19] Therefore, half of its value characterizes the area specific polarization resistance (ASR2) of the composite electrodes.

Investigations on the Ag-YSZ composites revealed that an area specific cathode polarization resistance of 2.875 Ohm cm^2 was achieved with symmetrical cells of Ag-20 vol% YSZ electrodes as shown in Figure 4. However, it would give rise to significantly high polarization losses and limit the electrochemical performance of the SOFCs. Thus, powder based Ag-20 vol% YSZ could not be employed as a cathode layer. Application of nanostructured perovskite coatings to the Ag-20 vol% YSZ electrodes by infiltration of polymeric precursors resulted in a significant improvement in the electrochemical performance of the electrodes. Initial polarization resistances (ASR2) of 0.25 Ohm cm^2, 0.110 Ohm cm^2 and 0.050 Ohm cm^2 were achieved with Ag based LSM, LSF and LSCF composites, respectively at 800^oC after 1 hour of measurements (Figure 4).

Polymeric precursors were completely decomposed and converted to oxides at temperatures below 400^oC.[29,30] However, the desired crystal structures of the perovskite

based materials did not form below 700^{o}C. Phase-pure perovskites were obtained after heat treatment at 800^{o}C. Therefore, conversion of the oxide particles did not require any high temperature processing and the obtained Ag based composites were not introduced to operational conditions prior to the measurements at 800^{o}C in air. Thus, further development of the microstructures took place during measurements and changes in the microstructure gave rise to the polarization resistances (ASR2). However, the polarization resistances stabilized with time (~100 hours) as the microstructural development of the porous composites completed as shown in Figure 5b.

Composites of Ag are widely investigated by other researchers. A common technique for preparation of composites is mixing powders of various oxides (e.g. YSZ, LSM, LSCF, $Sm_{0.5}Sr_{0.5}Co_3$ and Bi_2O_3) with Ag followed by partial sintering.[16,17,31-33] Even though certain stability of the porous microstructure could be achieved, percolation of the oxide particles could not be obtained due to their relatively high sintering temperatures. Another method to form Ag composites was infiltration of the solutions of Ag metal salts into porous oxide scaffolds.[34,35] Catalytically active Ag particles gave an initial rise to the electrochemical performance of the composite electrodes. However, the performance of the electrodes was not stable due to densification, coarsening and evaporation of Ag particles. The present study shows that densification of porous silver matrix could be inhibited by coating of silver with the nanostructured stable oxide layers. Enhanced microstructural stability of Ag grains and catalytic activity of the oxide layers gave rise to the electrochemical performance of the composite electrodes.

Although Warburg-type impedance suggests a diffusion limited polarization mechanism, the nature of the boundary conditions characterizes the magnitude of the

polarization. As the length of the diffusion region would identify the magnitude of the polarization in semi-infinite space, a boundary in this region would urge to a finite-length diffusion. While a reflective boundary would give rise to a completely capacitive impedance at low frequencies, a transmissive boundary would limit the impedance. The properties of the transmissive boundary would affect the measured polarization resistances.[16,36] In order to determine the nature of the polarization, the temperature dependences of the measured polarization resistances (ASR2) of the composite electrodes were investigated. Obtained activation energies were between 0.94 and 0.98 eV as shown in Figure 6. They were in a good agreement with the similar activation energies previously reported for the polarization resistances induced by transfer of oxygen from Ag to a transmissive plane.[15]

The contact of the Ag matrix does not cover the entire electrolyte surface due to its porosity. Even though nanostructured coatings were in two-dimensional contact with the electrolyte in those regions, the majority of the cathodic activity took place on the three-dimensional porous structure formed by the Ag matrix. Therefore, a possible explanation would be that the nanostructured perovskite layers function as cathodes on the porous surface of the electrodes and Ag matrix serves as the main oxygen conductor due to its significant oxygen solubility and diffusivity[11-15] as illustrated in Figure 7. The infiltrated cathode materials increased the coverage of the catalytically active sites in accordance with their ionic conductivities. As a result, LSCF grains carried oxygen atoms more efficiently while LSF and especially LSM were less efficient. Hence, the amount of the delivered oxygen atoms depends on the performance of the introduced perovskite layers. However, oxygen transfer through Ag grains induced the dominating polarization and the

transmissive nature of the interface between the Ag matrix and the electrolyte led to a Warburg-type polarization. Thus, the activation energies measured in this study were almost identical and did not resemble the activation energies of the related perovskite based cathode materials reported before.[37-40] The activation energies represent the dominating Warburg-type polarization due to the limited diffusion of oxygen through Ag grains.

Summary and conclusions

Considering the results of the detailed analyses on the novel porous metal matrix electrodes with nanostructured perovskite coatings, the microstructural stability of the porous Ag composites was significantly at the operating temperatures of the SOFCs (500^{o}C-800^{o}C). Previously developed powder based Ag matrix function both as the ionic conductor component and the current collector of the composite electrodes due to its relatively high mixed ionic and electronic conductivity. Since significantly high surface area was obtained by the nanostructured oxide coatings, deposited perovskite particles gave rise to the surface reactions required for the adsorption and reduction of oxygen for enhanced cathode performance. As a result, the composite electrodes combined desirable cathode and current collector properties such as stable and open porosity, high surface area, high electronic and ionic conductivity, and reduced electrode polarizations.

Acknowledgements

This work was supported by a grant of the AFRL under contract no. FA4819-09-C-0018. Utilization of SEM facilities at the Graduate Center for Materials Research (MRC) of Missouri S&T is greatly acknowledged.

References

1. A. B. Stambouli and E. Traversa, *Renewable Sustainable Energy Rev.,* **6**, 433 (2002).

2. M. Iwata, T. Hikosaka, M. Morita, T. Iwanari, K. Ito, K. Onda, Y. Esaki, Y. Sakaki and S. Nagata, *Solid State Ionics*, **132**, 297 (2000).

3. B. C. H. Steele, *Solid State Ionics*, **75**, 157 (1995).

4. D. J. L. Brett, A. Atkinson, N. P. Brandon and S. J. Skinner, *Chem. Soc. Rev.*, **37**, 1568 (2008).

5. S. H. Chan, K. A. Khor and Z. T. Xia, *J. Power Sources*, **93**, 130 (2001).

6. A. V. Virkar, J. Chen, C. W. Tanner and J. -W. Kim, *Solid State Ionics*, **131**, 189 (2000).

7. A. Sarikaya, V. Petrovsky and F. Dogan, *Int. J. Hydrogen Energ.*, DOI: 10.1016/j.ijhydene.2012.05.007, (2012) (in print).

8. Q. L. Liu, K. A. Khor and S. H. Chan, *J. Power Sources*, **161**, 123 (2006).

9. W. S. Yang, S. H. Hyun and S. G. Kim, *J. Mater. Sci.*, **37**, 2535 (2002).

10. L. T. Wilkinson and J. H. Zhu, *J. Electrochem. Soc.*, **156**, B905 (2009).

11. H. Möbius and B. Rohland, *Z. Chem.*, **6**, 158 (1966).

12. S. Badwal, M. Bannister and M. Murray, *J. Electroanal. Chem.*, **168**, 363 (1984).

13. T.A. Ramanarayanan and R.A. Rapp, *Metall. Mater. Trans. B*, **3**, 3239 (1972).

14. I. Kontoulis and B.C.H. Steele, *Solid State Ionics*, **47**, 317 (1991).

15. J. Van Herle and A. J. McEvoy, *J. Phys. Chem. Solids*, **55**, 339 (1994).

16. A. Sarikaya, V. Petrovsky and F. Dogan, *J. Mater. Res.*, DOI: 10.1557/jmr.2012.175, (2012) (in print).

17. A. Sarikaya, V. Petrovsky and F. Dogan, in *In-Situ Studies of Solid-Oxide Fuel-Cell Materials*, R. Maher, Editor, 1385, Materials Research Society Symposium Proceedings, Warrendale, PA (2012).

18. T. Suzuki, M. Awano, P. Jasinski, V. Petrovsky and H. U. Anderson, *Solid State Ionics*, **177**, 2071 (2006).

19. A. Buyukaksoy, V. Petrovsky and F. Dogan, *J. Electrochem. Soc.*, **159**, B68 (2012).

20. A. Buyukaksoy, V. Petrovsky and F. Dogan, *J. Electrochem. Soc.*, **159**, B232 (2012).

21. A. Buyukaksoy, V. Petrovsky and F. Dogan, *J. Electrochem. Soc.*, **159**, B666 (2012).

22. H. Y. Tu, Y. Takeda, N. Imanishi and O. Yamamoto, *Solid State Ionics*, **117**, 277 (1999).

23. O. Yamamoto, Y. Takeda, R. Kanno and M. Noda, *Solid State Ionics*, **22**, 241 (1987).

24. S. A. Barnett, *Energy*, **15**, 1 (1990).

25. L. S. Wang, E. S. Thiele and S. A. Barnett, *Solid State Ionics*, **52**, 261 (1992).

26. L. S. Wang and S. A. Barnett, *Solid State Ionics*, **61**, 273 (1993).

27. L. S. Wang and S. A. Barnett, *Solid State Ionics*, **76**, 103 (1995).

28. Z. Wang, N. Zhang, J. Qiao, K. Sun and P. Xu, *Electrochem. Commun.*, **11**, 1120 (2009).

29. T. Suzuki, M. Awano, V. Petrovsky and H. U. Anderson, *J. Am. Ceram. Soc.*, **89**, 3854 (2006).

30. P. Plonczak, M. Gazda, B. Kusz and P. Jasinski, *J. Power Sources*, **181**, 1 (2008).

31. M. Muranaka, K. Sasaki, A. Suzuki and T. Terai, *J. Electrochem. Soc.*, **156**, B743 (2009).

32. S. P. Simner, M. D. Anderson, J. W. Templeton and J. W. Stevenson, *J. Power Sources*, **168**, 236 (2007).

33. M. Camaratta and E. Wachsman, *Solid State Ionics*, **178**, 1242 (2007).

34. Y. Sakito, A. Hirano, N, Imanishi, Y. Takeda, O. Yamamoto and Y. Liu, *J. Power Sources*, **182**, 476 (2008).

35. Y. Liu, M. Mori, Y. Funahashi, Y. Fujishiro and A. Hirano, *Electrochem. Commun.*, **9**, 1918 (2007).

36. E. Barsoukov and J.R. Macdonald, *Impedance Spectroscopy: Theory, Experiment, and Applications,* pp. 84-91, John Wiley & Sons, Hoboken, NJ (2005).

37. E. P. Murray, T. Tsai and S. A. Barnett, *Solid State Ionics*, **110**, 235 (1998).

38. H. J. Hwang, J. –W. Moon, S. Lee and E. A. Lee, *J. Power Sources*, **145**, 243 (2005).

39. J. Van Herle, A. J. McEvoy and K. Ravindranathan Thampi, *Electrochim. Acta*, **41**, 1447 (1996).

40. F. S. Baumann, J. Fleig, G. Cristiani, B. Stuhlhofer, H. –U. Habermeier and J. Maier, *J. Electrochem. Soc.*, **154**, B931 (2007).

Figures:

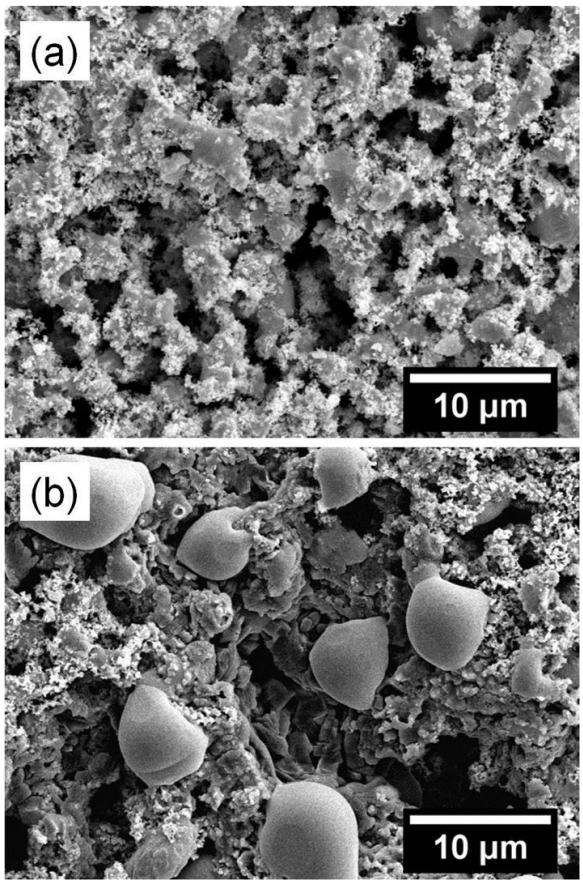

Figure 1. Scanning electron micrographs of porous Ag-20 vol% YSZ composite (a) after 2 hours of measurements and (b) after 170 hours of measurements at 800^{o}C in air.

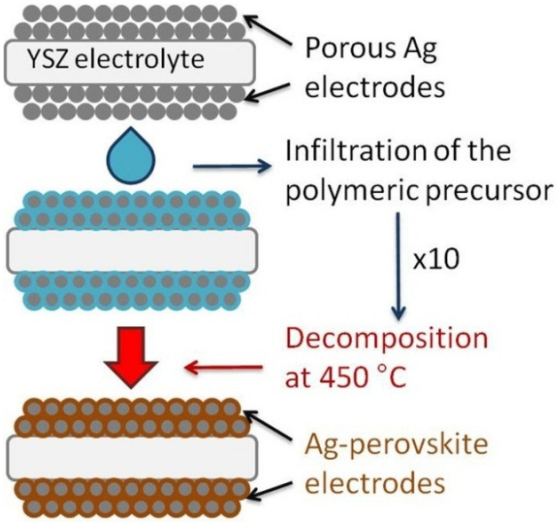

Figure 2. Illustration of the infiltration of polymeric precursors into porous Ag electrodes and their conversion to perovskite particles.

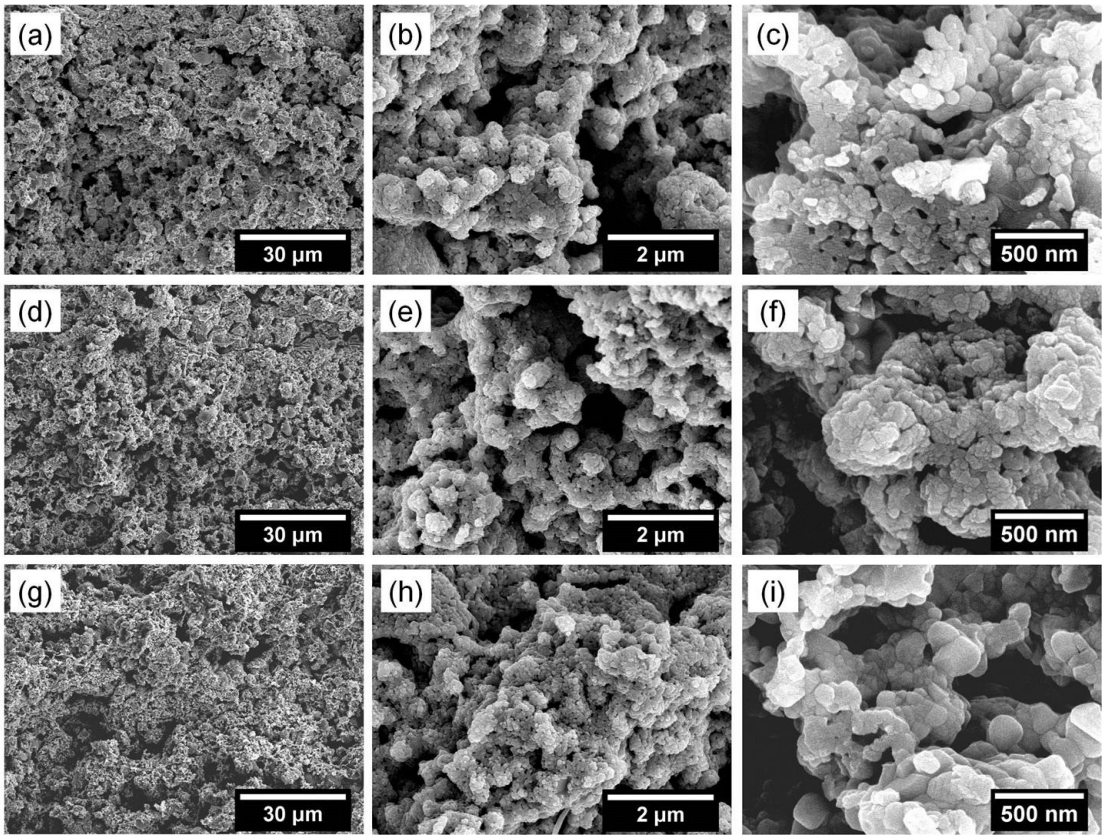

Figure 3. Scanning electron micrographs of (a, b, c) LSM, (d, e, f) LSF and (g, h, i) LSCF infiltrated porous Ag-20vol% YSZ composite electrodes after 200 hours of measurements at 800^{o}C in air.

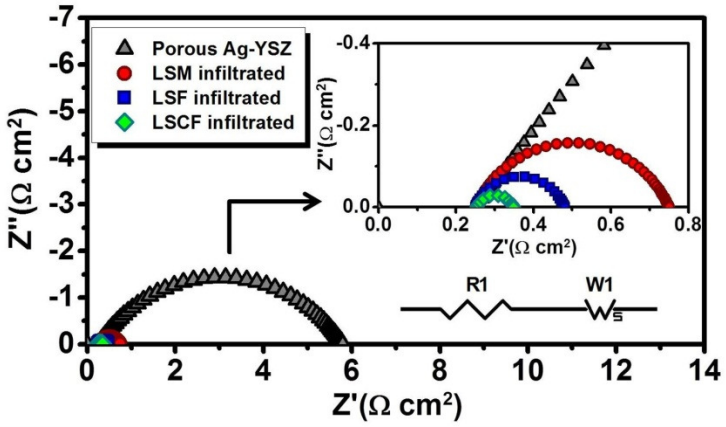

Figure 4. Cole-Cole plots calculated from the measured impedance spectra of the composite electrodes and the equivalent circuit model used for their characterization.

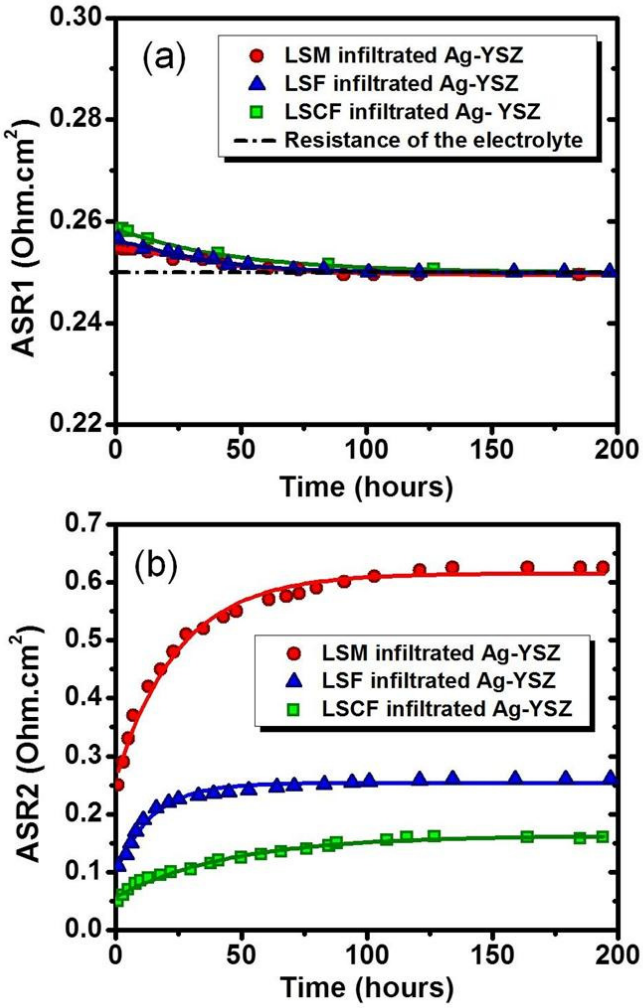

Figure 5. (a) Area specific ohmic resistances (ASR1) of the symmetrical cells and (b) polarization resistances (ASR2) of the Ag based nanocomposite cathodes as a function of time.

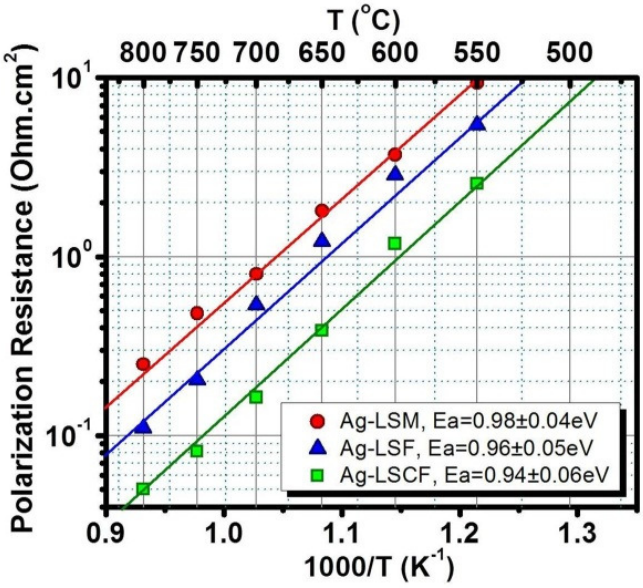

Figure 6. Temperature dependences of the cathode polarization resistances (ASR2) of the nanocomposite electrodes.

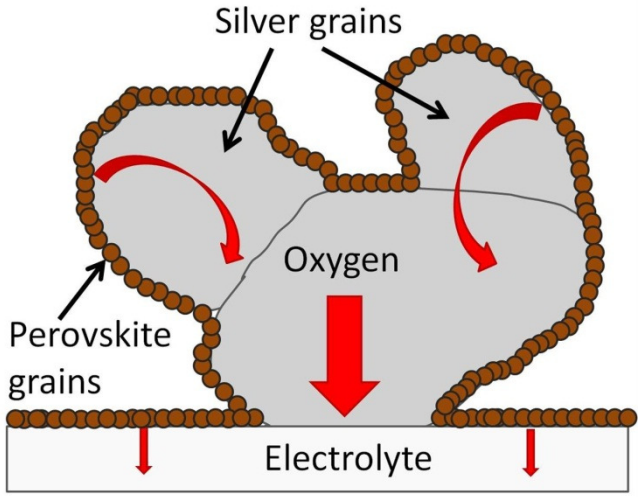

Figure 7. Illustration of the cross-section of Ag based perovskite nanocomposite electrodes on YSZ electrolytes and the possible pathway for the transport of oxygen atoms.

IV. EFFECT OF VARIOUS PORE FORMERS ON THE MICROSTRUCTURAL DEVELOPMENT OF TAPE-CAST POROUS CERAMICS

Ayhan Sarikaya, Fatih Dogan

Department of Materials Science and Engineering,

Missouri University of Science and Technology, Rolla, Missouri 65409, USA

Abstract

Various types of pore formers have been used for the fabrication of ceramics with controlled porosity. This study addresses a detailed and systematic comparison of different pore formers (e.g. graphite, polymethyl methacrylate, sucrose and polystyrene) with distinct features such as size, distribution and morphology of particles and decomposition/oxidation behavior. Investigations also involve their effect on the rheological properties of the slurries and the microstructural development of laminated porous ceramic tapes.

Morphological features of the pore former particles were characterized using laser diffraction, B.E.T. surface area measurement and scanning electron microscopy (SEM) techniques as their thermal decomposition/oxidation behavior were determined by thermogravimetric analysis (TGA) and differential thermal analysis (DTA) methods. Tape compositions were developed and optimized in order to incorporate identical volumetric loadings of the materials in the tape formulations with different pore formers for a reliable comparison of their pore forming characteristics. Porous yttria stabilized zirconia (YSZ) ceramics were fabricated without macroscopic defects (e.g. cracks, warpage and delamination) by developing heating profiles based on the identified thermal

properties of the pore formers. Characterization of the sintered porous ceramics by SEM and mercury intrusion porosimetry techniques revealed novel relationships between the physical properties of the utilized pore formers, processing parameters and final pore structures.

Keywords:

A. Tape casting; B. Porosity; Pore former; E. Fuel cells

1. Introduction

Porous ceramics are essential for a wide range of engineering applications including separation membranes [1], filters [2], piezoelectric [3] and pyroelectric ceramics [4], lightweight structural materials [5], biomaterials [6], battery separators [7] and solid oxide fuel cell (SOFC) electrodes [8-10]. Controlling the features of the porosity in ceramic microstructures is crucial to satisfy the requirements of desired applications. For instance, uniform distribution of pores gives rise to the electrochemical performance of SOFC electrodes while their connectivity/percolation allows transport of the reactant and product gases efficiently [11, 12, 13].

Although there are numerous techniques to fabricate porous ceramics such as combustion synthesis [14, 15], foaming [16], reactive infiltration [17], freeze drying [18] pyrolysis of polymeric precursors [19], electrophoretic deposition [20] and gel-casting [21], partial sintering of the ceramic tapes [22, 23] and incorporation of pyrolyzable pore formers to tape casting slurries [8, 24, 25] are commonly employed methods to fabricate tape-cast porous ceramics. In partial sintering, densification is retarded in order to obtain

a certain amount of porosity. However, partial sintering has fundamental difficulties in controlling the essential features of porosity such as shape, size, distribution and connectivity of the pores. Moreover, a desired dense ceramic matrix cannot be formed since the ceramic particles are allowed only to form neck and create a skeleton. Thus, porous ceramics fabricated by partial sintering are poor in mechanical strength [8, 26].

Pore former additions to the ceramic mixtures yield stable pores after the removal of the binder and the pore former particles. Formed pores are not removed at subsequent sintering steps [26, 27] and the final porosity of the ceramic microstructures resemble the features of the pore former particles even after sintering at elevated temperatures [26, 28, 29]. Considering that amount, size, shape and thermal properties of the pore formers can be controlled, this technique has more control over the features of the porosity as well as mechanical properties of the ceramic matrix. By controlling the properties of the pore formers, the ceramic microstructures can be also tailored by means of sintering shrinkage which is extremely crucial for the fabrication of multilayer tape-cast ceramics. Controlled sintering shrinkage and combination of tape casting with lamination also allow the fabrication of multilayer structures which involve graded porosity or integration of dense and porous ceramic layers [27].

In recent studies on the development of SOFCs, infiltration of polymeric precursors of catalytically active materials into porous 8 mol% yttria stabilized zirconia (YSZ) electrodes has been a critical step for fuel cell fabrication [30-32]. Porous YSZ electrodes are required to provide sufficient porosity to allow infiltration of the precursors and transport of the reactant/product gases while affording structural integrity to maintain

conductivity of oxygen ions. Hence, the desired YSZ electrode microstructure involves a dense matrix with a controlled pore structure.

Electrode tapes are laminated on either side of an electrolyte tape and co-sintered prior to the infiltration steps. Formation of pores in the electrode tapes and densification of the adjacent electrolyte layer introduces challenges impairing the integrity of their multilayer structure due to their dissimilar shrinkages. Various pore formers can be utilized to control the development of the porous electrodes. However, each pore former results in a different shrinkage profile on the tapes due to its characteristic particle morphology while it requires a controlled removal with a specific heating profile due to its particular thermal decomposition/oxidation behavior. As a result, undesired macroscopic defects such as cracks, blisters, warpage and delamination were observed as the compositions of the electrode tapes were modified to improve the performance of the SOFCs by changing the type, size and loading of the pyrolyzable pore formers. Therefore, a systematic study was needed to understand the relations between the properties of the pore formers, the resultant pore structures and the dimensional changes upon their removal and sintering. The gained knowledge would allow developing fabrication routes for defect-free (e.g. cracks, delaminations, blisters and warpage) multilayer ceramics.

Pore forming materials were selected considering their desired properties. Selection criteria included particle size and shape for a better understanding of the effect of the pore former morphology on the final pore structure, and decomposition/oxidation of pore formers with a minimum amount of residual carbon and other trace impurities that can affect the sintering behavior and properties of the YSZ matrix [33]. Selected high-purity

pore formers had distinct morphological features such as plate-like flake graphite, spherical PMMA and polystyrene, spheroidal graphite and random shaped sucrose. Moreover, they demonstrated dissimilar particle size distributions ranging from monodisperse to bimodal and polydisperse.

Even though numerous studies were conducted using graphite [8, 28, 33, 34], PMMA [26, 28, 35], sucrose [36, 37] and polystyrene [38-40] as pore formers, the processing conditions such as fabrication techniques, matrix materials, compositions and sintering profiles were not comparable and it was relatively difficult to draw any useful conclusions about their pore forming features with respect to each other. Moreover, the effect of the pore formers on the evolution of the final pore structures and the dimensional changes of the ceramics were not reported in sufficient detail towards processing of crack-free porous ceramic tapes. Therefore, a detailed comparative investigation of the pore formers is aimed by this study to reveal the relationships between their particle characteristics, processing conditions and effect on the pore structures of ceramics as well as dimensional changes during sintering of porous tape-cast ceramics.

Various techniques were employed for detailed analyses of the properties of the pore former particles such as size, shape, distribution, surface area and decomposition/oxidation behavior. The compositions of the ceramic slurries were developed for tape casting and lamination using identical volume fractions of the components for all of the pore formers for a consistent comparison. The analysis of their effects on the rheological properties of ceramic slurries in identical conditions provided additional information on their particle characteristics while characterization of their

thermal properties allowed determining heating profiles for their defect-free removal from tape-cast multilayer ceramics. Detailed investigations on the final microstructures led to a better understanding of the pore former – microstructure relationships of the sintered porous ceramics.

2. Experimental procedure

Commercially available high purity powders of flake and spheroidal graphite (Superior Graphite, Chicago, IL, USA), spherical polymethyl methacrylate (PMMA) (Sekisui, Osaka, Japan), random shaped sucrose (Alfa Aesar, Ward Hill, MA, USA) and spherical polystyrene (Alfa Aesar, Ward Hill, MA, USA) were selected. Although various starch types are also common pore formers, they were not included in this study due to the swelling phenomenon at elevated temperatures which makes it difficult to predict the final porosity by considering the initial properties and loading of the pore formers [41-43]. All pore formers were characterized as received except sucrose. Since it was not supplied with a certain particle specification, it was sifted through a 325 mesh screen.

Pore former particles were dispersed in an ethanol (Sigma-Aldrich, St. Louis, MO, USA) - toluene (Sigma-Aldrich, St. Louis, MO, USA) mixture and lightly coated on aluminum stubs prior to analyzing their morphologies. The coated particles were investigated using a scanning electron microscope (FE-SEM, S-4700, Hitachi, Tokyo, Japan).

Particle size distribution analysis was carried out in a laser diffraction analyzer (S3500, Microtrac, Largo, FL, USA) by using the conventional procedure [44, 45]. All

pore former particles were dispersed in distilled water at the sample preparation stage except sucrose. Sucrose was dispersed in isopropyl alcohol (Sigma-Aldrich, St. Louis, MO, USA) to avoid its solubility in water. Each measurement was repeated three times and the average was taken for the results.

Surface area measurements of the pore former particles were conducted using a surface area analyzer (NOVA 2000e, Quantachrome, Boynton Beach, FL, USA). Measurements were repeated twice and compared for their accuracy. A standard procedure was employed for the analysis of the B.E.T. (Brunauer-Emmet-Teller) gas adsorption measurement results [46].

Thermogravimetric analysis (TGA) and differential thermal analysis (DTA) of the pore formers were performed in a TGA/DTA unit (STA 409C, Netzsch, Selb, Germany) simultaneously in order to analyze their decomposition/oxidation behavior. Heating rate of 10^{o}C/min was used up to 1200^{o}C for the measurements in air. The same thermal analyses were performed also for a conventional binder system, polyvinyl butyral (PVB-79, Monsanto, St. Louis, MO, USA) plasticized with dioctyl phthalate (DOP, Sigma-Aldrich, St. Louis, MO, USA), as a reference for developing heating profiles for laminated ceramic tapes.

Ceramic slurries were prepared using a three stage preparation technique. In the first stage, YSZ powder (TZ-8Y, Tosoh, Tokyo, Japan), solvents (ethanol and toluene) and dispersant (KD-1, ICI, Barcelona, Spain) were mixed for one day by ball milling to achieve a homogeneously dispersed suspension. A mixture of ethanol (40 wt%) and toluene (60 wt%) was used as solvent for slurry preparation. The dispersant, KD-1, is a polyester/polyamine copolymer with an estimated molecular weight of ~10,000 g/mol

and has been efficiently used for dispersing a wide range of ceramic powders [47, 48]. In the second stage, the binder (PVB-79) and the plasticizer (DOP) were added to the slurry and milled for one day. The third stage consisted of the addition of pore formers to the slurry and further milling for one more day to achieve homogeneous distribution of the constituents. Sucrose is slightly soluble in ethanol [49] while it is insoluble in toluene [50]. The azeotropic mixture of toluene and ethanol [51] used for the slurry preparation demonstrated negligible solubility of sucrose. Therefore, sucrose particles maintained their physical features in the prepared slurries. The mixed slurries were then degassed for 5 min under vacuum prior to viscosity measurements and tape casting.

Viscosity measurements were performed to investigate the effect of the pore formers on the rheological properties of the slurries. A viscometer (VT550, Haake, Karlsruhe, Germany) was utilized for the measurements by applying shear rates ranging from 0 s^{-1} to 100 s^{-1}.

The measured thickness of the dry tapes were between 100-120µm. Tapes were laminated at 80^{o}C using a pressure of 25 MPa to obtain an average thickness of 625µm (±25µm) after lamination. The laminates were then heated in air to remove the organic content as well as the pore formers. Binder removal was conducted using a controlled heating profile to avoid macroscopic defects such as cracks, delamination and blistering. TGA analysis of the components (pore formers and binder/plasticizer) was utilized to optimize heating profiles for their defect-free burnout [27]. All samples were sintered in air at 1350^{o}C for 2h after the burnout of the pyrolyzable components (binder, plasticizer, dispersant and pore former particles).

Dimension and weight changes of the samples were measured before and after burnout and sintering steps to analyze the effect of burnout and sintering processes on the laminated tapes. Final microstructures of the porous YSZ samples were investigated using SEM on the fractured cross-sections. Porosity, pore size distribution and pore connectivity of the samples were characterized using a mercury intrusion porosimeter (PoreMaster 60, Quantachrome, Boynton Beach, FL, USA). The measurements were performed in a wide range of applied pressures [101.33 kPa-68.95 MPa] for a detailed analysis of pore structures [26, 52].

3. Results and discussion

3.1. Particle characteristics of the pore formers

Flake graphite and sucrose showed the most anisometric and highly polydisperse particles while spheroidal graphite consisted of more monodisperse particles with higher isometric features as shown in the micrographs presented in Fig. 1. Although most synthetic polymers are polydisperse [38], polystyrene showed highly monodisperse particles with relatively high spherical isometry. PMMA revealed a relatively large amount of small particles beside the large particles indicating a bimodal distribution of particles as shown in Fig. 2(c).

Quantification of the observations made on the micrographs is necessary for a better understanding of the characteristics of the pore formers. Therefore, laser diffraction measurements were performed on the pore former particles. As seen in Fig. 2., flake graphite (a) and sucrose (d) showed relatively broad number weighted particle size distributions (frequency histograms) that are in agreement with the obtained micrographs

in Fig. 1. Broad size distributions of flake graphite and sucrose particles involve deviation from ideal polydispersion as characterized by the distinguishable difference between their characteristic statistic parameters such as mode, median and average particle size as summarized in Table 1. The abundance of the smaller particles dominated the size distributions and resulted in smaller medians and average particle sizes. Since spheroidal graphite and polystyrene demonstrated relatively narrow particle size distributions, the analysis of these particles did not reveal any significant difference between the mode, the median and the average particle size. PMMA particles also showed a similarly narrow distribution; however, their tendency toward bimodal distribution resulted in considerable difference between the characteristic statistic parameters of their distribution. Although mode and median of the distribution were close to each other, higher number of small particles led to a relatively small average particle size.

Although flake graphite was expected to have higher surface area considering its relatively smaller and anisometric particles, the surface roughness of the spheroidal graphite yielded considerably high surface area as shown in Table 1. While the measured surface areas of the hydrocarbon based pore formers were substantially lower due to limited surface roughness, size and distribution of their particles determined their surface areas. Therefore, the lowest surface area was measured on polystyrene pore formers due to relatively large size and highly monodisperse particles. Although both pore formers were nearly isometric, PMMA particles demonstrated an order of magnitude higher surface area than polystyrene due to polydisperse and smaller size of particles.

3.2. Effect of the pore formers on the rheological properties of the ceramic slurries

Incorporation of pore formers results in distinguishable changes in the rheological properties of the slurries. Loading of the pore former particles in the slurries as well as their particle characteristics such as size, shape and distribution gives rise to particle to particle interactions which in turn lead to an increase in the viscosity. Thus, the recipe of slurries needs to be optimized by controlling the binder and dispersant ratios to obtain a suitable viscosity for casting of defect-free tapes. However, changing the binder loading may also alter the shrinkage of the sintered porous ceramics [27]. Since the binder itself acts as a pore former, any increase in the amount of the binder would introduce additional porosity to the tapes after the burnout process [28] and the comparison would be biased. Therefore, the slurry compositions were optimized by using the same volumetric loading of ceramic powder, dispersant, binder and pore former in ceramic tapes for a consistent comparison as shown in Table 2.

The optimization of the slurry compositions involved their resultant rheological properties such as viscosity and shear thinning behavior to perform a successful tape casting using the same amount of solvents. The optimized ratio of the solvent to the ceramic powder was determined at ~90 wt% and kept constant for all of the slurries. As a result, slurry viscosities were maintained in a reasonable range (4-20 Pa.s) for tape casting [53, 54]. A desired shear-thinning behavior of the slurries was observed with the increase of the shear rate as shown in Fig. 3.

Although addition of the pore formers to the slurries resulted in similar rheological properties, their particle characteristics gave rise to distinguishable differences in the resultant viscosities. Since relatively anisometric particles of flake graphite led to

increased particle to particle interactions, their incorporation resulted in a higher viscosity than the relatively isometric particles of spheroidal graphite. Even though both PMMA and polystyrene particles were relatively isometric, monodisperse polystyrene particles with relatively strong particle to particle interactions gave rise to the resultant viscosity of the slurry. Their significantly broad distribution especially in relatively small sizes limited the interactions of the sucrose particles. Therefore, incorporation of the sucrose particles to the slurry composition resulted in the lowest increase in the viscosity.

3.3. Thermal analysis of the pore formers

Thermal decomposition/oxidation behavior of the pore formers during the ceramic processes is determined by (i) the surrounding atmosphere, (ii) the heating rate and (iii) the temperature. Fig. 4. shows thermogravimetric curves of flake graphite, spheroidal graphite, PMMA, sucrose and polystyrene as well as PVB samples measured with a heating rate of 10^{o}C/min in air. Although both polymer based pore formers, PMMA and polystyrene, started losing mass around 165^{o}C and 250^{o}C, their fastest mass losses were observed around 265^{o}C and 350^{o}C, respectively. PVB started losing weight around 213^{o}C and its maximum decomposition and mass loss was observed around 350^{o}C. All hydrocarbon based samples showed complete decomposition below 600^{o}C as shown in Fig.4(a).

Weight loss was not observed with either graphite sample up to 600^{o}C as shown in Fig. 4(b). The initial mass losses of flake graphite and spheroidal graphite were observed around 619^{o}C and 600^{o}C, respectively. This is in a good agreement with the investigations reported in the literature [55, 56]. Oxidation of the crystalline graphite took

place at a relatively slow rate with respect to the decomposition of amorphous polymers (e.g. PMMA and polystyrene) and crystalline sucrose as summarized in Table 3. Although spheroidal graphite is expected to show faster oxidation kinetics than flake graphite considering its higher surface area (Table 1), oxidation of the flake graphite was significantly faster. The initial surface roughness of the spheroidal graphite gave rise to its initial oxidation kinetics at lower temperatures; however, the high aspect ratio and smaller size of flake graphite particles allowed its oxidation to reach higher rates and to complete at lower temperatures.

Although all hydrocarbon based pore formers and the binder decomposed considerably faster than the oxidation of the crystalline graphites, sucrose decomposed significantly slower than the PMMA, polystyrene and binder. Sucrose melted before it started losing mass as it was characterized using simultaneous TGA-DTA measurements. An endothermic effect was observed at around 160^{o}C corresponding to a melting process which was also confirmed by investigations performed on a temperature controlled hot plate. The slower decomposition kinetics of sucrose was attributed to the loss of its surface area as it was transformed to the liquid phase.

3.4. Sintering characteristics and analysis of the microstructures

Thermogravimetric analysis of the pore formers and plasticized binder allowed controlling of the burnout stages to eliminate rapid outlet of decomposition/oxidation gases and defect formation in the laminated tapes. Heating rate of 5.0^{o}C/min was applied up to the sintering temperature of 1350^{o}C after the soaking steps were applied at the identified controlled removal temperatures of the pore formers and the binder. The

identified controlled decomposition temperatures for polystyrene, PMMA and sucrose pore formers were 310^{o}C, 210^{o}C and 180^{o}C, respectively. Their samples were first heated up to the decomposition temperature of pore formers with the heating rate of 0.5^{o}C/min and held for one hour to complete the burnout followed by heating to the decomposition temperature of the binder at 320^{o}C. Since the controlled oxidation temperature of flake graphite and spheroidal graphite was identified as 600^{o}C, decomposition of the binder took place before their oxidation. Considering the sluggish oxidation of graphite, samples were kept at 600^{o}C for two hours. The samples were then heated to the sintering temperature of 1350^{o}C with the heating rate of 5.0^{o}C/min and held for two hours followed by cooling to the room temperature at a rate of 5.0^{o}C/min.

Macroscopic defects, such as warpage, delamination, and cracks were not observed in the samples after sintering. It was the evidence that casting and drying did not result in inhomogeneous tape compositions. Dimensional changes and the weight losses of the laminated tapes after removal of the pore formers and binder are summarized in Table 4. The solvents used for the slurry preparation were expected to leave the tapes upon drying prior to lamination. It was confirmed by measuring the weight of the laminated tapes before and after burnout. Measured weight losses of all five tape compositions were in a good agreement with the dry tape compositions shown in Table 2.

Although YSZ particles could not be sintered by firing at 800^{o}C for one hour after the removal of the binder and the pore formers, dimensional changes were observed in the laminates (Table 4). It is known that excess binder allows further densification and increases shrinkage in tape-cast ceramics since it forms fine closed porosity by improving the packing density of ceramic particles due to its migration before decomposition [8, 28,

33]. Therefore, the observed partial densification of the laminated tapes after removal of their pyrolyzable content was attributed to an increase of the packing density of YSZ particles by migration of the binder. Since incorporated graphite particles were removed from the tapes at relatively high temperatures (Table 3), they did not leave pores available for migration of the binder before its decomposition. Thus, the effect of the binder migration was lower for graphite containing tapes. However, hydrocarbon based pore formers decomposes earlier than the binder. It allowed the binder to migrate into the pores and increase the packing density of the YSZ particles further as summarized in Table 4. Sucrose incorporated tapes exhibited relatively high shrinkage upon removal of the pore former particles and the binder. The additional increase in the packing of the YSZ particles were attributed to the migration of the molten sucrose similar to the binder prior to its decomposition.

It is evident that the morphological features of the pore formers are replicated in the final porous microstructures as shown in Fig. 5. Isometric features of spheroidal graphite, PMMA and polystyrene particles resulted in nearly spherical pores. Flake graphite yielded anisometric pores representing its plate like geometry with the preferential orientation along the tape casting direction as sucrose also maintained its anisometry in the sintered microstructure but lost its broad particle size distribution due to melting of sucrose particles. Hence, the expected large pores left by the initial large particles of sucrose (Fig. 1(d)) were not observed in the sintered ceramics as shown in Fig. 5(d).

The volume change after sintering was around 56% for all samples except the sucrose sample as summarized in Table 5. The aforementioned thermal behavior of sucrose

resulted in an additional densification of the porous matrix due to improved packing of the YSZ particles.

Further characterization of the sintered microstructures was performed using mercury intrusion porosimetry. Although the intruded pore sizes between 2µm and 200µm were in a good agreement with the pore sizes observed in the micrographs shown in Fig. 5, significant amount of intrusion took place in a range of small pore sizes below 2µm for all samples except the sample prepared by removal of PMMA particles. Since it was previously observed in the investigations on the tape-cast YSZ electrolyte layers that near complete density can be achieved using identical sintering temperature (1350^{o}C) and time (2h), the formed porosity is attributed to the removal of the incorporated pore former particles. However, this range of the pore sizes was relatively smaller than the initial particle sizes of the pore formers shown in Fig. 6. It suggests that the pores were connected through smaller channels which allow the intrusion of mercury at elevated pressures.

Interconnected porosity can be achieved by percolation of the pore former particles [8, 28, 29]. High aspect ratio (>>1) of the particles of the flake graphite led to a percolating network by bridging of the pore former particles at the same volumetric loading [22]. Thus flake graphite allowed achieving almost completely open pores at around 35% bulk porosity. It demonstrated the highest amount of the intrusion of Hg and the lowest amount of closed porosity (~0.65%) among the fabricated porous ceramics in this study. Almost entirely open porosity achieved by one of the commonly used pyrolyzable pore formers, flake graphite, can be considered as a reference for the

comparison of pore forming characteristics of the other pore former particles at the same volumetric loading.

Spheroidal graphite samples showed the highest amount of the large pores (2µm-200µm) while sucrose samples showed the lowest amount of the large pores due to melting of its particles prior to decomposition. Higher densification of the sucrose also resulted in the lowest bulk porosity of 27.01%, as shown in Table 6. Spheroidal graphite yielded less open porosity (27.59%) than flake graphite due to its relatively isometric particles. Although PMMA yielded 27.08% bulk porosity, only 10% of the porosity was open due to disconnected PMMA particles in the initial tape. Since pores left by PMMA did not percolate, intrusion did not take place in the pore sizes below 2µm. Polystyrene particles achieved the percolation at the same volumetric loading due to their uniform size and resulted in more open porosity than PMMA although both are relatively isometric. Bimodal size distribution of PMMA particles resulted in disconnection of the final pores and the highest amount of measured closed porosity (24.38%). Moreover, although PMMA has a similar particle size distribution to the spheroidal graphite, its decomposition at lower temperatures prior to the decomposition of the binder, PVB, led to closing of the smaller pores. As the density of the matrix increased at the expense of closing small pores, the porosity left by larger PMMA particles got isolated and it gave rise to the closed porosity. The monodisperse particles of polystyrene left uniform pores surrounded with a dense matrix which resulted in 22.29% closed porosity.

Although the binder left the laminated structure earlier than both flake and spheroidal graphites, it did not result in any cracks due to structural weakening during their oxidation. Moreover, earlier removal of the binder at around 320^{o}C eliminated further

improvement of the packing of the ceramic particles in the graphite containing tapes by binder migration through the formed porosity. However, hydrocarbon based pore formers decomposing at temperatures lower than the decomposition temperature of the binder could not eliminate this phenomenon and yielded lower bulk porosities than the graphite based pore formers. Sucrose demonstrated the lowest amount of bulk porosity with its decomposition at the lowest measured decomposition temperature (~180^{o}C) while polystyrene showed higher bulk porosity than both sucrose and PMMA with its decomposition at a temperature (~310^{o}C) close to the decomposition temperature of the binder. Furthermore, both flake and spheroidal graphite yielded almost the same amount of bulk porosity (~36%) even though their particles have distinct morphological properties. As discussed earlier, the shape of the particles induced their percolation and identified the amount of open porosity; however, the amount of the bulk porosity was not significantly affected by the morphological features of the graphite based pore formers. Thus, the sequence of the removal of binder and pore formers can explain the higher bulk porosities achieved by utilizing graphite particles as pore formers (Table 6).

4. Summary and conclusions

Morphological and dimensional characteristics of pore formers were investigated using SEM micrographs and B.E.T. surface area measurements while distributions of the particle sizes were quantified using laser diffraction technique. Sucrose and flake graphite showed relatively broad size distributions with random shaped particles while spheroidal graphite, PMMA and polystyrene showed more spherical particles with narrow size distributions. Polydisperse particles of flake graphite and sucrose might be considered for

porous structures where decreased tortuosity is required with open porosity; however, melting of sucrose prior to decomposition may eliminate its pore forming capabilities.

Polymer based pore formers, PMMA and polystyrene, demonstrated the largest portion of the mass loss between 250^{o}C and 400^{o}C which was comparable to the burnout profile of the evaluated conventional binder, PVB. Completing the burnout step for all of the pyrolyzable content in such a narrow temperature range allowed completing the heating profile of the porous ceramics in a short period of time. Since the controlled burnout can be completed at temperatures as low as 350^{o}C, it may allow processing of the compositions sensitive to high temperature oxidation.

Oxidation of both flake and spheroidal graphite pore formers took place relatively slowly with respect to the hydrocarbon based pore formers. Although spheroidal graphite had a larger initial surface area, flake graphite oxidized faster than the spheroidal graphite due to its plate-like shape and smaller particles allowing higher surface area as the oxidation proceeds. Therefore, size and shape as well as surface area of the graphite particles need to be taken into account while planning heating profiles for processing of porous ceramics. Incorporation of graphite to the ceramic tapes as pore former may not require a slow heating profile for a defect-free burnout step.

Investigated pore formers acted as templates for the yielded porosities by means of pore shape, size and connectivity. Sucrose was the only exception since it lost the initial characteristics of its particles upon melting. All pore formers analyzed in this study resulted in similar amounts of volume change after sintering except sucrose. As highly isometric particles of PMMA yielded highest amount of closed porosity, anisometric particles of the flake graphite yielded highest amount of open porosity at the same

volumetric loading. The achieved bulk porosity was strongly affected by the removal sequence of the pore formers. While sucrose yielded the lowest bulk porosity with its decomposition at lower temperatures, graphite based pore formers oxidizing at elevated temperatures formed the highest amount of bulk porosity. Although the morphology of the pore former particles had a significant influence on the amount of the formed open porosity, the amount of the bulk porosity was not affected by the shape of the graphite particles.

It is demonstrated that the thermal and morphological properties of the pore formers have a vital effect on the features of resultant microstructures. Desired tape-cast porous ceramics can be fabricated without defects by using various pore formers, provided that the processing parameters are identified and adjusted accordingly. Therefore, the obtained understanding of the relationships between pore formers and resulted pore structures as well as the identified processing parameters will be utilized for the improvement of multilayer structures and the development of planar SOFCs.

Acknowledgements

This work was supported by a grant of the AFRL under contract no. FA4819-09-C-0018. Utilization of SEM facilities at the Graduate Center for Materials Research (MRC) of Missouri University of Science and Technology is greatly acknowledged.

References

[1] T. Tsuru, Inorganic porous membranes for liquid phase seperation, Separation & Purification Reviews 30 (2001) 191-220.

[2] J. She, T. Ohji, Z.-Y. Deng, Thermal shock behavior of porous silicon carbide ceramics, J. Am. Ceram. Soc. 85 (2002) 2125-2127.

[3] M. L. Dunn, M. Taya, Electromechanical properties of porous piezoelectric ceramics, J. Am. Ceram. Soc. 76 (1993) 1697-1706.

[4] C. P. Shaw, R. W. Whatmore, J. R. Alcock, Porous, functionally gradient pyroelectric materials, J. Am. Ceram. Soc. 90 (2007) 137-142.

[5] L. Yin, H. X. Peng, L. Yang, B. Su, Fabrication of three-dimensional inter-connective porous ceramics via ceramic green machining and bonding, J. Eu. Ceram. Soc. 28 (2008) 531-537.

[6] A. R. Walpole, Z. Xia, C. W. Wilson, J. T. Triffitt, P. R. Wilshaw, A novel nano-porous alumina biomaterial with potential for loading with bioactive materials, J. Biomed. Mater. Res. Part A 90 (2009) 46-54.

[7] X. Huang, Separator technologies for lithium-ion batteries, J. Solid State Electrochem. 15 (2011) 649-672.

[8] S. F. Cobin, P. S. Apté, Engineered porosity via tape casting, lamination and the percolation of pyrolyzable particulates, J. Am. Ceram. Soc. 82 (1999) 1693-1701.

[9] G. T. Chandrappa, N. Steunou, J. Livage, Macroporous crystalline vanadium oxide foam, Nature 416 (2002) 702.

[10] Z. Zivcová, E. Gregorová, W. Pabst, Low- and high-temperature processes and mechanisms in the preparation of porous ceramics via starch consolidation casting, Starch - Stärke 62 (2010) 3-10.

[11] J. R. Wilson, Barnett S. A., Solid oxide fuel cell Ni–YSZ anodes: effect of composition on microstructure and performance, Electrochem. Solid-State Lett. 11 (2008) B181-B185.

[12] D. Simwonis, F. Tietz, D. Stöver, Nickel coarsening in annealed Ni/8YSZ anode substrates for solid oxide fuel cells, Solid State Ionics 132 (2000) 241-251.

[13] A. Sarikaya, V. Petrovsky, F. Dogan, Effect of the anode microstructure on the enhanced performance of solid oxide fuel cells, Int. J. Hydrogen Energ. (2012) doi:10.1016/j.ijhydene.2012.05.007 (in press).

[14] D. Chen, B. Zhang, H. Zhuang, W. Li, Combustion synthesis of network silicon nitride porous ceramics, Ceram. Int. 28 (2003) 363-364.

[15] K. Maca, P. Dobsak, A. R. Boccaccini, Fabrication of graded porous ceramics using alumina–carbon powder mixtures, Ceram. Int. 27 (2001) 577-584.

[16] X. Mao, S. Wang, S. Shimai, Porous ceramics with tri-modal pores prepared by foaming and starch consolidation, Ceram. Int. 34 (2008) 107-112.

[17] J.-M. Qian, Z.-H. Jin, X.-W. Wang, Porous SiC ceramics fabricated by reactive infiltration of gaseous silicon into charcoal, Ceram. Int. 30 (2004) 947-951.

[18] T. Fukasawa, M. Ando, T. Ohji, S. Kanzaki, Synthesis of porous ceramics with complex pore structure by freeze-dry processing, J. Am. Ceram. Soc. 84 (2001) 230-232.

[19] Y.-W. Kim, S.-H Kim, C. Wang, C. B. Park, Fabrication of microcellular ceramics using gaseous carbon dioxide, J. Am. Ceram. Soc. 86 (2003) 2231-2233.

[20] A. Nakahira, F. Nishimura, S. Kato, M. Iwata, S. Takeda, Green fabrication of porous ceramics using an aqueous electrophoretic deposition process, J. Am. Ceram. Soc. 86 (2003) 1230-1232.

[21] Y. Gu, X. Liu, G. Meng, D. Peng, Porous YSZ ceramics by water-based gelcasting, Ceram. Int. 25 (1999) 705-709.

[22] A. Mortensen, S. Suresh, Functionally graded metals and metal-ceramic composites: part 1 - processing, Int. Mater. Rev. 40 (1995) 239-265.

[23] J. F. Yang, G. J. Zhang, T. Ohji, Porosity and microstructure control of porous ceramics by partial hot pressing, J. Mater. Res. 16 (2001) 1916-1918.

[24] S. Zhu, S. Ding, H. Xi, Q. Li, R. Wang, Preparation and characterization of SiC/cordierite composite porous ceramics, Ceram. Int. 33 (2007) 115-118.

[25] L. Hu, C.-A. Wang, Y. Huang, Porous yttria-stabilized zirconia ceramics with ultra-low thermal conductivity, J. Mater. Sci. 45 (2010) 3242-3246.

[26] H. L. Zhang, J.-F. Li, B.-P. Zhang, Microstructure and electrical properties of porous PZT ceramics derived from different pore-forming agents, Acta Mater. 55 (2007) 171-181.

[27] S. F. Corbin, J. Lee, X. Qiao, Influence of green formulation and pyrolyzable particulates on the porous microstructure and sintering characteristics of tape cast ceramics, J. Am. Ceram. Soc. 84 (2001) 41-47.

[28] M. Boaro, J. M. Vohs, R. J. Goerte, Synthesis of highly porous yttria-stabilized zirconia by tape-casting methods, J. Am. Ceram. Soc. 86 (2003) 395-400.

[29] J.-H. Lee, J.-W. Heo, D.-S. Lee, J. Kim, G.-H. Kim, H.-W. Lee, H. S. Song, H.-H. Moon, The impact of anode microstructure on the power generating characteristics of SOFC, Solid State Ionics 158 (2003) 225-232.

[30] A. Buyukaksoy, V. Petrovsky, F. Dogan, Stability and performance of solid oxide fuel cells with nanocomposite electrodes, J. Electrochem. Soc. 159 (2012) B666-B669.

[31] J. M. Vohs, R. J. Gorte, High-performance SOFC cathodes prepared by infiltration, Adv. Mater. 21 (2009) 943-956.

[32] T. J. Armstrong, J. G. Rich, Anode-supported solid oxide fuel cells with $La_{0.6}Sr_{0.4}CoO_3$–$Zr_{0.84}Y_{0.16}O_2$– composite cathodes fabricated by an infiltration method, J. Electrochem. Soc. 153 (2006) A515-A520.

[33] A. Sanson, P. Pinasco, E. Roncari, Influence of pore formers on slurry composition and microstructure of tape cast supporting anodes for SOFCs, J. Eu. Ceram. Soc. 28 (2008) 1221-1226.

[34] J. H. Choi, T. Lee, T.-S. Park, K.-B. Yoo, Y.-S. Yoo, Microstructure and Performance of Anode Supported Cell by Pore Size of Anode, in: J. Weidner and S. R. Narayanan (Eds.), ECS Transactions, Vol. 16, Battery and Energy Technology (General) – 214th ECS Meeting/PRIME 2008, The Electrochemical Society, Pennington, NJ, 2009, pp. 37-42.

[35] F. Tang, H. Fudouzi, T. Uchikoshi, Y. Sakka, Preparation of porous materials with controlled pore size and porosity, J. Eu. Ceram. Soc. 24 (2004) 341-344.

[36] C. Wang, T. Kasuga, M. Nogami, Macroporous calcium phosphate glass-ceramic prepared by two-step pressing technique and using sucrose as a pore former, J. Mater. Sci.: Mater. Med. 16 (2005) 739-744.

[37] A.-M. Le Raya, H. Gautier, J.-M. Bouler, P. Weiss, C. Merle, A new technological procedure using sucrose as porogen compound to manufacture porous biphasic calcium phosphate ceramics of appropriate micro- and macrostructure, Ceram. Int. 36 (2010) 93-101.

[38] Y. de Hazan, V. Märkl, J. Heinecke, C. Aneziris, T. Graule, Functional ceramic and nanocomposite fibers, cellular articles and microspheres via radiation curable colloidal dispersions, J. Eu. Ceram. Soc. 31 (2011) 2601-2611.

[39] H. Chen, K. Cheng, Z. Wang, W. Weng, G. Shen, P. Du, G. Han, Preparation of porous NiO-$Ce_{0.8}Sm_{0.2}O_{1.9}$ ceramics, J. Mater. Sci. Technol. 26 (2010) 523-528.

[40] T. Kim, G. Liu, M. Boaro, S.-I. Lee, J. M. Vohs, R. J. Gorte, O. H. Al-Madhi, B. O. Dabbousi, A study of carbon formation and prevention in hydrocarbon-fueled SOFC, J. Power Sources. 155 (2006) 231-238.

[41] E. Gregorová, W. Pabst, Porosity and pore size control in starch consolidation casting of oxide ceramics-achievements and problems, J. Eu. Ceram. Soc. 27 (2007) 669-672.

[42] E. Gregorová, W. Pabst, I. Bohačenko, Characterization of different starch types for their application in ceramic processing, J. Eu. Ceram. Soc. 26 (2006) 1301-1309.

[43] R. Barea, M. I. Osendi, P. Miranzo, J. M. F. Ferreira, Fabrication of highly porous mullite materials, J. Am. Ceram. Soc. 88 (2005) 777-779.

[44] T. Allen, Particle Size Measurement, Vols 1-2, 5th edition, Chapman & Hall, London, UK, 1997.

[45] R. Xu, Particle size characterization: light scattering methods, Kluwer Academic Publishers, Dordrecht, Netherlands, 2000.

[46] J. U. Keller, R. Staudt, Gas adsorption equilibria: experimental methods and adsorption isotherms, Springer, Berlin, Germany, 2005.

[47] X. Xu, R. Fu, J. M. F. Ferreira, Effect of homogenizing procedures on the slip casting of reaction sialon suspensions, Ceram. Int. 30 (2004) 745-749.

[48] X. Xu, S. Mei, J. M. F. Ferreira, Fabrication of Si_3N_4–SiC nano-composite ceramics through temperature-induced gelation and liquid phase sintering, J. Eu. Ceram. Soc. 3 (2006) 337-341.

[49] P. Beringer, Remington: the science and practice of pharmacy, 21st Ed., Lippincott Williams & Wilkins, Philadelphia, PA, USA, 2006.

[50] M. Asadi, Beet-sugar handbook, John Wiley & Sons, Inc., Hoboken, NJ, USA, 2007.

[51] N. Suppakarn, H. Ishida, J. D. Cawley, Roles of poly(propylene glycol) during solvent-based lamination of ceramic green tapes, J. Am. Ceram. Soc. 84 (2001) 289-294.

[52] X. Wei, A. Atkinson, Ceramic-metal interpenetrating network composites formed by electrodeposition, J. Electrochem. Soc. 152 (2005) C513-C519.

[53] R. E. Mistler, E. R. Twiname, Tape casting: theory and practice, The American Ceramic Society, Westerville, OH, USA, 2000.

[54] N. Straue, M. Rauscher, M. Dressler, A. Roosen, Tape casting of ITO green tapes for flexible electroluminescent lamp, J. Am. Ceram. Soc. 95 (2012) 684-689.

[55] S. Ding, S. Zhu, Y. Zeng, D. Jiang, Effect of Y_2O_3 addition on the properties of reaction-bonded porous SiC ceramics, Ceram. Int. 32 (2006) 461-466.

[56] H. Birol, T. Maeder, P. Ryser, Application of graphite-based sacrificial layers for fabrication of LTCC (low temperature co-fired ceramic) membranes and micro-channels, J. Micromech. Microeng., 17 (2007) 50-60.

Figures:

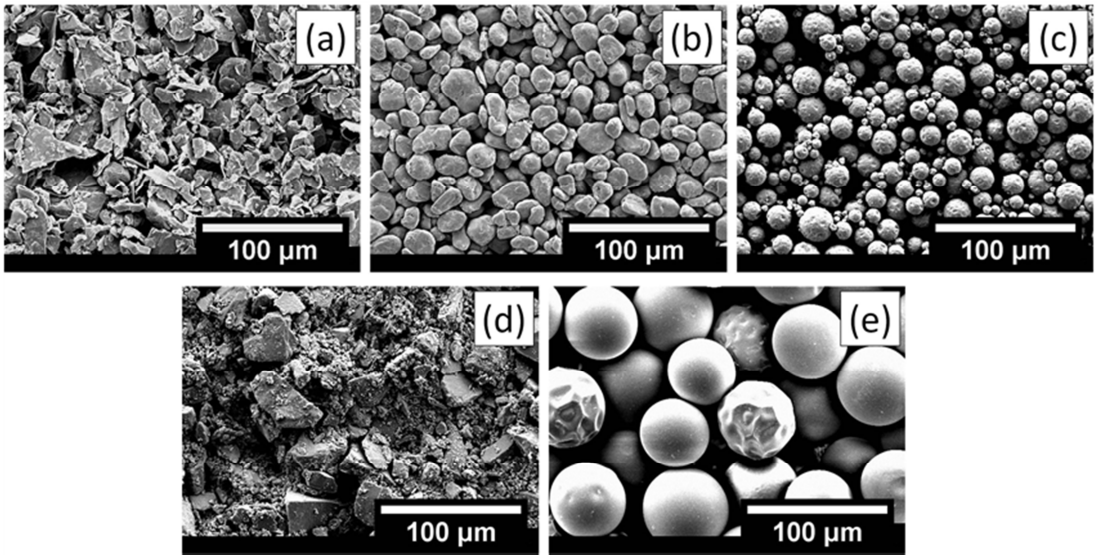

Figure 1. Scanning electron micrographs of (a) flake graphite, (b) spheroidal graphite, (c) PMMA, (d) sucrose and (e) polystyrene particles, respectively.

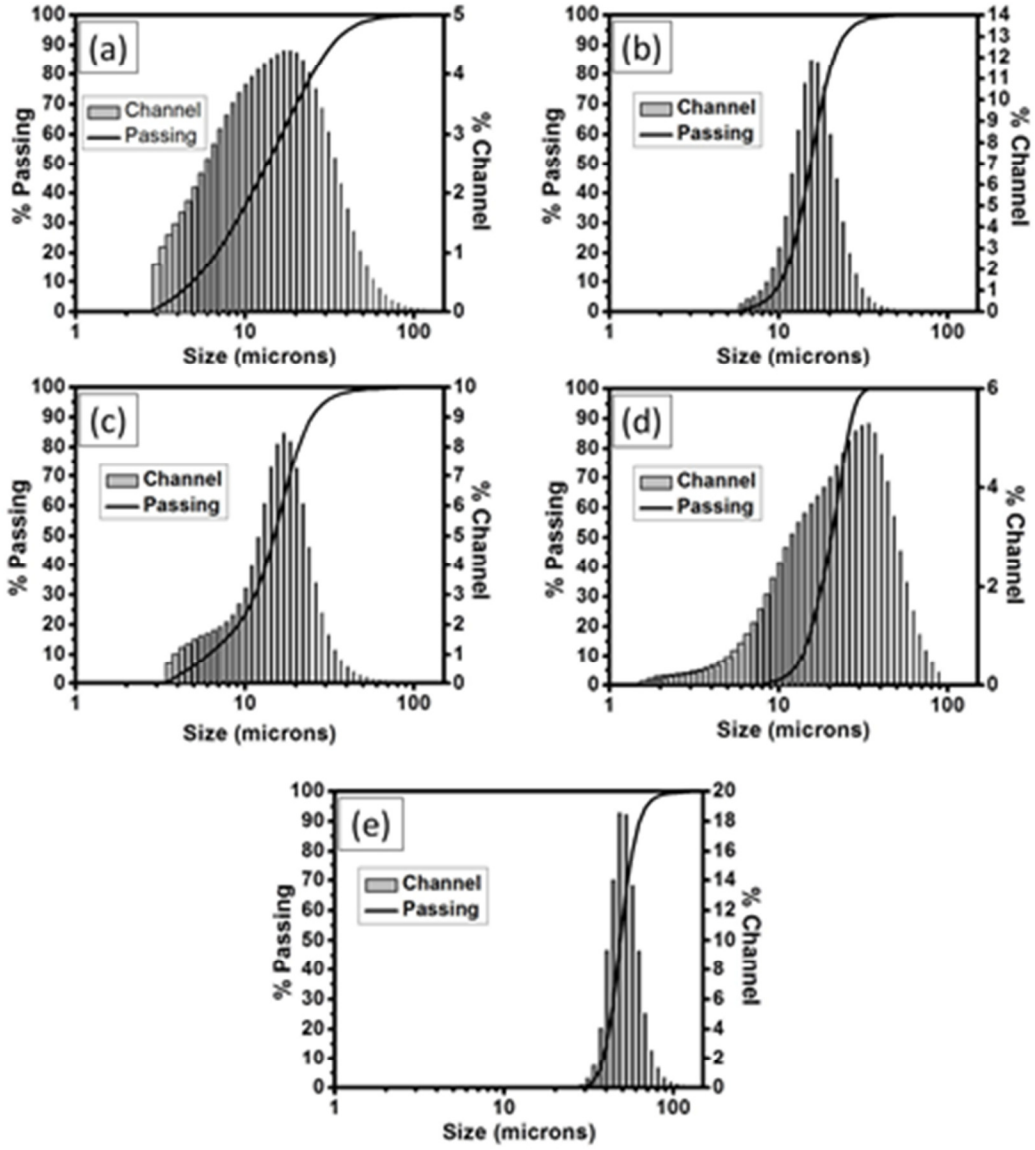

Figure 2. Number weighted particle size distributions of (a) flake graphite, (b) spheroidal graphite, (c) PMMA, (d) sucrose and (e) polystyrene particles, respectively.

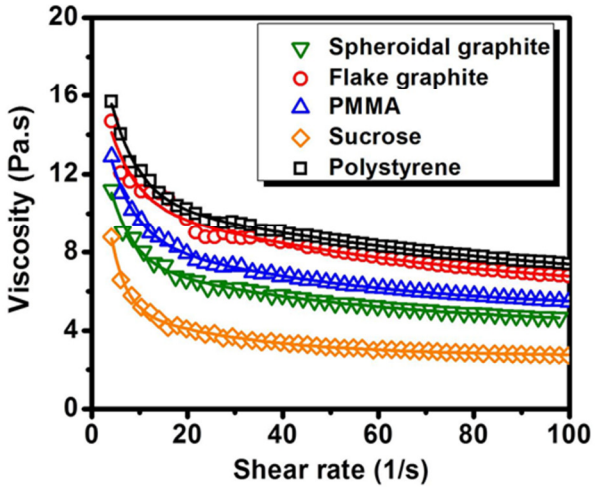

Figure 3. Viscosities of the tape casting slurries with various pore formers as a function of applied shear rate.

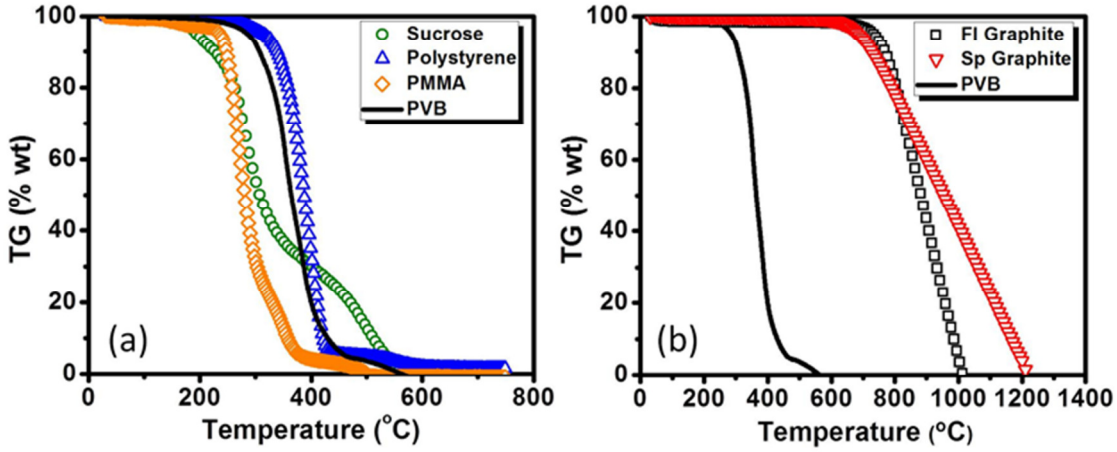

Figure 4. Thermogravimetric analysis of (a) the hydrocarbon based pore formers and (b) the graphite based pore formers with respect to the plasticized binder (PVB).

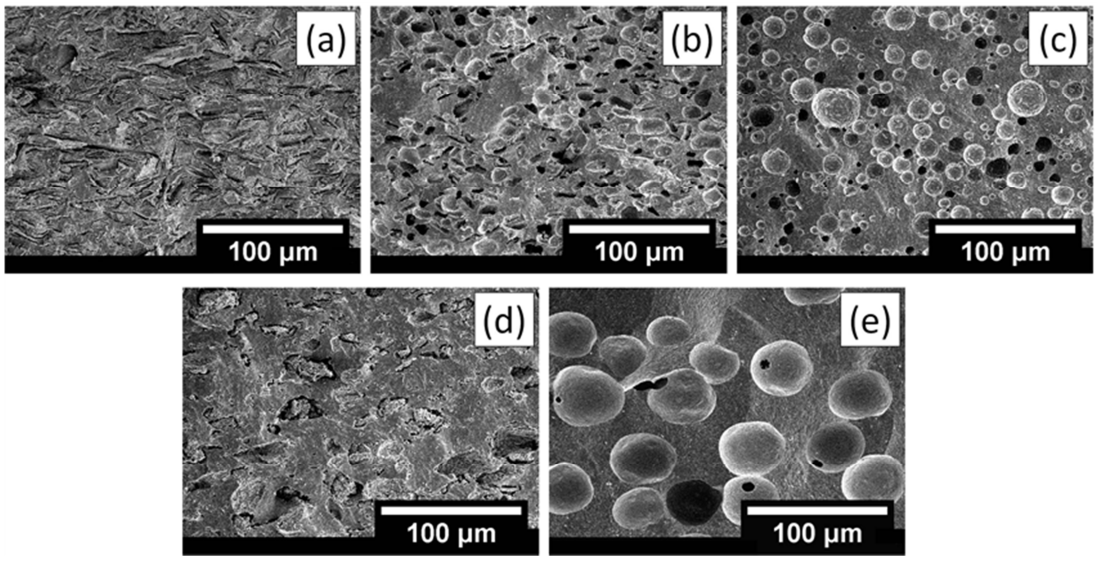

Figure 5. Scanning electron micrographs of the cross sections of the sintered porous YSZ samples prepared by removal of (a) flake graphite, (b) spheroidal graphite, (c) PMMA, (d) sucrose and (e) polystyrene pore formers, respectively.

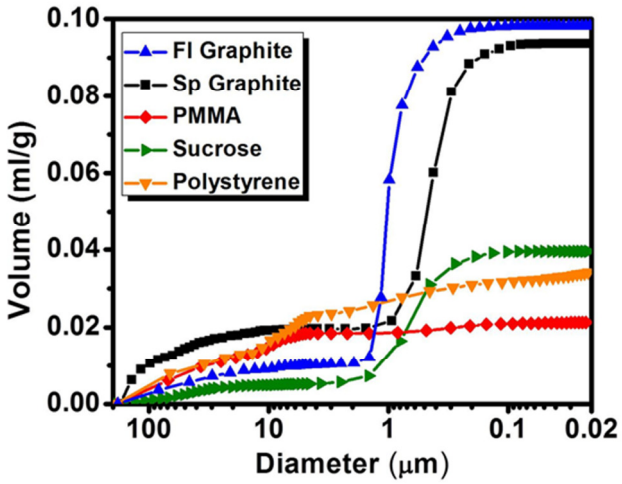

Figure 6. Pore size distribution of the sintered tapes characterized by the mercury intrusion porosimetry.

Tables:

Table 1. Particle size and surface area characteristics of the pore formers.

	Flake graphite	Spheroidal graphite	PMMA	Sucrose	Polystyrene
Mode (µm)	18.05	15.56	16.96	33.93	47.98
Median particle size (d_{50}) (µm)	13.57	15.42	14.93	22.64	48.40
Average particle size (µm)	6.59	13.09	8.39	4.14	46.37
Surface area (m^2/g)	4.526	5.45	1.168	0.771	0.106

Table 2. Compositions of the green tapes in weight and volume percents for various pore formers.

Pore former	YSZ		Dispersant		Binder		Plasticizer		Pore former	
Type	wt%	vol%	wt%	vol%	wt%	vol%	wt%	vol%	wt%	vol%
Flake graphite	61.7	28.6	0.3	0.7	11.5	29.5	5.8	15.9	20.7	25.3
Spheroidal graphite	61.7	28.6	0.3	0.7	11.5	29.5	5.8	15.9	20.7	25.3
PMMA	72.8	28.6	0.3	0.7	13.6	29.5	6.8	15.9	6.5	25.3
Sucrose	65.8	28.6	0.3	0.7	12.3	29.5	6.2	15.9	15.4	25.3
Polystyrene	69.4	28.6	0.3	0.7	13	29.5	6.5	15.9	10.8	25.3

Table 3. Decomposition/oxidation parameters of the pore formers and the plasticized binder (PVB).

Pore Former	Initial Decomposition Temperature	Onset Decomposition Temperature	Maximum Decomposition Temperature	Maximum Decomposition Rate	Final Decomposition Temperature
Type	(°C)	(°C)	(°C)	(g/min)	(°C)
Flake Graphite	618.93	758.34	863.79	3.982	1013.91
Spheroidal Graphite	599.68	690.77	1015.13	1.86	1198.68
PMMA	164.31	253.73	263.28	13.6	500.45
Sucrose	175.54	234.21	273.02	7.613	591.5
Polystyrene	249.33	352.82	385.71	13.1	598.32
PVB	212.51	316.48	349.5	10.81	589.54

Table 4. Dimensional changes and weight losses of the laminated dry tapes after removal of pyrolyzable components and firing at 800°C for one hour.

Tape	Volume Change	Diameter Change	Thickness Change	Weight Loss
Flake graphite	-4.19%	-2.14%	-0.05%	39.21%
Spheroidal graphite	-6.65%	-2.70%	-1.40%	39.19%
PMMA	-9.32%	-3.7%	-2.24%	28%
Sucrose	-17.49%	-6.29%	-6.05%	35.24%
Polystyrene	-9.54%	-5.67%	-1.65%	31.60%

Table 5. Dimensional changes and weight losses of the laminated dry tapes after sintering.

Tape	Volume Change	Diameter Change	Thickness Change	Weight Loss
Flake graphite	-56.59%	-24.46%	-23.93%	39.11%
Spheroidal graphite	-56.72%	-24.89%	-23.29%	39.21%
PMMA	-55.87%	-25.43%	-25.64%	28%
Sucrose	-64.14%	-29.21%	-28.43%	35.43%
Polystyrene	-57.51%	-27.14%	-19.93%	31.21%

Table 6. Measured bulk, open and closed porosities of the sintered tapes.

	Flake Graphite	Spheroidal Graphite	PMMA	Sucrose	Polystyrene
Bulk Porosity (%)	35.92	35.72	27.08	22.01	32.9
Open Porosity (%)	35.27	27.59	2.69	17.55	10.61
Closed Porosity (%)	0.65	8.13	24.38	4.46	22.29

V. DEVELOPMENT OF THE ANODE PORE STRUCTURE AND ITS EFFECTS ON THE PERFORMANCE OF SOLID OXIDE FUEL CELLS

Ayhan Sarikaya, Vladimir Petrovsky, Fatih Dogan

Department of Materials Science and Engineering,

Missouri University of Science and Technology, Rolla, Missouri 65409, USA

Abstract

Microstructural features, especially pore structure, has a substantial effect on the properties of the anode layer determining the electrochemical performance of the solid oxide fuel cells (SOFCs). Various anode pore structures were obtained by removal of different pyrolyzable pore formers (e.g. flake graphite, spheroidal graphite, spherical polymethyl methacrylate, random shaped sucrose, and spherical polystyrene particles). Determined processing parameters for the constituent layers allowed fabrication of Ni-YSZ anodes and complete multilayer fuel cells without macro defects (i.e. cracks, blisters and warpage). A systematic comparison was performed on the anode microstructures, as the fabricated fuel cells consisted of identical component layers (i.e. electrolyte, cathode and current collectors) supported by an anode layer with various pore structures. Voltammetric measurements and analyses of the corresponding impedance spectra on the developed fuel cells along with the investigations on the resultant microstructures using scanning electron microscopy and mercury intrusion porosimetry techniques led to the identification of the relationships between the anode pore structure and the electrochemical performance of the fuel cells. It was revealed that the anode pore structure has critical effects on the properties of the formed anode layers such as

electrical conductivity, gas permeability and electrochemical polarization. The novel findings on the anode pore structure allowed increasing the power density of the fuel cells with identical components from 0.45 W/cm^2 to power densities over 1.75 W/cm^2 at 800^{o}C using diluted hydrogen (10% H_2 in Ar) as fuel.

1. Introduction

Increasing energy demand of the technology based modern life urges researchers to seek for alternative energy sources. As the solid oxide fuel cells (SOFCs) demonstrated highest chemical to electrical energy conversion efficiencies (>55%), they have attracted significant attention. The total efficiency of the SOFCs exceeded 85% when combined with the generated heat [1, 2]. Therefore, significant effort has been focused on the research and development of the individual components as well the integration of the systems leading to the realization of the SOFC technology.

As the name implies, solid oxide fuel cells are based on solid oxide ceramic based electrolytes. The order of the electrochemical reactions, namely the reduction of the oxygen on the cathode side and the oxidation of the fuel (e.g. hydrogen) on the anode side, is completed by the transfer of the charged species (i.e. oxygen ions) through the electrolyte. The efficient transfer of the oxygen ions requires elevated temperatures to overcome the thermally activated energy barrier (activation energy) of the utilized electrolyte material. The most common type of the oxide based material used as electrolyte, yttria-stabilized zirconia (YSZ), limits the useful operation of the SOFCs at temperatures below 550^{o}C due to the drastic drop in its ionic conductivity.

The operation of the SOFCs at elevated temperatures gives rise to the kinetics of the electrochemical reactions as well as the ionic conductivity of the electrolytes; however, material related challenges, such as changes in the microstructural features and undesired interactions among the component materials, lead to degradation of their electrochemical performance. Therefore, the thickness of the electrolyte was reduced by employing various SOFC configurations in order to minimize the ohmic losses at useful operating temperatures ($\leq 800^{o}C$). SOFCs based on anode supported thin electrolytes gained importance and widely investigated as this particular fuel cell configuration demonstrated some of the highest performances up-to-date [3, 4].

Effects of the component microstructures on the performance of the SOFCs were widely investigated in order to improve the electrochemical performance of the fuel cells [5, 6]. It was revealed that microstructural properties of the components layers, especially the anode layer, have a critical effect on the electrochemical performance of the anode supported SOFCs [7-10]. It is essential that the anode layer satisfies the requirements below for substantial electrochemical performance [11-14].

(i) Percolation and homogeneous distribution of the constituent phases (YSZ, Ni and pores)

(ii) Substantial electronic and ionic conductivity

(iii) Adequate gas permeability for transport of fuel and product gases

(iv) Fine particles with high surface area for improved catalytic performance

Miscellaneous configurations were proposed to provide the required properties of an efficient anode and improve the electrochemical performance of the fuel cells such as

adding functional layers processed with fine particles between the electrolyte and the supporting anode [15, 16], grading of the microstructure by means of pore and grain sizes from fine to coarse starting from the anode-electrolyte interface [17, 18], and incorporating catalytically active particles (e.g. samaria-doped ceria) to the anode layer [19, 20]. Although significant improvements were achieved as a result of those efforts, fundamental issues arose due to the distinct properties of the component materials (dense electrolyte and porous anode layers). The difference in the sintering shrinkages and the thermal expansion of the anode functional layer compositions with fine particles and anode layer compositions with coarse particles along with the densifying electrolyte layer resulted in macro defects (e.g. delamination, warpage and cracks) upon sintering [21-23]. Moreover, the use of additional materials (i.e. gadolina-doped ceria) resulted in formation of undesired phases upon sintering at elevated temperatures [24, 25]. Even though these issues might be addressed by modifying the compositions and processing routes, each modification brings new challenges to the processing of the SOFCs and also increases the cost. Thus, it is essential that an anode layer is developed utilizing reliable and reproducible materials and employing cost-effective processing methods. Furthermore, use of a single porous anode layer interfacing with the dense electrolyte and the electrical contacts would simplify processing of the anode as well as the complete fuel cells. However, the relationships between the processing parameters, development of the microstructures and the resultant electrochemical performance of the anode layers need to be identified for successful fabrication and operation of SOFCs. Employing the commonly used Ni-YSZ anode compositions and using the conventional processing

routes would allow optimizing the anode microstructures in an efficient and cost-effective way.

Conventional fabrication route for the anode supported planar SOFCs is based on tape-casting and lamination of the anode and electrolyte tapes and their co-sintering. Co-sintering process requires elevated temperatures (i.e. 1300^{o}C-1500^{o}C) as the densification of the gas-tight electrolyte layer is achieved at this step [26, 27]. Cathode layers are screen-printed on the electrolyte layer supported by the anode. Since the relatively thin (5-50μm) cathode layers need to preserve their fine particles and high surface area while forming the structural integration of the constituent phases, their sintering temperatures are limited and do not reach the complete densification. Sintering temperatures range between 1100^{o}C-1200^{o}C for the most commonly used cathode composition based on YSZ and lanthanum-strontium manganite (LSM) [28].

Processing of the conventional SOFC based on LSM-YSZ cathode, YSZ electrolyte and Ni-YSZ anode is completed usually in-situ during measurements or operation by reducing the NiO component of the tape-cast, laminated and co-sintered NiO-YSZ to Ni. The reduction of NiO to Ni is accompanied by a volume change of ~40%. As the volume of the Ni based component decreases upon reduction, it forms porosity in the Ni-YSZ composite anode structure. Considering the useful NiO compositions, 40 vol% – 60 vol%, utilized in the processing of the anode layers, ~24 vol% could be the highest amount of porosity formed in the anode microstructure upon reduction. However, this amount is not sufficient for efficient transport of gases through the supporting thick anode layer [12]. Therefore, additional porosity is required for effective delivery of the fuel gases to the active reaction sites and the removal of the product gases.

Various methods have been utilized for the processing of porous ceramics. Considering the technical feasibility for processing of multilayer SOFC configurations, efficiency and affordable cost, partial sintering and incorporation of pyrolyzable pore formers to the component layers and their removal at elevated temperatures are the most commonly employed techniques. Sintering process is retarded in the partial sintering method to maintain the remaining porosity. Therefore, the features of the obtained pore structure such as pore size, shape and distribution cannot be controlled. Furthermore, partial sintering does not allow achieving the desired mechanical strength since the development of the microstructure is limited with the formation of neck between particles and does not complete a dense matrix [29, 30].

Incorporation of pyrolyzable pore formers into the ceramic compositions and their removal upon heating to elevated temperatures allow obtaining stable pores [31, 32]. Since the formed porosity remains after sintering at relatively high temperatures, desired pore structures can be achieved along with the mechanical properties. As the formed pore structure resembles the morphology of the pore former particles, wide variety of former particles with different size, shape and distribution provides further control for processing of the desired pore structures [5, 33]. Moreover, it allows the required simultaneous densification of the electrolyte layer due to high temperature processing. Thus, incorporation of the pore former particles into the anode compositions and their removal prior to their co-sintering with the electrolyte layers is one of the most commonly used routes for processing of the SOFCs.

Previous studies demonstrated that the incorporated pore formers have a critical effect on the developed anode microstructures [11, 32, 34]. Although various investigations were performed on effects of the pore formers on the sintered single anodes, further insight was required on the influence of the pore structure on the electrochemical performance of complete SOFCs. Furthermore, successful fabrication of dense thin electrolyte layers on the supporting anodes is required while modifying the anode pore structure for a thorough analysis of the anodes in complete fuel cell configurations. Previously, we reported that the performance of the SOFCs was improved tri-fold and power densities over 1.5 W/cm^2 were achieved by modifying the anode pore structure [34]. This study aims developing a further understanding of the relationships between the properties of the incorporated pore formers, features of the developed pore structures and the corresponding electrochemical parameters yielding the performance of the SOFCs. Therefore, five different pore formers with distinct properties (e.g. particle size, shape, distribution and thermal decomposition/oxidation) were employed for the investigations on the development of the anode pore structures. While identification of the processing parameters allowed successful fabrication of complete SOFCs with the investigated anode layers, the characterization of their electrochemical properties led to a novel understanding of the pore structure – electrochemical performance relationships in SOFCs.

2. Experimental

Investigations on the anode pore structures were performed both on single anode layers and complete SOFCs. Fabricated fuel cells consist of a tape-cast and laminated porous

Ni-YSZ anode, tape-cast YSZ electrolyte, screen-printed LSM-YSZ cathode and screen-printed LSM current collector layers. All of the employed fabrication methods were conventional and the utilized materials were commercially available.

Commonly used pore formers are usually in plate-like and spherical shape. In the previous study, flake graphite with plate-like particles and PMMA with spherical particles were utilized for the preparation of anode pore structures. Various pore formers with distinct properties were employed in this study to further analyze their effects on processing and performance of anode microstructures. Therefore, spheroidal graphite with nearly spherical particles, flake graphite with plate-like particles, PMMA with polydisperse spherical particles, sucrose with random particles and polystyrene with monodisperse spherical particles were investigated.

2.1. Fabrication

Employed conventional tape-casting and screen-printing techniques require preparation of ceramic slurries with the desired raw materials. Slurries for the electrolyte and anode layers were prepared using two and three-stage preparation methods. NiO (NiO-F, NexTech Materials, Columbus, OH, USA) and YSZ (8 mol% yttria stabilized zirconia, TZ-8Y, Tosoh, Tokyo, Japan) powders were mixed in a toluene/ethanol mixture using a dispersant (KD-1, ICI, Barcelona, Spain) to obtain a homogeneously dispersed slurry at the first stage. Addition of the NiO powder was excluded for the preparation of the electrolyte slurry. A binder configuration composed of PVB (PVB-79, Monsanto, St. Louis, MO, USA) and DOP (Dioctyl Phthalate, Sigma-Aldrich, St. Louis, MO, USA) was added to the slurries after mixing for 24 hours and the binder added slurries were

mixed for 24 hours to achieve a uniform mixture at the second stage. While the electrolyte tapes were required to yield dense and gas-tight layers after sintering, obtaining relatively porous (e.g. porosity over 50 %) layers were essential with the anode tapes [12]. Thus, the slurries of the anode tapes involved addition of the pore former particles. High purity flake (LBG2025, Superior Graphite, Chicago, IL, USA) and spheroidal graphite (SLA1518, Superior Graphite, Chicago, IL, USA), PMMA (2041, Sekisui, Osaka, Japan), sucrose (Alfa Aesar, Ward Hill, MA, USA) and polystyrene (Alfa Aesar, Ward Hill, MA, USA) were added to the NiO-YSZ slurries and mixed for 24 hours to complete the third stage. Since incorporation of each type of pore former results in a change in the rheological properties of the slurries, the compositions of the anode tapes were optimized for this study [35]. Identical volumetric loadings of the components were employed during the optimization of the anode tapes to prevent the pore forming effect of the additional binder [5]. The slurry compositions used for a reliable comparison with identical loadings are shown in Table 1.

Prepared ceramic slurries were degassed under vacuum prior to tape-casting. Casting was performed on a polyester film using a moving doctor blade setup. The tapes were dried at 25^{o}C in air and thicknesses around 14 µm and 100 µm were achieved with electrolyte and anode tapes, respectively. Anode tapes and an electrolyte tape were laminated using a pressure of 25 MPa at 80^{o}C. A thickness of 600±20 µm was measured with the prepared laminates. Pore former particles were removed from the anode layers in a controlled fashion to prevent formation of macro defects. Hence, the heating profiles determined in a previous study using identical pore formers for development of multilayer porous ceramics were employed [35]. The laminates with the anode layers

containing PMMA, sucrose and polystyrene pore formers were heated with a rate of 0.5^{o}C /min to the decomposition temperatures of 210^{o}C, 180^{o}C and 310^{o}C, respectively. They were held at the decomposition temperature for 1 hour prior to heating to the decomposition temperature (320^{o}C) of the binder (PVB). The laminates with the anode layers containing flake and spheroidal graphite heated to the decomposition temperature of the binder with a rate of 0.5^{o}C/min. As the binder decomposition was completed, the laminates were heated to the controlled oxidation temperature of the graphite based pore formers (600^{o}C) and held there for 2 hours to completely remove the pyrolyzable content. The sintering temperature and time were determined to obtain a gas-tight electrolyte layer and a porous NiO-YSZ anode. Thus, the minimum temperature and time was identified to densify the electrolyte layer while retarding the densification of the anode layer. As a consequence, all laminates were heated to the sintering temperature of 1350^{o}C and sintered for 2 hours.

Cathode and cathode current collector layers were applied on the sintered electrolyte layer supported by the porous anode layer by screen-printing the corresponding inks. The ink for the cathode layer was prepared by mixing LSM and YSZ powders with an organic vehicle (V-006, Heraeus, Conshohocken, PA, USA). Only LSM powder was mixed with the vehicle for the preparation of the cathode current collector layer. The composition of the cathode layer was 50 vol% LSM – 50 vol% YSZ and the cells were sintered at 1150^{o}C for 2 hours for the optimized performance as reported in a previous publication involving the optimization of the cathode layer [36].

2.2. Characterization

The analysis of the pore former particles and the porous anode microstructures developed upon their removal were performed using scanning electron microscopy techniques. Captured images were processed using an analysis software (ImageJ, NIST, Bethesda, MD, USA) for the characterization of the constituent anode phases. The dimensions of the anode layers before and after the removal of the pyrolyzable content and the sintering steps were measured for the identification of the dimensional changes. Further analysis of the porosity, pore size distribution and pore connectivity of the anode layers were conducted using a mercury intrusion porosimeter (PoreMaster 60, Quantachrome, Boynton Beach, FL, USA).

A combined potentiostat (CellTest 1470, Solartron, Mobrey, UK) and frequency response analyzer (1255B, Solartron, Mobrey, UK) setup was employed for the electrical and electrochemical analysis of the anode layers and the complete fuel cells. Electrical conductivity measurements of the anode layers were performed on 0.5 x 3.0 cm rectangular samples using a four-probe configuration. The voltammetric and impedance measurements of the fuel cells were carried out on samples around 2.7 cm in diameter with a cathode layer area of 0.3 cm^2. All measurements were performed at 800^oC by flowing diluted hydrogen on the anode side and air on the cathode side. Since consecutive fuel cells in stacks utilize hydrogen-poor fuel compositions, 10% hydrogen diluted in argon was used as the fuel to simulate realistic operating conditions.

3. Results and discussion

Analysis of the pore formers by SEM revealed that the PMMA and polystyrene particles were highly isometric as shown in Figure 1. While PMMA consisted of polydisperse particles, polystyrene particles were relatively monodisperse. Significantly anisometric particles were observed with flake graphite and sucrose particles as spheroidal graphite particles were rather isometric. Relatively polydisperse particles of flake graphite and sucrose exhibited wide particle size distributions as reported previously [35].

As it was expected, morphological features of the pore former particles were represented by the pore structure of the developed anode layers as shown in Figure 2. Relatively isometric particles of PMMA, polystyrene and spheroidal graphite particles resulted in the formation of nearly spherical pores. Significantly anisometric particles of flake graphite yielded pores resembling the shape of the initial particles and they were elongated in the tape casting direction. Since anode tapes were stacked by maintaining the horizontal layout of the tape-casting direction, the resultant pores are mainly perpendicular to the direction of gas flow from the bottom of the anode layer through the electrolyte interface. Therefore, the increased tortuous path formed by the elongated pores might not be preferable for efficient transport of gases through the supporting anode layer.

Although larger pores were expected to be formed, sucrose particles left fine pores relatively smaller than their initial size as shown in Figure 2(d). The thermal behavior of the sucrose upon heating resulted in the unexpected pore structure. As it was reported before, sucrose undergoes melting prior to its decomposition at elevated temperatures [35]. Hence, the liquid sucrose loses its initial morphology and increases the packing

density of the consolidated ceramic particles in a fashion similar to binder migration. As a result, expected larger pores disappear and a relatively fine pore structure develops upon its removal.

The analysis of the resultant microstructures indicated that the particle sizes of both Ni and YSZ phases were similar and around 0.5 µm. Considering the initial size of the YSZ (d_{50} = 25 nm) and NiO (d_{50} = 0.5 µm), it can be concluded that lowering the sintering temperature (1350^{o}C) and time (2h) retarded the grain growth of the particles and maintained the high surface area of the anode layers. No distinguishable difference was observed between the microstructures processed by removal of different pore former particles. It suggests that the formed pore structure does not have a significant influence on the particle sizes of the solid phases after sintering [34].

The analysis of the mercury intrusion porosimetry results demonstrated bimodal pore size distribution for all of the investigated anode layers. The majority of the intrusion (>80%) took place through pore channels with a diameter below 2 µm and 1 µm in the anode pore structures formed upon removal of graphite based and hydrocarbon based pore formers, respectively as shown in Figure 3. The intrusion through the pores above these diameters resembled the morphological features of the initial pore former particles. The anode prepared by removal polystyrene particles allowed the highest amount of intrusion through the pores between 110 µm – 1 µm while the anodes formed upon removal of flake graphite and sucrose particles led to the lowest amount of intrusion. As seen in the intrusion profiles, pore structures formed by the removal of flake graphite and sucrose particles consists of pores connected through relatively small openings and more than 90% of the intrusion took place through pore channels smaller than 2 µm. The

relatively anisometric plate-like particles of flake graphite were connected through their smaller dimension when elongated during tape casting. It resulted in the percolation of the particles and also connection of the pore channels through shorter, sub-micron dimensions as also observed in the scanning electron micrographs shown in Figure 2.

As sucrose particles melt before their removal, they formed a significantly fine pore structure which allowed connection of pores mainly through sub-micron channels. Relatively small pore connections were prone to closing upon sintering. Therefore, anode microstructures formed by removing flake graphite and sucrose demonstrated the highest amount of closed porosity as shown in Table 2. Graphite based pore former particles were removed at relatively higher temperatures (~600^{o}C) compared to the decomposition temperature of the binder (320^{o}C) and the other hydrocarbon based pore formers ($\leq$310^{o}C). Hence, the closing of the pores due to migration of the binder and the resulting increase of the packing of the ceramic powders were limited. Along with the expected easier percolation of particles with high aspect ratio, it allowed achieving the highest amount of bulk porosities as shown for flake graphite and spheroidal graphite. Removal of graphite based pore former particles at higher temperatures also allowed the smallest change in the dimensions of the corresponding anodes upon sintering as shown in Table 3. Melting of sucrose particles resulted in the largest change in the dimensions upon their removal and sintering.

While the investigated pore former could not be expected to form pores in submicron range, the reduction of NiO phase to Ni could produce fine porosity. As the volume of NiO particles decrease ~40% upon reduction, pores smaller than 0.2 µm in diameter are expected to be formed considering the initial size of the NiO particles (d_{50} = 0.5 µm) and

the final particle size of the sintered and reduced Ni phase (d_{50} = 0.5 µm) in the porous anode microstructures. Although a relatively high pressure (>200 MPa) was applied for the intrusion of Hg, no pores were observed smaller than 0.2 µm in diameter in the anode layer formed by removal of flake graphite. The intrusion of Hg took place at pore diameters down to 0.01 µm in the pore structures formed by removal of other pore former particles. The continuous intrusion through relatively small pore channels suggests the percolation of the pores accessing the high surface area of the solid anode phases and the active reaction sites. However, in the case of the anode pore structure formed by removal of flake graphite suggests that the available surface area of the anode microstructure and the reaction sites could not be utilized due to the interrupted percolation of the pores and limited intrusion through fine pores formed upon reduction.

Properties of the anode layer such as (i) composition, (ii) pore structure, (iii) size of the constituent particles and (iv) percolation of the electrically conductive phase (i.e. Ni) determine its electrical conductivity [13, 15, 34]. Thus, four-probe electrical conductivity measurements were performed on individual anode layers with different pore structures and a significant difference between their conductivities was observed as shown in Table 3. The lowest electrical conductivity (157 S/cm) was measured with the anode layer formed by removal of flake graphite particles as a relatively higher electrical conductivity (1137 S/cm) was measured with the anode layer fabricated upon burn-out of the PMMA particles. The high aspect ratio of the flake graphite particles and their preferential orientation along the tape casting direction did not only disturb the percolation of the pores, but also interrupted the percolation of the Ni phase and gave rise to its electrical resistance. The uniformly distributed isometric pores of the anodes prepared by removal

of PMMA and polystyrene particles allowed a continuous percolation of the pores while maintaining the percolation of the Ni phase. Although similar bulk and open porosities were formed with both types of anode pore structures, the change in the thickness of the pore walls also had a distinguishable effect in the resultant electrical conductivity of the anode layers. Hence, a higher electrical conductivity of 1335 S/cm was measured due to the higher pore wall thickness of the structure formed by removal of polystyrene particles as shown in Figure 2. As the anode layer processed by removal of flake graphite yielded a relatively low electrical conductivity, it might not be desirable for a successful current collection minimizing the ohmic losses on the SOFCs.

As the fabrication of the fuel cells was based on the lamination of the electrolyte layer and the anode layers and their co-sintering, the integration of the component layers was crucial for their processing without macro defects. A relatively thin (~10 μm) electrolyte layer was applied on a significantly thick (~500 μm) porous anode layer. In case the electrolyte layer is exposed to tensile stresses due to the smaller changes in the diameter of the anode layer during sintering, it would cause warpage of the multilayer structure as shown in Figure 4(a) and ultimately form cracks on the electrolyte layer. Thus, the most critical dimensional change among the different dimensions shown in Table 4 was the diameter change. An electrolyte tape was prepared considering the minimum diameter change observed with the investigated anode layers to maintain compressive stresses on the electrolyte during sintering. Investigations on the samples of the electrolyte tape in the diameter of the button cells demonstrated that the change in its diameter was around -20%. The removal of the pyrolyzable content and the sintering of the laminated tapes were carried out while maintaining their linear planar shape elongated between flat YSZ

based setter plates. The electrolyte layer was exposed only to compressive stresses during fabrication due to the applied relatively small confining pressure (~0.002 MPa). As a consequence, crack-free and flat anode supported electrolyte half-cells were obtained with all of the investigated anode compositions using identical electrolyte layers for a reliable comparison as shown in Figure 4.

Figure 5 shows a typical cross-section of the investigated anode supported fuel cells after reduction of the NiO-YSZ anode layer to Ni-YSZ. A similar thickness of ~10 µm was achieved with crack-free electrolyte, porous cathode and cathode current collector layers. The microstructures and thicknesses of these layers were maintained for all of the fuel cells fabricated for this study.

The results of the voltammetric measurements on the processed SOFCs are shown in Figure 6. All of the fuel cells demonstrated an open circuit voltage (OCV) over 1 V as expected considering the fuel composition and the operating temperature [34]. It confirmed the leak-free electrolyte layers and the reliable sealing of the measurement fixture. The current density – voltage dependence of all fuel cells except the fuel cell with the anode layer prepared upon removal of flake graphite demonstrated a similar slope and a deviation from linearity at high current densities. As the fuel cell operates at higher current densities, its operation requires delivery of a larger amount of fuel to the anode reaction interface and removal of the product gases. Even though the cell fabricated with the anode formed upon removal of flake graphite would exhibit a similar limitation, its performance and the corresponding current density was limited. While the lowest peak power density of 0.45 W/cm^2 was obtained with that anode configuration, the fuel cells with the anodes prepared by removing spheroidal graphite and PMMA particles

demonstrated the highest peak power density of 1.54 W/cm^2 at 800^{o}C. The fuel cells with the anode pore structures formed by removing spheroidal graphite and PMMA particles also exhibited power densities of 1.31 W/cm^2 and 1.29 W/cm^2 at 0.7 V, respectively.

Current density – voltage profiles of the investigated fuel cells demonstrated that the peak power densities were achieved around the potential of 0.5 V. Thus, the impedance spectroscopy measurements were mainly focused on that regime to reveal the performance limiting parameters. An equivalent circuit model was determined to characterize the measured impedance spectra. The model consists of a resistor and two constant phase elements in series as shown in Figure 7(a). The total magnitude of the resistances induced by the corresponding high frequency processes are represented by the high frequency x-axis intercept of the Cole-Cole plots (Figure 7) [18]. It is the total ohmic polarization resistance (R1 in the equivalent circuit model) and resembles the sum of the electrical resistances of the electrolyte, electrode and current collector layers of the fuel cells at the measurement temperature utilized for this study (i.e. 800^{o}C). It was observed that the fuel cells with the anode layers fabricated by removal of flake graphite and PMMA demonstrated significantly different ohmic resistances of 0.085 Ohm cm^2 and 0.043 Ohm cm^2, respectively as shown in Table 5. Since all other contributions to the measured ohmic resistance of the cells could not vary due to the identical layers and similar results were reproduced with multiple cells, the possible effect of the difference in the anode pore structures to the electrical resistances was investigated [34]. The measured electrical conductivity of the anode layers (Table 3) were compared with the yielded ohmic resistances deconvoluted from the impedance spectra (Table 5) and a strong correlation was observed. The interrupted percolation of the anode layer fabricated by

removal of flake graphite particles did not allow reaching the required conductivity for an efficient anode layer (>1000 S/cm). On the other hand, the uniform pore structures of the other investigated anode layers allowed the percolation of the Ni phase and led to significantly high electrical conductivities while reducing the contribution of the anode layer to the ohmic resistance of the fuel cells. The lowest total ohmic resistance of 0.041 Ohm cm^2 was achieved with the fuel cell utilizing the most conductive (1335 Ohm cm^2) anode layer (formed upon removal of polystyrene) investigated in this study. It confirmed the effect of the pore structure on the percolation of the Ni phase and the resulting changes in its electrical conductivity.

Two different dominating processes with distinguishable characteristic relaxation frequencies were observed in the impedance spectra of the investigated fuel cells. Their characterization by deconvolution of the impedance spectra using the equivalent circuit model indicated that the previously developed cathode layer utilized for the fabrication of the fuel cells did not induce any performance limitations [36, 37]. Both low and high frequency arcs arose due to the processes involving the anode layer. Investigations showed that the high frequency arc with the characteristic frequency range of 10^3-10^4 correspond to the anode activation processes and it is in a good agreement with the previous studies on SOFCs with similar configurations [38-40]. The highest anode activation polarization resistance (0.169 Ohm cm^2) was measured with the SOFC utilizing the anode layered prepared by removal of flake graphite as shown in Table 5. The fuel cell with the anode layer prepared by removing spheroidal graphite particles exhibited a relatively lower anode activation polarization resistance of (0.075 Ohm cm^2). Similar characteristic frequencies (Figure 7) and the particle sizes (Figure 2) suggest a

similar nature for the reaction sites yielding the anode activation processes. However, there was a strong increase in the magnitude of the polarization resistance due to the interrupted percolation of the phases (i.e. closed pores and non-percolated Ni phase). As the anode layer prepared by removal of spheroidal graphite provided the required percolation of the all three phases, all active reaction sites were accessible and they gave rise to the electrochemical activity by decreasing the magnitude of the polarization resistance along with the increasing electrical conductivity [41].

As the diluted hydrogen (10% H_2 in Ar) was supplied to the anode side as a fuel, its flow through the anode layer and delivery to the active reaction sites was provided by the pore structure of the anode layer. The required improved delivery of the fuel gas for operation of the fuel cells at high power outputs might not be satisfied due to the tortuous path or closed pore structure of the anode layer. The analyses on the measured impedance spectra of the fuel cells demonstrated that the low frequency arc (~10 Hz) was associated with the retarded gas transport through the anode layer [36, 41]. Although the fuel cell with the anode layer prepared by removal of flake graphite particles exhibited the lowest power density and also the current density among the investigated SOFCs, its performance was limited mainly by the concentration polarization (0.288 Ohm cm^2). The horizontal orientation of the pores perpendicular to the direction of the gas flow resulted in a relatively tortuous pathway. Moreover, the interrupted percolation of the pores due to the closed porosity gave rise to the corresponding polarization resistance. A similar problem was observed also with the anode layer fabricated by removal of sucrose particles. As the particles of sucrose melted, they resulted in a significant amount of closed porosity along with a very fine pore structure. Thus, the percolation of the pores

was interrupted and their connection was established through a relatively tortuous path. As a result, a concentration polarization resistance more than six times higher than its activation polarization resistance was measured as shown in Table 5.

The highest polarization resistance due to transport of gases was measured with the anode layer formed upon removal of polystyrene particles. Although polystyrene particles left the largest pores among the investigated pore formers, the connection of the large pores was provided through relatively small pore channels (Figure 2). The connection through smaller pores was also confirmed by the shift through the smaller pore sizes for the intrusion of mercury as shown in Figure 3. Hence, a significantly high concentration polarization resistance of 0.5 Ohm cm^2 was measured with the fuel cell operating near the peak power density at 0.5 V.

According to the interpretation of the impedance spectra, the dominating low frequency process (i.e. concentration polarization) was expected to be minimized or eliminated by decreasing the length of the gas delivery/removal path through the anode. Therefore, the thickness of the anodes was lowered from ~500 µm to ~300 µm by using the identical components (electrolyte, cathode and current collector layers). Since the thickness of the anode layer was decreased, the electrical resistance of the thinner anode could add to the ohmic resistance of the cells. Hence, the anode layer with the highest electrical conductivity (i.e. anode layer formed upon removal of polystyrene particles) was selected to reduce its thickness for minimum increase in the ohmic resistance for the sake of a systematic comparison. Moreover, the highest concentration polarization of the selected anode layer could demonstrate a more pronounced decrease due to the change in the gas delivery path.

The impedance spectra of the fuel cells with the anode layers formed by removing the polystyrene particles demonstrated that the concentration polarization resistance eliminated by reducing its thickness to 300 µm as shown in Figure 8. The analysis of the polarization mechanism corresponding to the low frequency arc demonstrated that it was induced by the cathode surface processes as reported previously [36]. Although there was a slight increase in the ohmic resistance of the cell from 0.041 Ohm cm^2 to 0.055 Ohm cm^2 due to thinner anode layer, it could be considered negligible. The significantly decreased total resistance of the fuel cell (from 0.611 Ohm cm^2 to 0.117 Ohm cm^2) allowed minimizing the deviation from the linear current density – voltage trend and yielded a power density of 1.76 W/cm^2 at 800^oC in the same operating conditions as shown in Figure 9. The eliminated concentration polarization of the anode layer by reducing its thickness confirmed the pursued approach and the interpretation of the deconvoluted polarization resistances from the measured impedance spectra.

4. Summary and conclusions

Determined processing parameters (e.g. compositions, dimensions and heating profiles for removal of the pyrolyzable content and sintering) allowed successful fabrication of anode layers with distinct pore structures using various pore former particles with different properties. Anode supported thin electrolyte layers were obtained without macro defects and utilized as half-cells upon co-sintering. Previously developed cathode layers were applied on the sintered electrolyte layer at a subsequent step. As the dimensional changes upon sintering were controlled by the processing parameters, a composition was selected where all pore formers could be employed for forming anode microstructures

with distinct pore structures while co-sintering with a thin electrolyte layer. Obtained SOFCs had identical components and dimensions while varying only the anode pore structure. It allowed a reliable comparison between the development of the anode layers with different pore structures and their effects on the electrical and electrochemical properties of the fuel cells.

Analysis of the developed anode layers demonstrated that the morphological features (e.g. particle size and shape) are resembled by the formed pore structures. It allowed forming desired pore structures by utilizing selected pore former particles. Only sucrose did not yield predictable pore structures due to melting of its particles prior to their removal. While sucrose formed relatively small pores after melting of its large particles, flake graphite formed pore channels with comparable dimensions due their high aspect ratio. As the fine pore channels were more prone to collapsing upon sintering, both pore structures led to formation of closed porosity. The other pore formers (spheroidal graphite, PMMA and polystyrene) with more isometric and uniform particles (aspect ratio ~1) resulted in anode microstructures with uniform and completely open porosity.

The uniform and continuous distribution of the pores allowed the successful percolation of the other constituent phases. Therefore, the electrical conductivity of the anode layers with the identical composition demonstrated an eight-fold increase when the pore structure was changed from the non-uniform elongated plate-like pores left by flake graphite to uniform spherical pores formed upon removal of polystyrene particles.

Electrochemical analysis of the developed fuel cells allowed revealing the correlations between the anode pore structures and the performance limiting parameters. The improved percolation of the phases also gave rise to electrochemical performance of

the anode layers. As a conclusion of the impedance analyses, it was found out that the uniformly distributed pores and percolation of the constituent phases minimize the sluggish anode activation processes by utilizing the active reaction sites while the large pores provide the main pathway for the gas transport. As the current density drawn from the fuel cells increase with the increasing power densities, the pore channels were not sufficient to provide the required gas transport due to their tortuous path even if the pores are completely open and percolated. Thus, the pore structure formed by removal of polystyrene particles was investigated by changing its thickness in the identical SOFC configuration. As a result, the concentration polarization resistance was eliminated by reducing the pathway for the gas delivery and removal. It allowed increasing the peak power density of the fuel cells to substantial power densities over 1.75 W/cm^2 from 1.25 W/cm^2 and confirmed the applied impedance and voltammetric characterization approach for characterization of the performance limiting polarization mechanisms and development of efficient anode pore structures.

Acknowledgements

This work was supported by a grant of the AFRL under contract no. FA4819-09-C-0018. Utilization of SEM facilities at the Graduate Center for Materials Research (MRC) of Missouri S&T is greatly acknowledged.

References

[1] Riensche E, Achenbach E, Froning D, Haines MR, Heidug WK, Lokurlu A et al. Clean combined cycle SOFC power plant - cell modelling and process analysis. J Power Sources;86 (1–2) (2000): 404–410.

[2] Santin M, Traverso A, Magistri L, Massardo AF. Thermoeconomic analysis of SOFC–GT hybrid systems fed by liquid fuels, Energy;35 (2010):1077–1083.

[3] Minh NQ. Solid oxide fuel cell technology-features and applications. Solid State Ionics 2004;174(1-4):271-277.

[4] Yakabe H, Hishinuma M, Uratani M, Matsuzaki Y, Yasuda I. Evaluation and modeling of performance of anode-supported solid oxide fuel cell. J Power Sources 2000;86(1-2):423-431.

[5] Boaro M, Vohs JM, Gorte RJ. Synthesis of highly porous yttria-stabilized zirconia by tape-casting methods. J Am Ceram Soc 2004;86(3):395-400.

[6] Wilson JR, Barnett SA, Electrochem Solid-State Lett 2008;11(10):B181–B185.

[7] Minh NQ. Ceramic fuel cells. J Am Ceram Soc 1993;76(3):563–88.

[8] Jiang S-P, Callus PJ, Badwal SPS. Fabrication and performance of Ni/3 mol% Y_2O_3–ZrO_2 cermet anodes for solid oxide fuel cells. Solid State Ionics 2000;132(1-2):1-14.

[9] Lee C-H, Lee C-H, Lee H-Y, Oh S-M. Microstructure and anodic properties of Ni/YSZ cermets in solid oxide fuel cells. Solid State Ionics 1997;98(1-2):39–48.

[10] Brown M, Primdahl S, Mogensen M. Structure/performance relations for Ni/yttria-stabilized zirconia anodes for solid oxide fuel cells. J Electrochem Soc 2000;147(2):475–485.

[11] Clemmer RMC, Corbin SF. Influence of porous composite microstructure on the processing and properties of solid oxide fuel cell anodes. Solid State Ionics 2004;166(3-4):251-259.

[12] Holzer L, Münch B, Iwanschitz B, Cantoni M, Hocker Th, Graule Th. Quantitative relationships between composition, particle size, triple phase boundary length and surface area in nickel-cermet anodes for solid oxide fuel cells. J Power Sources 2011;196(17):7076-7089.

[13] Atkinson A, Barnett S, Gorte RJ, Irvine JT, McEvoy AJ, Mogensen M, et al. Advanced anodes for high-temperature fuel cells. Nat Mater 2004;3(1):17-27.

[14] Simwonis D, Thülen H, Dias FJ, Naoumidis A, Stöver D. Properties of Ni/YSZ porous cermets for SOFC anode substrates prepared by tape casting and coat-mix® process. J Mater Process Technol 1999;92-93(1):107-111.

[15] Virkar AV, Chen J, Tanner CW, Kim J-W. The role of electrode microstructure on activation and concentration polarizations in solid oxide fuel cells. Solid State Ionics 2000;131(1-2):189-198.

[16] Vivet N, Chupin S, Estrade E, Piquero T, Pommier PL, Rochais D, et al. 3D microstructural characterization of a solid oxide fuel cell anode reconstructed by focused ion beam tomography. J Power Sources 2011;196(18):7541-7549.

[17] Han MF, Yin H-Y, Miao W-T, Zhou S. Fabrication and properties of anode-supported solid oxide fuel cell. Solid State Ionics 2008;179(27-32):1545-1548.

[18] Wang Z, Zhang N, Qiao J, Sun K, Xu P. Improved SOFC performance with continuously graded anode functional layer. Electrochem Commun 2009;11(6):1120-1123.

[19] Ai N, Lü Z, Chen K, Huang X, Du X, Su W. Effects of anode surface modification on the performance of low temperature SOFCs. J Power Sources 2008;171(2):489-494.

[20] Ai N, Lü Z, Tang J, Chen K, Huang X, Su W. Improvement of output performance of solid oxide fuel cell by optimizing Ni/samaria-doped ceria anode functional layer. J Power Sources 2008;185(1):153-158.

[21] Li W, Hasinska K, Seabaugh M, Swartz S, Lannutti J. Curvature in solid oxide fuel cells. J Power Sources 2004;138(1-2):145-155.

[22] Malzbender J, Steinbrech RW. Advanced measurement techniques to characterize thermo-mechanical aspects of solid oxide fuel cells. J Power Sources 2007;173(1):60-67.

[23] Mücke R, Menzler NH, Buchkremer HP, Stöver D. Cofiring of thin zirconia films during SOFC manufacturing. J Am Ceram Soc 2008;92(s1):S95-S102.

[24] Tsoga A, Naoumidis A, Stöver D. Total electrical conductivity and defect structure of ZrO_2–CeO_2–Y_2O_3–Gd_2O_3 solid solutions. Solid State Ionics 2000;135(1-4):403-409.

[25] Zhou XD, Scarfino B, Anderson HU. Electrical conductivity and stability of Gd-doped ceria/Y-doped zirconia ceramics and thin films. Solid State Ionics 2004;175(1-4):19-22.

[26] Basu RN, Blass G, Buchkremer HP, Stover D, Tietz F, Wessel E, Vinke I. Simplified processing of anode-supported thin film planer solid oxide fuel cells. J Eur Ceramic Soc 2005;25(4):463-471.

[27] Bao W, Chang Q, Meng G. Effect of NiO/YSZ compositions on the co-sintering process of anode-supported fuel cell. J Membrane Sci 2005;259(1-2):103-109.

[28] Jorgensen MJ, Primdahl S, Bagger C, Mogensen M. Effect of sintering temperature on microstructure and performance of LSM–YSZ composite cathodes. Solid State Ionics 2001;139(1-2):1-11.

[29] Zhang HL, Li J-F, Zhang B-P. Microstructure and electrical properties of porous PZT ceramics derived from different pore-forming agents. Acta Mater 2007;55(1):171-181.

[30] Corbin SF, Apté PS. Engineered porosity via tape casting, lamination and the percolation of pyrolyzable particulates. J Am Ceram Soc 1999;82(7):1693-1701.

[31] Corbin SF, Lee J, Qiao X. Influence of green formulation and pyrolyzable particulates on the porous microstructure and sintering characteristics of tape cast ceramics. J Am Ceram Soc 2001;84(1):41-47.

[32] Sanson A, Pinasco P, Roncari E. Influence of pore formers on slurry composition and microstructure of tape cast supporting anodes for SOFCs. J Eur Ceramic Soc 2008;28(6):1221-1226.

[33] Lee JH, Heo JW, Lee DS, Kim J, Kim GH, Lee HW, et al. The impact of anode microstructure on the power generating characteristics of SOFC. Solid State Ionics 2003;158(3-4):225-232.

[34] Sarikaya A, Petrovsky V, Dogan F. Effect of the anode microstructure on the enhanced performance of solid oxide fuel cells. Int J Hydrogen Energy 2012;37(15):11370-11377.

[35] Sarikaya A, Dogan F. Effect of various pore formers on the microstructural development of tape-cast porous ceramics. Ceram Int 2013;39(1):403-413.

[36] Sarikaya A, Petrovsky V, Dogan F. Influence of microstructural evolution on the electrochemical performance of LSM-YSZ composite cathodes for high performance solid oxide fuel cells. J Electroceram (*submitted*).

[37] Sarikaya A, Petrovsky V, Dogan F. Effect of microstructural evolution on the electrochemical properties of high performance SOFCs. In: Mogensen M, Armstrong T, Gur T, Yokokawa H, Zhou X, editors. ECS Transactions, Vol. 45, The Electrochemical Society, Pennington, 2012, pp. 25-32.

[38] Primdahl S, Mogensen M. Oxidation of hydrogen on Ni/yttria-stabilized zirconia cermet anodes. J Electrochem Soc 1997;144(10):3409-3419.

[39] Barfod R, Hagen A, Ramousse S, Hendriksen PV, Mogensen M. Break down of losses in thin electrolyte SOFCs. Fuel Cells 2006;6(2):141-145.

[40] Primdahl S, Mogensen M. Gas diffusion impedance in characterization of solid oxide fuel cell anodes. J Electrochem Soc 1999;146(8):2827-2833.

[41] Lee J-J, Moon H, Park H-G, Yoon D-I, Hyun S-H. Applications of nano-composite materials for improving the performance of anode-supported electrolytes of SOFCs. Int J Hydrogen Energy 2010;35(2):738-744.

Figures:

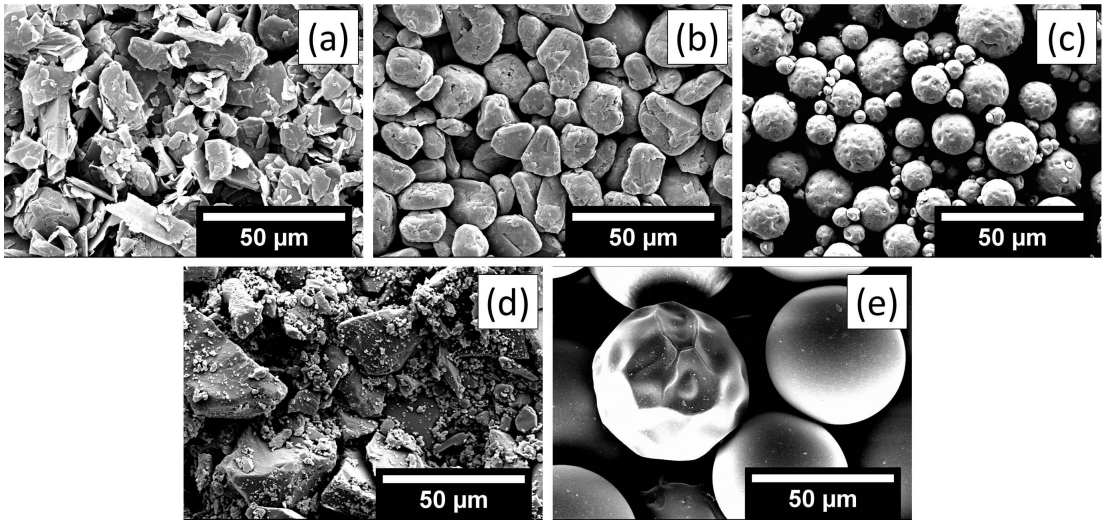

Figure 1. Scanning electron micrographs of flake graphite (a), spheroidal graphite (b), PMMA (c), sucrose (d) and polystyrene (e) pore former particles.

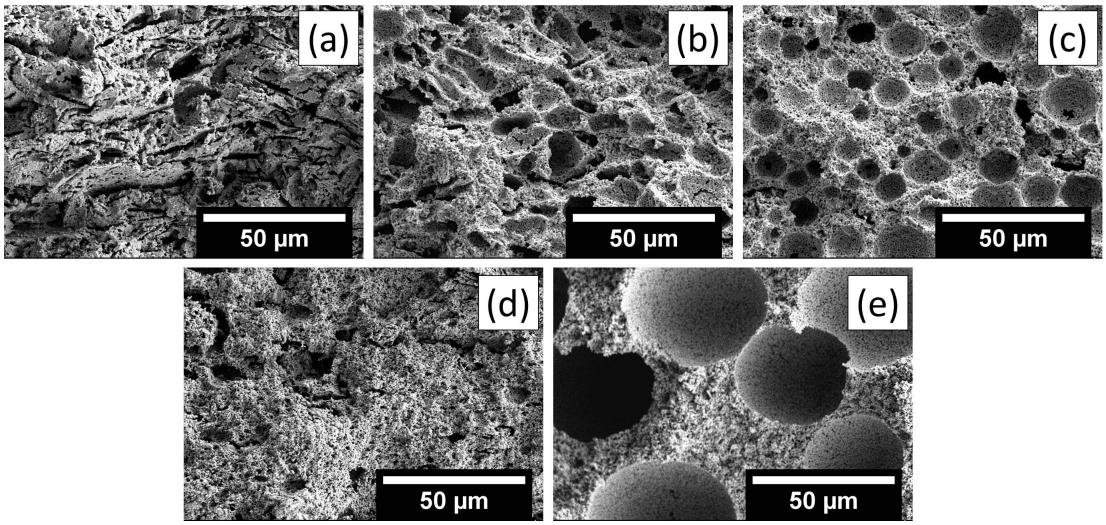

Figure 2. Scanning electron micrographs of the cross sectional fracture surface of the sintered and reduced Ni-YSZ anodes processed by removal of flake graphite (a), spheroidal graphite (b), PMMA (c), sucrose (d) and polystyrene (e) pore former particles.

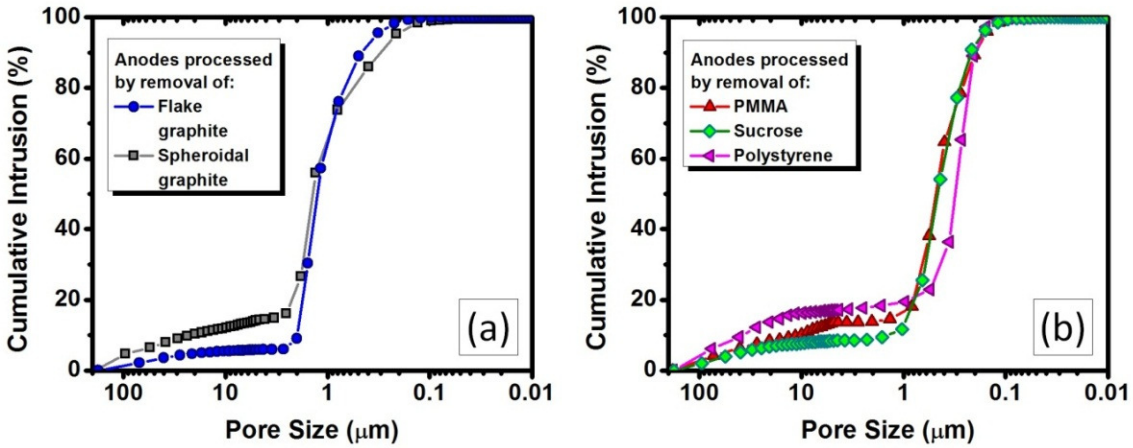

Figure 3. Cumulative intruded volume of Hg as a function of pore size in sintered and reduced Ni-YSZ anodes processed by removal of various pore formers.

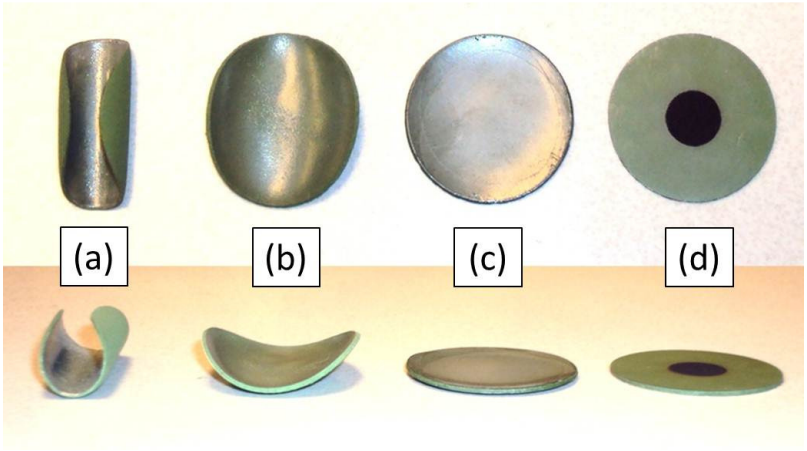

Figure 4. Top and side views of the co-sintered anode supported thin electrolyte cells with reduced warpage by decreasing the electrolyte sintering shrinkage (a to c) and the fabricated planar fuel cell with no macro defects (d).

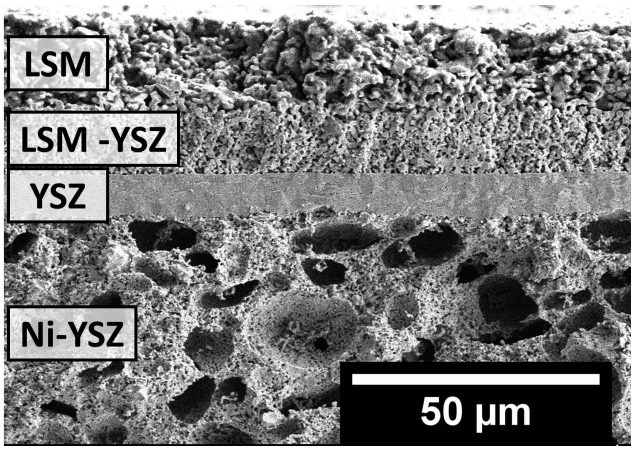

Figure 5. Scanning electron micrograph of a typical cross-sectional fracture surface of a developed anode supported planar SOFC. Note that the shown porous anode layer was processed by removal of spheroidal graphite particles.

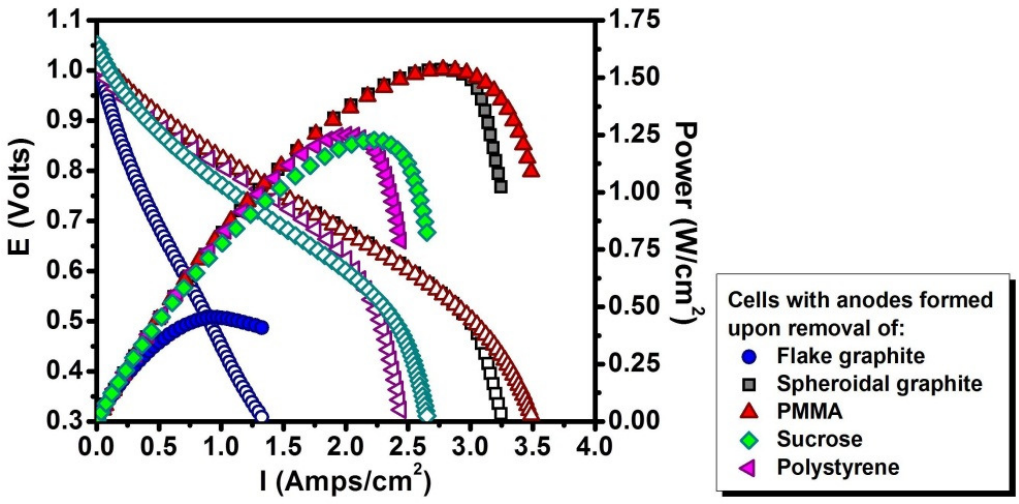

Figure 6. Measured current density - voltage curves and the associated power densities of the fuel cells with the anodes processed by removal of various pore formers. All measurements were performed at 800^{o}C.

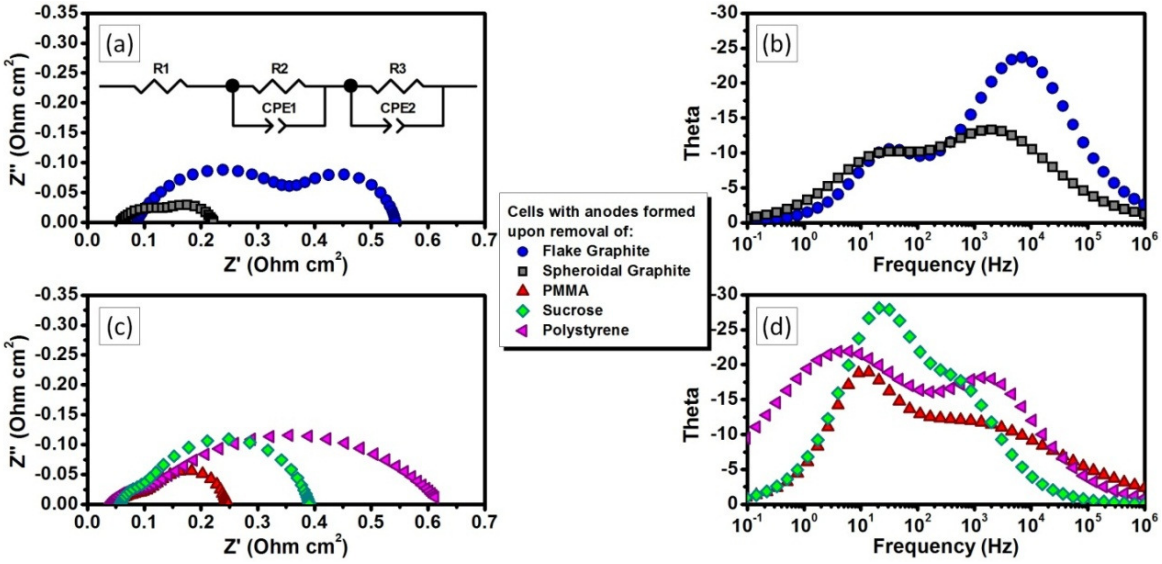

Figure 7. Cole-Cole (a) and Bode (b) plots calculated from the impedance spectra of the fuel cells with the anodes processed by removal of various pore formers. All measurements were performed at 0.5 V and 800^{o}C.

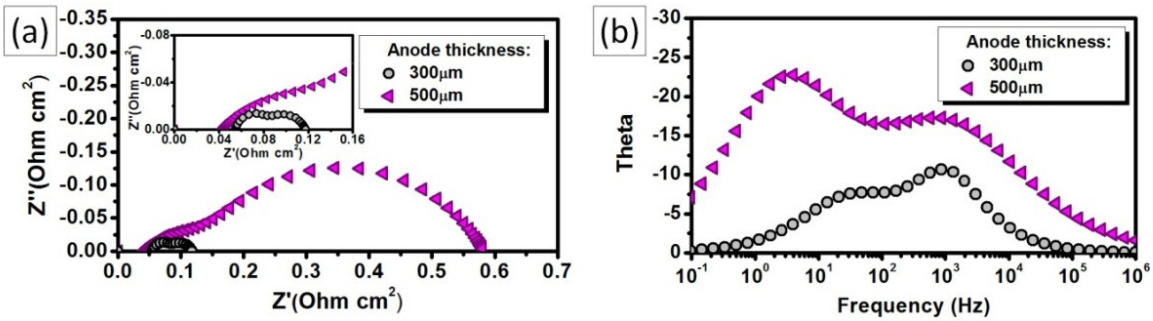

Figure 8. Cole-Cole (a) and Bode (b) plots calculated from the impedance spectra of the fuel cells with different anode thicknesses. All measurements were performed at 0.5 V and 800^{o}C [37].

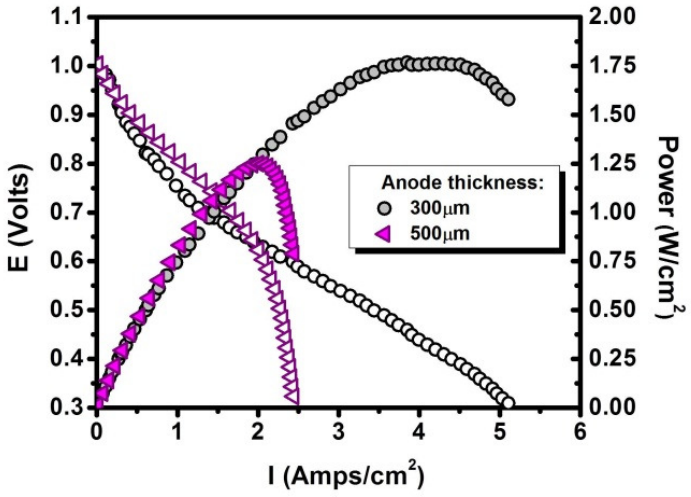

Figure 9. Measured current density - voltage curves and the associated power densities of the fuel cells with thin and thick anodes processed by removal of polystyrene particles. All measurements were performed at 800^{o}C [37].

Tables:

Table 1. Compositions of the green NiO-YSZ anode tapes in weigth and volume percents for various pore formers.

Pore former	YSZ		NiO		Dispersant		Binder		Plasticizer		Pore former	
Type	wt%	vol%	wt%	vol%	wt%	vol%	wt%	vol%	wt%	vol%	wt%	vol%
Flake graphite	23.4	11.4	40.2	17	0.3	0.7	11	29.5	5.5	15.9	19.6	25.3
Spheroidal graphite	23.4	11.4	40.2	17	0.3	0.7	11	29.5	5.5	15.9	19.6	25.3
PMMA	27.4	11.4	47	17	0.3	0.7	12.8	29.5	6.4	15.9	6.1	25.3
Sucrose	24.9	11.4	42.7	17	0.3	0.7	11.7	29.5	5.8	15.9	14.6	25.3
Polystyrene	26.2	11.4	44.9	17	0.3	0.7	12.3	29.5	6.1	15.9	10.2	25.3

Table 2. Measured bulk, open and closed porosities of the sintered and reduced Ni-YSZ anodes processed by removal of various pore formers.

	Flake graphite	Spheroidal graphite	PMMA	Sucrose	Polystyrene
Bulk porosity (%)	60.52	56.05	49.36	42.38	52.01
Open porosity (%)	55.51	56.05	49.36	32.69	52.01
Closed porosity (%)	5.01	0	0	9.69	0

Table 3. Electrical conductivity of the sintered and reduced Ni-YSZ anodes prepared by removal of various pore formers.

Flake graphite	Spheroidal graphite	PMMA	Sucrose	Polystyrene
157 S/cm	894 S/cm	1137 S/cm	1177 S/cm	1335 S/cm

Table 4. Dimensional changes and weight losses of the laminated dry NiO-YSZ anode tapes after removal of pyrolyzable components and sintering.

Pore former	Volume change	Diameter change	Thickness change	Weight loss
Flake graphite	-45.71%	-20.49%	-14.11%	37.20%
Spheroidal graphite	-50.68%	-22.01%	-18.91%	37.26%
PMMA	-54.83%	-24.96%	-20.13%	26.39%
Sucrose	-63.15%	-27.15%	-30.61%	33.33%
Polystyrene	-56.58%	-26.26%	-20.15%	30.10%

Table 5. Deconvoluted components of the measured impedance spectra of the fuel cells with the anodes processed by removal of various pore formers.

Pore former	Ohmic resistance	Magnitude of the high frequency arc	Magnitude of the low frequency arc
Type	Ohm cm^2	Ohm cm^2	Ohm cm^2
Flake graphite	0.085	0.169	0.288
Spheroidal graphite	0.059	0.075	0.089
PMMA	0.043	0.107	0.101
Sucrose	0.058	0.043	0.292
Polystyrene	0.041	0.07	0.5

4. CONCLUSIONS

This study investigated the relationships between the processing parameters, microstructures, and the electrochemical performance of the SOFC components. The research resulted in a fundamental understanding of the relationships based on microstructural characterization and electrochemical analyses to identify the parameters limiting performance of the fuel cell materials. The manuscripts then focused on performance improvements that were achieved by taking advantage of this progress in understanding. This section summarizes the conclusions of the research reported in the dissertation.

1. The change in the LSM-YSZ composite microstructures were characterized with scanning electron microscopy and impedance spectroscopy techniques. It was found out that sintering temperature has a strong influence on the microstructure of the LSM-YSZ cathodes while LSM contents from 45 vol% to 55 vol% do not have a significant effect. Two dominant polarization arcs were identified for all compositions that were sintered at temperatures ranging between 1050^{o}C and 1250^{o}C in air. The high frequency arc was correlated with the charge-exchange processes between the LSM and YSZ phases while the low frequency arc was induced by surface processes (adsorption and surface diffusion of oxygen). Although sintering at higher temperatures produced more efficient contacts between LSM and YSZ phases, which minimized the corresponding polarization resistance, coarsening of the LSM phase took place simultaneously and gave rise to the low frequency arc as surface area decreased. Therefore, the development of LSM-YSZ composite microstructures results in a trade-off between these

competing processes. The dependence of the distinct polarization resistances to the contact (neck) growth between LSM and YSZ phases and coarsening of the LSM phase – loss of surface area allowed predicting the conditions to achieve their lowest sum using the determined diagrams. As a result, the lowest total polarization resistances (0.040 Ohm cm^2 at 800^oC in air) were achieved at the minima of their combination (i.e., 50 vol% LSM – 50 vol% YSZ sintered at 1150^oC).

2. Undesired insulating phases ($La_2Zr_2O_7$ and $SrZrO_3$) were not observed in the LSM-YSZ composite cathodes upon their interactions at elevated temperatures. Formation of zirconates has been a fundamental problem for the material processing aspect of the SOFC cathodes. Although some thermodynamic models were proposed to predict their formation, the multi-component nature of the composites (i.e., Zr, Y, La, Sr, Mn and O) limited their reliability. Thus, experimental data based on the diffusion couples formed the basis for the predictions. It was claimed in the literature that stoichiometric and A-site excess LSM compositions form $La_2Zr_2O_7$ and $SrZrO_3$ due to higher solubility of La^{3+} and Sr^{2+} cations in YSZ. Utilization of A-site deficient LSM was suggested to lower the activity of these cations and eliminate the formation of zirconates. The investigations in this study confirmed the proposed mechanism and the stability of A-site deficient LSM at elevated temperatures since no zirconate formation was detected upon sintering at temperatures as high as 1250^oC in air.
3. A model was developed to predict changes in the particles of the Ag matrix (i.e. coarsening and densification) and the Ag electrode – YSZ electrolyte contact

interface (i.e. active contact area and contact resistance) during electrical and electrochemical analyses at elevated temperatures (e.g. 800^{o}C). The model involves the correlation between the identified properties of the induced Warburg polarization in semi-infinite space (i.e. characteristic relaxation frequency and polarization resistance) measured by electrochemical impedance spectroscopy technique and the active diffusion length of oxygen through Ag particles. The experimental data confirmed the predictions of the model by the ex-situ analysis of various Ag based electrodes by scanning electron microscopy.

4. Porous microstructures of Ag composites were stabilized at elevated temperatures by incorporation of oxide particles. While Ag based porous electrodes could not be used for applications requiring microstructural stability at temperatures above 550^{o}C, incorporation of LSM and YSZ particles into powder based Ag composites with comparable particle sizes (d_{50}~0.5 μm) and up to 25 vol% solids loading stabilized their porous microstructure at temperatures up to 800^{o}C and allowed their use as stable current collectors. Although various parameters determine the degree of stabilization, ratio of the particle sizes and the loading of the incorporated particles have a strong influence on the resultant microstructures and the corresponding electrical and electrochemical properties. Therefore, stable microstructures were achieved with Ag particles (d_{50} = 0.5 μm) by additions of YSZ particles with a comparable particle size (d_{50} = 0.3 μm) while severe coarsening was observed with smaller YSZ particles (d_{50} = 25 nm) at the same solids loading (20 vol %) at 800^{o}C.

5. Coating of the inner surface of the Ag based porous electrodes by nanostructured layers of various catalytically active perovskite based cathode materials (LSM, LSF and LSCF) was revealed as an effective method to stabilize the initial porous microstructures at temperatures as high as 800^{o}C in air. The size of the nanostructured perovskite grains ranged between 50 nm and 100 nm while the particles of the Ag matrix preserved their initial size (~0.5 μm) during extended holds at 800^{o}C in air. The electrochemical analyses of the nanocomposites demonstrated that the coatings contributed to the cathode reactions at the expense of their ionic conductivity and significantly lowered the polarization resistance of the Ag based porous composite layer. The decrease was from ~2.88 Ohm cm^2 to ~0.1 Ohm cm^2 in the case of LSCF coating (more than 28 times improvement). Further analysis of the impedance spectra revealed that the Ag particles behave as the main oxygen conductor of the composite layers providing significant conduction of oxygen atoms due the solubility and diffusivity of oxygen in Ag. For the first time, Ag based composites were demonstrated as efficient and stable mixed oxygen-electron conducting cathodes/current collectors for high temperature applications (>550^{o}C).
6. Combination of the powder based stabilization of the Ag composites with infiltrated nanostructured oxides allowed improving the stability of the Ag-YSZ composites at temperatures as high as 900^{o}C. It was demonstrated that an inexpensive, non-oxidizing metal such as Ag could be utilized as a stable combined cathode and current collector layer at operating conditions near melting temperature (i.e. 962^{o}C) by tailoring the microstructures to retard the densification

and coarsening of their matrix. Since Ag particles were encapsulated by a continuous nanostructured coating of YSZ by a low temperature deposition process (i.e., polymeric precursor infiltration at temperatures below 500^{o}C), the particle size of Ag was confined and no distinguishable change was observed after measurements at 900^{o}C for 1 month.

7. No diffusion or phase formation was detected at the interface of the Ag and YSZ phases upon their interactions under operating conditions (e.g. 800^{o}C in air). The eliminated high temperature densification and coarsening of the Ag based composites allowed investigations on the interactions of Ag and YSZ phases upon treatment under various polarization regimes (anodic and cathodic) and current flow at elevated temperatures. The characterization of the fundamental material interactions was performed by preparation of specific interface samples (i.e. grain-grain and grain-grain boundary) using focused ion-beam (FIB) lift-out technique and their analysis by TEM. The results answered a long-lasting question and demonstrated that Ag does not diffuse or migrate through the grain or grain boundary of dense YSZ at 800^{o}C in air.
8. Investigations on the anode layers revealed that the Ni-YSZ composite anodes are required to possess bi-modal distribution of pores for efficient electrochemical performance. The effects of the anode pore structure on the development of the Ni-YSZ anode microstructures and on the resultant electrochemical polarization mechanisms were identified. As a result, it was found out that the sub-micron pores yielded by the reduction of NiO to Ni have a significant influence on the anode activation processes as they contribute to the formation of the reaction sites

where the required phases (Ni, YSZ and pores) converge. Larger pores (>1 μm) formed by the removal of additional pyrolyzable pore former particles create the main percolating pathway for transport of the fuel and product gases. Uniform distribution of isometric pores is desired as non-uniform pores with high aspect ratio form a tortuous pathway for the gas transport and give rise to the concentration polarizations. Moreover, the high aspect ratio of the pores and their preferential non-uniform distribution results in disconnection of other phases such as Ni and increases the contribution of the porous anode layer to the ohmic polarization. Thus, it can be concluded that uniform distribution of the percolating isometric pores with diameters above 5 μm is desirable for minimizing the performance losses in Ni-YSZ anodes due to transport of gases while the uniform distribution of sub-micron pores provide active reaction sites (i.e. triple phase boundaries).

9. Polarization resistances were decreased and performance of the SOFC increased from 0.45 W/cm^2 to 1.76 W/cm^2 at 800^{o}C by utilizing the developed composite layers (i.e., anode, cathode, electrolyte and current collectors). Determined processing parameters such as compositions and dimensional changes upon sintering allowed decreasing the electrolyte thickness (<15um) without forming macro defects. These studies led to the fabrication of complete high performance SOFCs with thin YSZ electrolytes for further evaluation of the components utilizing the gained fundamental understanding of the microstructure – electrochemical performance relationships. The results demonstrated that coupling microstructural characterization techniques with electrochemical

analysis methods for identification of the electrochemical polarization mechanisms is an effective approach for optimization of the component material microstructures and fabrication of efficient SOFCs.

10. As a conclusion, the findings of this dissertation suggest that realization of the SOFC concept strongly depends on the understanding of fundamental material properties and interactions such as:
    (i) Bulk, interface and surface processes (ionic and electronic conductivity, diffusion mechanisms, surface adsorption-diffusion kinetics, charge-exchange processes, solubility and phase formations) to determine the essential properties of the constituent materials through advance characterization techniques (e.g. electron microscopy and impedance spectroscopy)
    (ii) Microstructural evolution to control the densification and coarsening of the composite phases (porous LSM-YSZ composites, porous Ag composites and porous Ni-YSZ composites) and form desired microstructures
    (iii) Chemical compatibility and thermo-mechanical changes to eliminate formation of undesired phases and ensure the integrity of the multilayer SOFC structures.

5. FUTURE WORK

This study was focused on the relationships between the processing parameters, evolution of the microstructures and the electrochemical performance of SOFCs. Based on the results and the gained understanding, some interesting topics were emerged.

1. Nanostructured composites: Considering the gained knowledge on the improvement of the microstructural stability and the electrochemical activity of the cathodes by infiltration of nanostructured oxides, effects of various infiltrated coatings can be studied in porous composites to improve their desired properties such as electronic and ionic conductivity, microstructural stability, mechanical properties and electrochemical activity. Since it is a low temperature process, it may eliminate the requirements of high temperature sintering to for a dense skeleton and allow tailoring the microstructures for novel properties.
2. Densification and coarsening kinetics of Ag composites: The stabilization of the Ag composites were investigated for high temperature applications and a strong correlation was revealed between the particle size ratio and composition of the composites. The fundamental percolation theories were not sufficient to explain the behavior of the Ag composites as they involve static states. Thus, along with the gained knowledge in the current work, the kinetics evolving the microstructures from the initial stacking and percolation of the constituent particles may be investigated to tailor their microstructures for various research and engineering applications.
3. Deconvolution of the polarization mechanisms in composite cathodes: Characterization of the polarization mechanisms and their relationships with the

microstructural features can help improving the current cathode compositions such as LSCF, LSF and their composites with electrolyte phases. As it was performed in this study, identification of the competing mechanisms and determining the minima of the induced polarization resistances has potential to lower losses due to cathode reactions.

4. Interface and grain boundary analysis: The investigations and improvements on the component materials were performed based on the scanning electron microscopy and impedance spectroscopy analysis in this study. More detailed investigations at the electrolyte-electrode interfaces, active reaction sites where all three phases merge and scaffold – nanostructured coating interfaces and grain boundaries with high resolution and analytical TEM will reveal further directions for tailoring electrochemically more efficient microstructures.
5. Modeling the electrochemical losses: Considering the useful input of the impedance spectroscopy and voltammetry techniques in this study, a universal model is required to be developed to determine the electrochemical loss mechanisms involving each component. It will help determining and distinguishing problems which can be addressed by materials research and engineering design. Thus, it may help accelerating the realization of the SOFC technology.

APPENDIX A

DEVELOPMENT OF A SILVER BASED STABLE CURRENT COLLECTOR FOR SOLID OXIDE FUEL CELL CATHODES

DEVELOPMENT OF A SILVER BASED STABLE CURRENT COLLECTOR FOR SOLID OXIDE FUEL CELL CATHODES

Ayhan Sarikaya, Vladimir Petrovsky and Fatih Dogan

Department of Materials Science and Engineering,

Missouri University of Science and Technology, Rolla, MO 65409, U.S.A.

ABSTRACT

Long term stability has been a crucial issue for the future applications of the solid oxide fuel cells (SOFCs). Current collectors for the cathodes have been among the most vulnerable components of the SOFCs due to their operation in oxidizing atmospheres at relatively high temperatures. Ag and Ag based LSM (lanthanum-strontium manganite) composites were studied to develop highly stable and low-cost current collectors compatible with other fuel cell components. In this study, no degradation was observed in the electrical conductivity and the porous microstructure of the Ag-LSM composite current collectors after 600 hours of operation at 800^{o}C in air.

INTRODUCTION

Power loss due to high resistance of contact materials has been a fundamental concern for the development of solid oxide fuel cells (SOFCs) [1, 2]. Current collection on the cathode side is more challenging than the anode side especially for the intermediate temperature (600^{o}C-800^{o}C) SOFCs due to high temperature oxidation [3-5]. Currently available current collectors include ceramics (e.g. $LaCoO_3$ and $LaCrO_3$) and

noble metals (e.g. Pt, Pd, Au and Ag) [6]. Ceramic materials have high stability in oxidizing conditions; however, their electrical conductivity is limited. Although noble metals such as Pt, Au or Pd are known as current collectors stable at high temperatures, their relatively high cost makes them less desirable for use in SOFC applications [6-8]. Ag is a relatively inexpensive candidate with various attributes such as high conductivity, high ductility and self-healing at operating temperatures [7, 9]. However, its structural instability has limited its use in operational conditions of SOFCs [7, 9, 10, 11]. Since operational temperatures of SOFCs (e.g. 800^{o}C) are fairly close to the melting temperature of pure Ag (962^{o}C), sintering between Ag particles results in near complete densification of initially porous microstructure within a relatively short time (<170 hours) with respect to the target lifetime of 40,000 hours [12] as seen in figure 1(a) and (b). The aim of this study was the development of a porous and structurally stable Ag based current collector. Current collectors were applied on stable electrolytes as symmetrical electrodes to analyze their degradation. Hence, the electrodes in this study should not be confused with actual anode and cathode materials of SOFCs. Porous Ag current collector was obtained by incorporating up to 20 vol% LSM (lanthanum-strontium manganite) particles into the Ag matrix. Percolation of Ag grains and wetting of the underlying electrolyte layer were maintained providing sufficiently high electrical conductivity to achieve efficient current collection and stable electrical contact.

EXPERIMENT

Ag and Ag-LSM inks were prepared using a polymeric vehicle (V006, Hearaeus, Conshohocken, PA, USA) and optimized for screen printing of symmetrical current

collectors on YSZ (8 mol% Y_2O_3-stabilized ZrO_2) electrolyte. Since the previous studies showed that high surface area of Ag results in structural instability [7, 13], a relatively coarse (d_{50}=1.1 μm) Ag powder (Alfa Aesar, Ward Hill, MA, USA) and an LSM (NexTech, Columbus, OH) powder with a compatible particle size (d_{50}=0.5 μm) were used. Symmetrical cells were prepared by screen printing of current collector inks on both sides of 180 μm thick YSZ electrolyte (NexTech, Columbus, OH, USA). Impedance spectroscopy and scanning electron microscopy (SEM) techniques were employed for electrochemical analysis and microstructural characterization of the cells, respectively. Electrical measurements were performed at 800^{o}C in air to simulate the operational conditions of the cathode side of SOFC.

RESULTS AND DISCUSSION

SEM micrographs shown in figure 1 demonstrate the microstructural development of pure Ag and Ag-20 vol% LSM composite after measurements for various times at 800^{o}C. Although pure Ag reached nearly full density by closing the initially open pores in a relatively short time, Ag-20 vol% LSM composite maintained its porous microstructure without any distinguishable grain growth and coarsening over 170 hours.

The solubility and mobility of oxygen within the solid Ag were widely investigated by other researchers [14, 15]. Their studies demonstrated that atomic oxygen has a significant solubility and mobility in the bulk solid Ag. The characteristic relaxation frequency of the dominating polarization mechanism was identified by analyzing the measured impedance spectra of the symmetrical cells. The temperature dependence of the characteristic frequency allowed calculating the activation energy of the polarization

mechanism. The calculated activation energy was in a good agreement with their results suggesting that the diffusion of atomic oxygen through bulk Ag is the controlling transport mechanism for oxygen and induces the polarization. Thus, for diffusion coefficient, $D_{O,Ag(s)}$, the following equation can be used with reasonable precision:

$$D_{O,Ag(s)}=4.9x10^{-3}exp(-0.503eV/RT) \quad (1, [16])$$

Since the mean diffusion time of oxygen, τ, is not dependent on the surface area in the symmetrical cell configuration, the diffusion length of the charge carrier, oxygen, can be calculated according to the following equation:

$$L_d = (D\tau)^{1/2} \quad (2, [17])$$

The mean diffusion time of oxygen, τ, can be calculated by the following equation and be correlated with the characteristic relaxation frequency, f, of the polarization mechanism measured in the impedance spectrum:

$$\tau=1/(2\pi f) \quad (3)$$

Impedance spectroscopy results of the symmetrical cell with pure Ag revealed that the characteristic relaxation frequency corresponding to the electrode reaction decreases with time (170 hours) as shown in figure 2(a). Diffusion length, L_d, was related to the frequency using the diffusion constant, $D_{O,Ag(s)}$, at the measurement temperature, 800^{o}C. Densification of initially porous Ag was reflected in the change of diffusion length through impedance spectra. The shift to the lower relaxation frequencies is attributed to higher diffusion length of oxygen atoms through larger grains of dense solid Ag as compared to shorter diffusion length of oxygen atoms through smaller grains of initially porous Ag, as shown in figure 2(b). Calculated diffusion lengths are in good

agreement with the grain sizes observed in the analysis of the densifying microstructure of pure Ag, as shown in figure 1(a-b).

The symmetrical Ag-20 vol% LSM cell exhibited an increasing relaxation frequency over an extended period of time (600 hours) as shown in figure 2(a). The shift to the higher relaxation frequencies is attributed to lower diffusion length of oxygen atoms through smaller grains of porous Ag to the electrode-electrolyte reaction interface, as shown in figure 2(b). Although the kinetics of the dominating polarization mechanism was dictated by the diffusion of oxygen through solid Ag, the amount of the transferred oxygen atoms was determined by the size of the electrode-electrolyte interface. Therefore, an increase in the contact area between Ag electrode and the electrolyte with time gives rise to the amount of the transferred oxygen atoms while decreasing the electrode polarization resistance [8]. Moreover, the expansion of the contact area allows diffusion of oxygen atoms through shorter distances and increases the characteristic relaxation frequency [18]. Calculated diffusion lengths are also comparable to the size of Ag grains observed in the micrographs. These results are in a good agreement with the analysis of the stable porous microstructure composed of Ag-20 vol% LSM as shown in figure 1(c-d).

The resistance of the YSZ electrolyte was measured by dc four-probe and impedance spectroscopy techniques to separate the ohmic resistance of the electrolyte from Ag based current collectors. An area specific resistance (ASR) of 0.25 $Ohm.cm^2$ was measured for 180 µm thick electrolytes at 800^oC using both techniques. Ohmic resistance of symmetrical cells can be obtained from the high frequency x-axis intercepts of Cole-Cole plots. Since YSZ electrolyte, symmetrical pure Ag cell and symmetrical

Ag-20 vol% LSM cell revealed the same ASR of 0.25 Ohm.cm^2, the contact resistance was negligible (~0 Ohm) and stable for both Ag based current collectors as shown in figure 3.

Densification of Ag was hindered by pinning of homogeneously dispersed LSM particles at the grain boundaries of Ag by inhibiting grain growth. Since percolation of Ag was maintained by neck formation between Ag particles, the highly conductive nature of Ag matrix remained nearly unaffected by addition of LSM. Although the Ag matrix was loaded with a relatively high amount of LSM particles (20 vol%), a strong bond at the interface with YSZ electrolyte formed without any coarsening or delamination. Near zero ohmic loss in conductance of Ag-LSM contact demonstrated here and the recently reported Cr blocking feature of LSM may realize the use of Ag-LSM current collectors with fairly inexpensive Cr containing ferritic steel as interconnect material to build SOFC stacks [6].

CONCLUSIONS

Highly stable silver based current collectors for cathodes of SOFCs were obtained from a mixture of LSM and Ag particles. Addition of LSM hindered densification of Ag particles and led to a stable porous microstructure of the composite current collector while the ohmic resistance remained unchanged after 600 hours of measurements at 800^{o}C in air.

ACKNOWLEDGEMENTS

This work was supported by a grant of the AFRL under contract no. FA4819-09-C-0018. Utilization of SEM facilities at the Graduate Center for Materials Research (MRC) of Missouri S&T is greatly acknowledged.

REFERENCES

1. W. Schafer, A. Koch, U. Herold-Schmidt, and D. Stolten, *Solid State Ionics,* **86-88,** 1235 (1996).

2. S. Koch and P.V. Hendriksen, *Solid State Ionics*, **168,** 1 (2004).

3. K. Huang, P.Y. Hou, J.B. Goodenough, *Solid State Ionics,* **129**, 237 (2000).

4. J. Piron-Abellan, V. Shemet, F. Tietz, L. Singheiser, and W.J. Quadakkers, in *Proceedings of the Seventh International Symposium on Solid Oxide Fuel Cells,* edited by H. Yokokawa, and S.C. Singhal, (PV 2001-16, The Electrochemical Proceedings Series, Pennington, NJ, USA, 2001) p. 811.

5. Z. Yang, K.S. Weil, D.M. Paxton and J.W. Stevenson, *J. Electrochem. Soc.* **150**, A1188 (2003).

6. L.T. Wilkinson, and J.H. Zhu, *J. Electrochem. Soc.* **156**, B905-B912 (2009).

7. Z. Yang, G. Xia, P. Singh, and J.W. Stevenson, *J. Power Sources* **155,** 246 (2006).

8. S.P. Simner, M.D. Anderson, J.E. Coleman, and J.W. Stevenson, *J. Power Sources* **161,** 115 (2006).

9. T.B. Sheppard and B.S.J. Kang, in *Proceedings of Materials Science and Technology Conference (MS&T) 2007*, (PV 2007-2, Detroit, MI, USA, 2007) p. 1209.

10. P. Singh, Z. Yang, V. Viswanathan, and J.W. Stevenson, *J. Mater. Eng. Perform.* **13**, 287 (2004).

11. M. Camaratta and E.D. Wachsman, *Solid State Ionics,* **178,** 1242 (2007).

12. H.U. Anderson and F. Tietz, in *High Temperature Solid Oxide Fuel Cells: Fundamentals, Design and Applications*, edited by S. C. Singhal and K. Kendall, (Elsevier Advanced Technology, Oxford, UK, 2003) p. 183.

13. W.A. Meulenberg, O. Teller, U. Flesch, H.P. Buchkremer, and D. Stöver, *J. Mater Sci.* **36,** 3189 (2001).

14. H. Möbius and B. Rohland, *Z. Chem.* **6,** 158 (1996).

15. S. Badwal, M. Bannister and M. Murray, *J. Electroanal Chem.* **168,** 363 (1984).

16. T.A. Ramanarayanan and R.A. Rapp, *Metall. Mater. Trans. B*, **3,** 3239 (1972).

17. CT. Sah, *Fundamentals of Solid-State Electronics*, (World Scientific Publishing, Singapore, 1991) p. 436.

18. M.J. Jorgensen, Ph.D. Thesis, Keele University, Staffordshire, UK, (2001).

Figures:

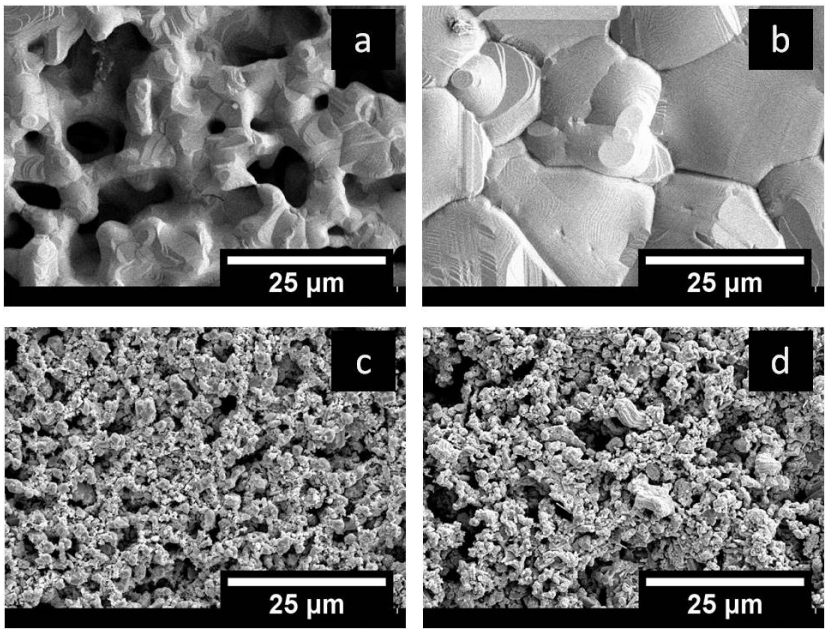

Figure 1. SEM micrographs of pure Ag (a, b) and Ag-20 vol% LSM (c, d), both obtained after 2 hours and 170 hours measurements at 800^{o}C, respectively.

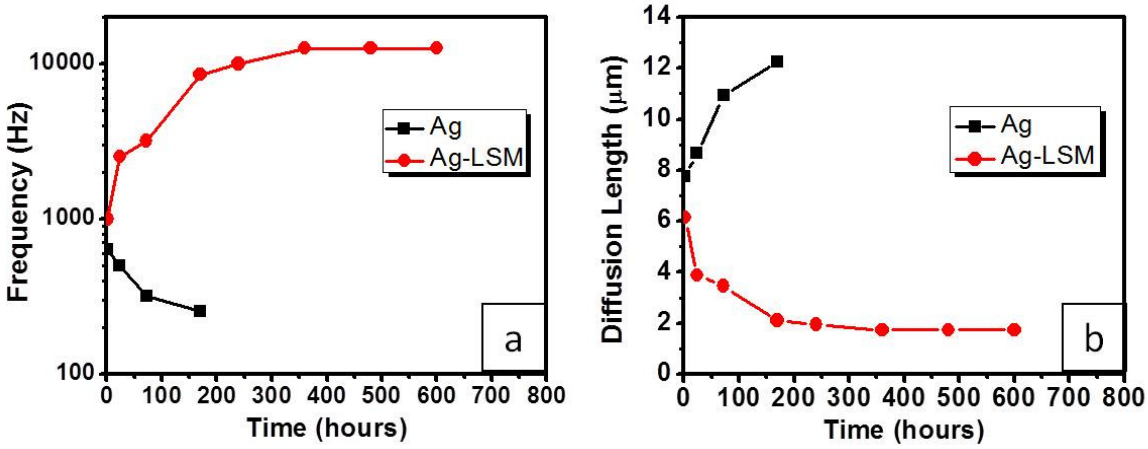

Figure 2. Characteristic relaxation frequency (a) and diffusion length (b) as functions of time, calculated from the impedance spectra of the pure Ag and Ag-20 vol% LSM cells measured at 800°C, respectively.

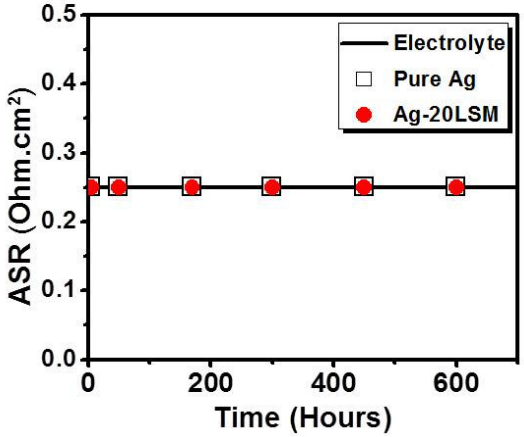

Figure 3. Area specific resistances of the YSZ electrolyte, symmetrical pure Ag cell and symmetrical Ag-20 vol% LSM cell at 800°C as a function of time.

APPENDIX B

EFFECT OF THE ANODE MICROSTRUCTURE ON THE ENHANCED PERFORMANCE OF SOLID OXIDE FUEL CELLS

EFFECT OF THE ANODE MICROSTRUCTURE ON THE ENHANCED PERFORMANCE OF SOLID OXIDE FUEL CELLS

Ayhan Sarikaya, Vladimir Petrovsky, Fatih Dogan

Department of Materials Science and Engineering,

Missouri University of Science and Technology, Rolla, Missouri 65409, USA

Abstract

Anode microstructure has a vital effect on the performance of anode supported solid oxide fuel cells. High electrical conductivity, gas permeability and low polarization are the required features of anodes to achieve high power densities. The desired properties of the anodes were obtained by modifying their microstructural development using pyrolyzable pore former particles without introducing any functional layers and compositional modifications. The microstructures of fabricated anodes were characterized using scanning electron microscopy and mercury intrusion porosimetry techniques while their electrochemical properties were identified using impedance spectroscopy and voltammetric measurements. Detailed investigations demonstrated that the pore structure has a major impact on the electrical conductivity, polarization and gas permeability of the anodes. Through tailoring of conventional anode microstructures, a significantly high power density of 1.54W/cm^2 was achieved at 800^{o}C using diluted hydrogen (10% H_2 in argon) as fuel.

Keywords

Solid oxide fuel cells; Anode; Microstructure; Porosity; Pore former; Power density

1. Introduction

Solid oxide fuel cells (SOFCs) are attractive power generation systems mainly due to their high conversion efficiencies and low emissions with flexible fuel options; however, cost and reliability are remaining concerns for their realization [1]. Increase in the performance can help reduce the cost for unit power production and allow feasible SOFC applications.

Electrochemical performance of a fuel cell is limited by various polarization mechanisms such as (i) activation polarization, (ii) ohmic polarization and (iii) concentration polarization. They result in a decrease in the voltage of the fuel cell as it provides current to maintain a certain power output. The sluggish kinetics of the electrode reactions give rise to the activation polarization while the electrical resistance of the components (e.g. electrolyte, electrodes and contacts) induce the ohmic polarization. The concentration polarization also arises as the transport of the reactant and/or product gases is retarded [2-4].

The conventional SOFC configuration consists of a dense yttria stabilized zirconia (YSZ) electrolyte between a porous lanthanum-strontium manganite (LSM) – YSZ cathode and a porous Ni – YSZ anode [5, 6]. In order to increase the power density, the efficiencies of the electrodes need to be improved while the electrolyte and contact resistances are decreased to lower the ohmic losses. As many attempts were made to decrease the thickness of the electrolyte in order to minimize its contribution to the ohmic polarization, anode supported design with a thin electrolyte gained importance and has been extensively investigated recently [7, 8].

Several studies demonstrated that the microstructures of the component layers have crucial effect on the performance of the SOFCs [9-11]. Among all of the components, anode plays a critical role in oxidation of fuel and generation of electrons in the anode supported SOFC design [12-17]. Ni-YSZ anode layer is required to provide (i) high electronic and ionic conductivity, (ii) uniform distribution and percolation of all three phases (YSZ, Ni and pores), (iii) fine grain sizes with high surface area for enhanced catalytically activity and (iv) high permeability for the fuel gas and the reaction products [11, 18-23].

Since it was relatively challenging to satisfy all of the requirements of a high performance SOFC in a single anode layer with a uniform microstructure and composition, various modifications in the cell design have been pursued to improve the electrochemical performance of the anode layers [24, 25]. Application of a functional layer between the anode and electrolyte layers was proposed to decrease the activation and concentration polarizations of the anode layer [3]. The functional layer consisted of finer grains and pore structure than the supporting anode layer. Outer supporting anode was relatively thick (~1mm) and provided the mechanical strength as well as delivery of gases through the open pore channels among its coarse grains. Since the electrochemical activity took place in the anode functional layer, it had to provide uniform distribution of the phases (e.g. YSZ, Ni and pores) while providing extended reaction sites for the electrochemical reactions to meet the requirements of a high performance SOFC [26]. Therefore, optimization of the fine microstructure of the functional layer gave rise to the power density of the fabricated cells.

Numerous approaches were suggested considering the prospective results obtained with functional layers. Grading the microstructure from coarse to fine towards the electrolyte has been one of the common approaches employed for improving the performance of the anodes. Grading of the anode microstructure was achieved by fabricating multi-layer configurations. Usually, composition, grain size, pore structure and porosity vary in each layer to provide the desired grading of the anode. Recently, improved power densities were reported by several researchers using this technique [27-29]. Another common approach is based on incorporation of various catalytically active materials to the anode functional layer to decrease the activation polarization of the anode. Introduction of materials such as gadolina-doped ceria and samaria-doped ceria to the anode functional layer was resulted in distinguishable increase in the power density of the fabricated SOFCs [30-32].

Despite the significant success achieved by these methods, incorporated materials lead to various issues such as material interactions resulting in formation of undesired phases at elevated temperatures required for their processing or the operation of the SOFCs [33, 34]. The sintering shrinkage and the thermal expansion of the anode functional layer are affected by compositional modifications and give rise to structural incoherence between component layers during sintering as well as fuel cell operation. These dissimilarities between the fuel cell components lead to formation of macroscopic defects such as cracks, delamination and warpage [35-38]. Although some of these consequent challenges can be addressed by modifying the compositions and processing techniques, each additional step establishes new complications and increases the cost of fuel cell fabrication. Providing the desired properties in a uniform single Ni-YSZ anode

layer could address these challenges and lead to enhanced reliability of fuel cells. However, the microstructure needs to be optimized to meet the fundamental needs of a high performance SOFC and it requires a detailed understanding of the relationship between anode microstructure and SOFC performance. Moreover, use of conventional materials and fabrication techniques for this purpose would make the SOFCs more feasible by decreasing the cost further while providing enhanced reliability [39, 40].

Although various methods have been employed for the fabrication of planar SOFCs, tape casting of both anode and electrolyte layers, lamination of tapes prior to sintering and screen printing of the cathode layer has been the most common production route [41,42]. Incorporation of pore former particles has been an effective technique to produce controlled porosity in the anode microstructures since the particles leave pores with adjustable properties as the green ceramic is introduced to elevated temperatures for sintering [19, 43].

This study is focused on understanding the relationship between the anode microstructure and its resultant electrochemical performance to combine all of the required properties on a single anode layer without adding an anode functional layer or applying a compositional/microstructural grading. Distinct pore structures were fabricated by incorporating two pyrolyzable pore formers with significantly different powder characteristics such as morphology and thermal decomposition/oxidation behavior. Developed single anode microstructures were applied to a thin YSZ electrolyte (~10µm) and LSM-YSZ cathode configuration to fabricate complete SOFCs. Detailed analyses of the anode microstructures and the electrochemical performance of the cells revealed novel results with respect to performance improvements through modification of

the pore structure. Although identical compositions were used, utilization of a different pore former led to evolution of a significantly diverse microstructure and improved the cell performance more than three times. The developed Ni-YSZ/YSZ/LSM-YSZ cells exhibited power densities over 1.5 W/cm^2 at 800^{o}C using diluted hydrogen (10% H_2 in Ar) on the anode side and air on the cathode side.

2. Experimental

The investigated anode supported SOFCs consist of a porous Ni-YSZ anode, YSZ electrolyte, LSM-YSZ cathode and a porous LSM current collecting layer. Anode and electrolyte tapes were tape cast and laminated together. Inks of LSM-YSZ and LSM were screen printed on the electrolytes after their co-sintering with anode tapes. All of the materials used for the investigations are commercially available.

Various materials have been used as pore formers for the fabrication of porous SOFC anodes. They are usually either in spherical or plate like geometries. Flake graphite with plate like morphology has been widely investigated and used for porous electrode fabrication [10, 19, 43, 44]. Although there are various techniques to control the desired properties of graphite such as purity, they are relatively expensive and poor in yielding desired particle size, shape and purity of the graphite particles [45, 46]. Polymethyl methacrylate (PMMA) spheres have also been successfully utilized as pore formers for the fabrication of porous anodes. Recently reported high performance SOFCs using porous anodes formed by incorporating PMMA particles made it an attractive candidate for optimization of anode microstructures [39, 47-49]. Production of PMMA is relatively inexpensive and it allows controlling the size of the pore formers in a wide range with

nearly zero contamination [50]. Thus, the common pore former, flake graphite, and the promising pore former candidate, spherical PMMA, were employed as pore formers to form anode microstructures with distinguishable microstructural features such as shape and distribution of the pores, and percolation of the constituent phases.

2.1. Fabrication

Ceramic slurries of the electrolyte and anode tapes were prepared using two and three stage preparation techniques, respectively. The compositions used to make the anode slurries are shown in Table 1. The rheological properties of the slurry would vary according to the features of the incorporated pore formers. Therefore, compositional changes are required to be made on the slurries to obtain defect free tapes. Use of more binder would increase the porosity and the comparison would be biased as it is known that additional binder also has pore forming effect [11]. Thus, the compositions of the anode slurries were optimized for this study to be able to use the same volumetric loading of the components for both pore formers for the sake of a reliable comparison.

In the first stage, YSZ powder (TZ-8Y, Tosoh, Tokyo, Japan), solvents (ethanol and toluene) and dispersant (KD-1, ICI, Barcelona, Spain) were mixed for one day to achieve a uniformly dispersed suspension for the electrolyte tape slurries. This stage also included the addition of the NiO (NiO-F, NexTech, Columbus, OH, USA) powder to the mixture for the anode tape slurries. In the second stage, the binder (PVB-79, Monsanto, St. Louis, MO, USA) and plasticizer (Dioctyl Phthalate, Sigma-Aldrich, St. Louis, MO, USA) were added to the slurry and mixed for one day. The third stage consisted of the addition of the pore formers to the slurry and further mixing for one more day to achieve homogeneous

dispersion of the constituents for the anode tapes. High purity pore formers of flake graphite (LBG2025, Superior Graphite, Chicago, IL, USA) and PMMA (2041, Sekisui, Osaka, Japan) were used for the fabrication of the anode tapes. The mixed slurries were then degassed for 5 min under vacuum and cast into tapes. The dried thicknesses of the anode and electrolyte tapes were around 100µm and 14µm, respectively. One electrolyte and six anode tapes were laminated together at 80^{o}C using a pressure of 25 MPa. The thickness of the laminates ranged between 600-620µm. The laminated tapes of the anodes with PMMA and flake graphite were heated to 210^{o}C and 600^{o}C, respectively, to remove the binder and pore formers. The sintering step is required to allow the densification of the thin YSZ electrolyte for gas tightness while maintaining fine grains, high surface area and porosity of the NiO-YSZ composite by controlled grain growth and densification. Therefore, sintering conditions were optimized and the lowest temperature and shortest time was identified for the densification of the electrolyte for this particular configuration. As a result, laminated anode and electrolyte tapes were co-sintered in air at 1350^{o}C for 2 hours.

Cathode current collector ink was prepared by mixing LSM powder (LSM20-HP, NexTech, Columbus, OH, USA) with an organic vehicle (V-006, Heraeus, Conshohocken, PA, USA). 50vol% of the LSM powder was replaced with the YSZ powder for the cathode layer. Cathode layer was screen printed on the co-sintered electrolyte and sintered in air at 1150^{o}C for 1 hour. Cathode current collecting layer was screen printed on the cathode layer and sintered in air at 1150^{o}C for 1 hour. The cathode and the cathode current collecting layers as well as the electrolyte layer were kept the same for all of the fabricated fuel cells. Hereafter, fabricated SOFCs with anode layers

prepared by incorporating flake graphite and PMMA will be called cell A and cell B, respectively.

2.2. Characterization

Utilization of scanning electron microscopy and mercury intrusion porosimetry methods provided a thorough analysis of the anode microstructures while impedance spectroscopy technique along with the voltammetric measurements allowed identification of the electrochemical performance loss mechanisms of the fabricated SOFCs.

The microstructures of the anodes were characterized using mercury intrusion porosimetry and scanning electron microscopy techniques. Four probe electrical conductivity measurements were also employed for the analysis of the Ni-YSZ anodes. Electrochemical performance investigations and also impedance spectroscopy measurements were done using a combined potentiostat and frequency response analyzer (Solartron, 1470 CellTest, Mobrey, UK). Samples were around 27mm in diameter and 500μm in thickness with a cathode layer area of $0.3cm^2$. Pt wires were used on both cathode and anode sides and fixed by Pt paste to provide reliable electrical contacts. All measurements were performed at 800^oC. Considering operational conditions of SOFCs in stacks, a diluted hydrogen mixture (10% H_2 in Ar) was used as fuel. It was humidified by bubbling through water at 20^oC prior to introducing it to the anode side of the SOFCs during measurements. An oxygen partial pressure (pO_2) of $2.99x10^{-20}$atm and a hydrogen to water ratio (pH_2/pH_2O) of 4.29 was estimated in the fuel at 800^oC. Air flow was also maintained on the cathode side simultaneously.

3. Results and Discussion

Fig. 1 demonstrates the typical cross section of a fabricated anode supported SOFC. Electrolyte, cathode and cathode current collection layers had the same thickness around 10μm after sintering. The thicknesses and microstructures of these layers were identical for all of the investigated fuel cells. Morphologies and particle sizes of the flake graphite and PMMA are shown in Fig. 2(a) and (c), respectively. Both flake graphite and PMMA particles were relatively polydispersed while the particles of the flake graphite exhibited a distinct anisometry. Since the final microstructures of the porous ceramics resemble the morphological features of the pyrolyzable pore formers, fabricated anode microstructures demonstrated distinct features mainly due to the dissimilar geometries of flake graphite and PMMA pore formers. Although the volume fractions of the pore former loadings in the anode tapes were identical, their shapes and particle size distributions resulted in significantly different pore structures. Flake graphite yielded pores representing high aspect ratio (>>1) of its plate like shape with preferred alignment along the tape cast direction (Fig. 2(b)) while PMMA left pores resembling its spherical shape and the uniform distribution in the sintered microstructure as shown in Fig. 2(d). The particles of flake graphite align parallel to the electrolyte as the tapes were stacked for the lamination and co-sintering. Alignment of the pore channels almost perpendicular to the gas flow direction towards the electrolyte may not be preferable for the efficient transport of gases due to the tortuous path it forms.

The observed grain sizes of both Ni and YSZ phases were ~0.5μm and no distinguishable size difference was detected in all of the fabricated anodes. It suggests that lowering the sintering temperature (1350^{o}C) and time (2 hours), allowed inhibiting

the exaggerated grain growth and maintained high surface area of the initial fine particles of NiO (d_{50}=0.5µm) and YSZ (d_{50}=25nm) upon sintering. Moreover, the incorporated pore former did not have any distinguishable influence on the final grain sizes of the solid phases.

Analysis of the mercury intrusion porosimetry results allowed further characterization of the porosities of the reduced anodes. Although flake graphite yielded higher total bulk porosity (~60%) than PMMA (~50%), 8% of the pores were closed and could not be penetrated by mercury even at high pressures (over 200 MPa) while all of the pores were open in the anode of the cell B. Highly anisometric particles of flake graphite resulted in bridging of the pore former particles and yielded higher bulk porosity while isometric particles of PMMA formed less bulk porosity at the same volumetric loading. Smaller dimensions of the pores left by the pore formers with high aspect ratios are more prone to collapsing during further densification. Thus, some of the initially open pores of the anode of the cell A left by the flake graphite collapsed and got isolated upon sintering at 1350^{o}C.

Similar amounts of open porosity were obtained with both pore formers; however, size, distribution, and connectivity of the pores exhibited distinct features. Although anodes of both cell A and cell B demonstrated the majority of the intrusion through their pore channels with a diameter below 2µm, abundance of their pores in two extreme pore size ranges were relatively different as shown in Fig. 3. Anode of the cell B allowed intrusion of ~15% of its total porosity in the pore size range between 100µm and 2µm while anode of the cell A allowed intrusion of only ~5% of its total porosity in the same pore size range. It suggests the improved connectivity of the large pores with uniform

distribution left by PMMA particles. The second major difference was observed in the submicron pores. Although incorporated pore formers could not be expected to yield any fine porosity due to their relatively large particles, the NiO constituent of the composite anode was capable of forming a significant amount of fine porosity upon reduction as the volume of the NiO decreases ~40% upon reduction to Ni. Considering the initial particle size of the NiO powder (d_{50}=0.5µm) and the observed average grain size (d_{50}=0.5µm) of the anode after reduction, submicron pores were expected to be observed. However, no pores were detected in the anode of the cell A smaller than 0.2µm in diameter, while the intrusion of the Hg into the anode of the cell B took place through the pores smaller than 0.06µm in diameter. Considering the closed porosity and the limited intrusion of Hg at high pressures (>200 MPa), flake graphite did not yield a continuous pore structure. Moreover, formed pores did not access to the fine microstructure of the grains with pores smaller than 0.2µm in diameter. Thus, the anode of the cell A did not satisfy the requirement of the percolation of pores and could not be expected to allow transport of the gases to the reaction sites. On the other hand, completely open porosity (~50vol%) of the anode of the cell B along with the continuous intrusion into the pores with diameters below 0.06µm suggests a percolating pore structure which allows gas transport to relatively small pores surrounded by fine grains with significantly high surface area. Hence, the analyses of the results of mercury intrusion porosimetry measurements were in a good agreement with the microstructural features of the anodes observed in the micrographs shown in Fig. 2(b) and (d).

Electrical conductivity of the anode is strongly affected by several parameters such as (i) composition, (ii) pore structure, (iii) size of the grains and (iv) percolation of the

electrically conductive phase, Ni [3, 20]. Thus, electrical conductivity measurements were performed on the anodes of the cell A and the cell B at 800^{o}C in flowing humidified 10% H_2 in Ar to simulate the operational conditions. Four probe conductivity measurements of the anode of the cell A demonstrated a conductivity of 157 S.cm^{-1} which is relatively lower than the required conductivity (>1000 S.cm^{-1}) for an efficient anode layer [51, 52]. A significantly improved conductivity of 1137 S.cm^{-1} was measured in the anode of cell B. Although the same composition of the components was used and similar amounts of open porosity was measured with the anodes of both cell A and cell B, change of the pore structure improved the electrical conductivity of anode more than seven times and allowed achieving the required level for an efficient anode. It confirms the expected adverse effect of the non-uniform pore structure of the anode of the cell A on the connectivity of the conducting phase, Ni. The pore structure of the cell A did not only deteriorate the percolation of the pores but also the percolation of the Ni phase. Thus, discontinuity of the Ni grains resulted in the increase of the electrical resistance [53].

Fig. 4 shows the results of the voltammetric measurements performed on the cell A and the cell B. Considering the partial pressures of oxygen maintained on the anode (pO_2=2.99x10^{-20}atm) and the cathode sides (pO_2=0.209atm) a theoretical open circuit voltage (OCV) of 1.003V was expected at 800^{o}C. Both configurations of the cells showed identical OCVs over 1V confirming their dense and leak-free electrolytes observed in the cross sectional micrographs shown in Fig. 1. The maximum power density of 1.54W/cm^2 was obtained with the cell B while the cell A demonstrated the

maximum power density of 0.45W/cm^2 at 800^{o}C. Cell A and cell B also showed the power densities of 0.33W/cm^2 and 1.29W/cm^2 at 0.7V, respectively.

Considering that the investigation of the fuel cells at their peak power densities would allow the analysis of all perfomance limiting contributions, impedance spectra were measured at the potential of 0.5V. Ohmic polarization resistance of the cells can be obtained from the high frequency x-axis intercepts of Cole-Cole plots [27]. Cell B demonstrated an ohmic resistance of 0.043 Ohm.cm^2 while cell B demonstrated an ohmic resistance of 0.085 Ohm.cm^2 as shown in Fig. 5(a). Since the anode layer was the only different component and identical results were reproduced with multiple sets of samples, it can be concluded that the change in the anode microstructure resulted in different ohmic resistances. This is in agreement with the results of four probe electrical conductivity measurements. Low electrical conductivity (157 S.cm^{-1}) of the anode of cell A gave rise to the ohmic loss and led to an increase in the total cell resistance. Further analysis of the impedance spectra showed that the previously developed cathode did not demonstrate any limitation in these cell configurations and both low and high frequency arcs are associated with the anode layer [54]. Deconvolution of the spectra also revealed that the high frequency arc (~10 kHz) corresponds to the anode activation processes which is in a good agreement with the studies reported in the literature [55-57]. The anode activation polarization of the cell A was 0.169 Ohm.cm^2 while it was 0.107 Ohm.cm^2 on the cell B. It confirms that the interrupted percolations of the pores and the Ni phase in the anode did not only decrease the electrical conductivity but also decreased the electrochemical performance of the Ni-YSZ anode. Thus, well developed percolation of all three phases in the anode of the cell B gave rise to the electrochemical performance

as well as the electrical conductivity. Even though the obtained identical size of the grains in both anode microstructures and the characteristic frequencies of their activation processes shown in Fig. 5(b) suggested similar natures, the lack of the percolation of the phases resulted in disconnected reaction sites in the anode of the cell A. Therefore, improved percolation of all of the three phases resulted in a relatively higher amount of active reaction sites and higher electrical conductivity which gave rise to the performance of the cell B [58].

Since a diluted (10% H_2 in Ar) and water-rich fuel (pH_2/pH_2O=4.29) was utilized to simulate the operational conditions of the SOFCs in stacks, the delivery of the fuel and removal of the product water could suffer and give rise to the concentration polarization on the anode side. The concentration polarization would also be more pronounced at the utilized cell potential (0.5V) for the measurements. Further analysis of the impedance spectra demonstrated that the low frequency arc (~10Hz) corresponds to the limitation of the gas transport through the anode [59]. Although a smaller amount of current (~0.9 $Amps.cm^{-2}$) was drawn from the cell A suggesting a lower utilization of fuel gas, a relatively high concentration polarization (~0.288 $Ohm.cm^2$) was observed. A significant amount of current was (~3 $Amps.cm^{-2}$) drawn from the cell B during the measurements; however, a lower concentration polarization resistance (~0.101 $Ohm.cm^2$) was observed. The difference in the measured concentration polarization resistances also agree with the previously observed percolation of pores in the anode microstructures of the cell A and the cell B. Completely open porosity and the enhanced connectivity of the small and large pores in the anode microstructure of the cell B allowed a significant improvement in the delivery of the fuel gas as well as removal of the water-rich product gas through the

anode layer. Moreover, the effect of the concentration polarization would decrease further as the operational cell potential (0.5V) is increased to higher values (0.7V-0.9V) for improved fuel utilization in SOFC stacks.

Since relatively large pores (1µm-100µm) were obtained upon high temperature sintering (1350^{o}C) and submicron pores were formed by reduction of NiO, significant microstructural changes were not expected at the operational temperatures (e.g. 800^{o}C). Although coarsening of Ni grains could take place after reduction, the investigations on the fuel cells and single anode layers after reduction and measurements in operational conditions for prolonged time (~200 hours) did not reveal any distinguishable change in grain and pore sizes as well as pore size distributions with time suggesting the stability of the formed anode microstructures.

4. Summary and Conclusions

The results reported here are based on the observed significant increase in the power density as a consequence of the difference in the anode microstructures formed by using identical volumetric loadings of two different pore formers. Although earlier percolation of the pore formers with high aspect ratios (>>1) such as flake graphite could be easily expected to create more porosity, the pore structure, uniform distribution and percolation of the phases (e.g. Ni, YSZ and pores) are more important criteria for high electrochemical performance of anodes. Thus, the pore formers with low aspect ratios (~1) such as PMMA produce more uniform anode microstructures and yield open porosity, which result in increased electrical conductivity by percolation of all phases and

improved electrochemical performance even at lower total porosity than the porosity formed by the flake graphite.

Achieved significantly high power density of 1.54W/cm^2 confirmed that conventional powder based fabrication techniques have potential to exhibit enhanced performances by tailoring the electrode microstructures. Considering the obtained novel results, highly efficient anode microstructures can be fabricated by adjusting the morphological properties and loading of pore formers without introducing functional layers or modifying the anode compositions.

Acknowledgement

This work was supported by a grant of the AFRL under contract no. FA4819-09-C-0018. Utilization of SEM facilities at the Graduate Center for Materials Research (MRC) of Missouri S&T is greatly acknowledged.

References

[1] Xia C, Liu M. A simple and cost-effective approach to fabrication of dense ceramic membranes on porous substrates. J Am Ceram Soc 2001;84(8):1903-1905.

[2] Chan SH, Khor KA, Xia ZT. A complete polarization model of a solid oxide fuel cell and its sensitivity to the change of cell component thickness. J Power Sources 2001;93(1-2):130-140.

[3] Virkar AV, Chen J, Tanner CW, Kim J-W. The role of electrode microstructure on activation and concentration polarizations in solid oxide fuel cells. Solid State Ionics 2000;131(1-2):189-198.

[4] Chan SH, Xia ZT. Polarization effects in electrolyte/electrode-supported solid oxide fuel cells. J Appl Electrochem 2002;32(3):339-347.

[5] Kuhn M, Napporn TW, Meunier M, Therriault D. Single-chamber micro solid oxide fuel cells: Study of anode and cathode materials in coplanar electrode design. Solid State Ionics 2010;181(5-7):332-337.

[6] Appari S, Janardhanan VM, Jayanti S, Maier L, Tischer S, Deutschmann O. Micro-kinetic modeling of NH_3 decomposition on Ni and its application to solid oxide fuel cells. Chem Eng Sci 2011;66(21):5184-5191.

[7] Minh NQ. Solid oxide fuel cell technology-features and applications. Solid State Ionics 2004;174(1-4):271-277.

[8] Yakabe H, Hishinuma M, Uratani M, Matsuzaki Y, Yasuda I. Evaluation and modeling of performance of anode-supported solid oxide fuel cell. J Power Sources 2000;86(1-2):423-431.

[9] Wilson JR, Barnett S, Electrochem Solid-State Lett 2008;11(10):B181–B185.

[10] Choi JH, Lee T, Park T-S, Yoo K-B, Yoo Y-S. Microstructure and performance of anode supported cell by pore size of anode. In: Weidner J, Narayanan SR, editors. ECS Transactions, Vol. 16, The Electrochemical Society, Pennington, 2009, pp. 37-42.

[11] Boaro M, Vohs JM, Gorte RJ. Synthesis of highly porous yttria-stabilized zirconia by tape-casting methods. J Am Ceram Soc 2004;86(3):395-400.

[12] Kim S, Kwon O, Kumar S, Xiong Y, Lee C. Development and microstructure optimization of atmospheric plasma-sprayed NiO/YSZ anode coatings for SOFCs. Surf Coat Technol 2008;202(14):3180-3186.

[13] Lee JH, Moon H, Lee H-W, Kim J, Kim J-D, Yoon K-H. Quantitative analysis of microstructure and its related electrical property of SOFC anode, Ni–YSZ cermet. Solid State Ionics 2001;148(1-2):3180-3186.

[14] Minh NQ. Ceramic fuel cells. J Am Ceram Soc 1993;76(3):563–88.

[15] Brown M, Primdahl S, Mogensen M. Structure/performance relations for Ni/yttria-stabilized zirconia anodes for solid oxide fuel cells. J Electrochem Soc 2000;147(2):475–485.

[16] Lee C-H, Lee C-H, Lee H-Y, Oh S-M. Microstructure and anodic properties of Ni/YSZ cermets in solid oxide fuel cells. Solid State Ionics 1997;98(1-2):39–48.

[17] Jiang S-P, Callus PJ, Badwal SPS. Fabrication and performance of Ni/3 mol% Y_2O_3–ZrO_2 cermet anodes for solid oxide fuel cells. Solid State Ionics 2000;132(1-2):1-14.

[18] Simwonis D, Naoumidis A, Dias FJ, Linke J, Moropoulou A. Material characterization in support of the development of an anode substrate for solid oxide fuel cells. J Mater Res 1997;12(6):1508-1518.

[19] Clemmer RMC, Corbin SF. Influence of porous composite microstructure on the processing and properties of solid oxide fuel cell anodes. Solid State Ionics 2004;166(3-4):251-259.

[20] Atkinson A, Barnett S, Gorte RJ, Irvine JT, McEvoy AJ, Mogensen M, et al. Advanced anodes for high-temperature fuel cells. Nat Mater 2004;3(1)17-27.

[21] Marinšek M, Zupan K, Maček J. Preparation of Ni–YSZ composite materials for solid oxide fuel cell anodes by the gel-precipitation method. J Power Sources 2000;86(1-2):383-389.

[22] Simwonis D, Thülen H, Dias FJ, Naoumidis A, Stöver D. Properties of Ni/YSZ porous cermets for SOFC anode substrates prepared by tape casting and coat-mix® process. J Mater Process Technol 1999;92-93(1):107-111.

[23] Holzer L, Münch B, Iwanschitz B, Cantoni M, Hocker Th, Graule Th. Quantitative relationships between composition, particle size, triple phase boundary length and surface area in nickel-cermet anodes for solid oxide fuel cells. J Power Sources 2011;196(17):7076-7089.

[24] Kong J, Sun K, Zhou D, Zhang N, Mu J, Qiao J. Ni–YSZ gradient anodes for anode-supported SOFCs. J Power Sources 2007;166(2):337-342.

[25] Jeon DH, Nam JH, Kim CJ. Microstructural optimization of anode-supported solid oxide fuel cells by a comprehensive microscale model. J Electrochem Soc 2006;153(2):A406-A417.

[26] Vivet N, Chupin S, Estrade E, Piquero T, Pommier PL, Rochais D, et al. 3D microstructural characterization of a solid oxide fuel cell anode reconstructed by focused ion beam tomography. J Power Sources 2011;196(18):7541-7549.

[27] Wang Z, Zhang N, Qiao J, Sun K, Xu P. Improved SOFC performance with continuously graded anode functional layer. Electrochem Commun 2009;11(6):1120-1123.

[28] Han MF, Yin H-Y, Miao W-T, Zhou S. Fabrication and properties of anode-supported solid oxide fuel cell. Solid State Ionics 2008;179(27-32):1545-1548.

[29] Mukhopadhyay M, Mukhopadyay J, Sharma AD. Multilayered SOFC anode structure with electroless Ni-YSZ for enhancement of cell performance. In: Singhal S, Eguchi K, editors. ECS Transactions, Vol. 35, The Electrochemical Society, Pennington, 2011, pp. 1293-1302.

[30] Nguyen WL, Kobayashi K, Honda T, Iimura Y, Kato K, Neghisi A, et al. Fabrication preparation and evaluation of doped ceria interlayer on supported stabilized zirconia electrolyte SOFCs by wet ceramic processes. Solid State Ionics 2004;174(1-4):163-174.

[31] Ai N, Lü Z, Tang J, Chen K, Huang X, Su W. Improvement of output performance of solid oxide fuel cell by optimizing Ni/samaria-doped ceria anode functional layer. J Power Sources 2008;185(1):153-158.

[32] Ai N, Lü Z, Chen K, Huang X, Du X, Su W. Effects of anode surface modification on the performance of low temperature SOFCs. J Power Sources 2008;171(2):489-494.

[33] Zhou XD, Scarfino B, Anderson HU. Electrical conductivity and stability of Gd-doped ceria/Y-doped zirconia ceramics and thin films. Solid State Ionics 2004;175(1-4):19-22.

[34] Tsoga A, Naoumidis A, Stöver D. Total electrical conductivity and defect structure of ZrO_2–CeO_2–Y_2O_3–Gd_2O_3 solid solutions. Solid State Ionics 2000;135(1-4):403-409.

[35] Mücke R, Menzler NH, Buchkremer HP, Stöver D. Cofiring of thin zirconia films during SOFC manufacturing. J Am Ceram Soc 2008;92(s1):S95-S102.

[36] Park H-G, Moon H, Park S-C, Lee J-J, Yoon D, Hyun S-H, et al. Performance improvement of anode-supported electrolytes for planar solid oxide fuel cells via a tape-casting/lamination/co-firing technique. J Power Sources 2010;195(9):2463-2469.

[37] Malzbender J, Steinbrech RW. Advanced measurement techniques to characterize thermo-mechanical aspects of solid oxide fuel cells. J Power Sources 2007;173(1):60-67.

[38] Li W, Hasinska K, Seabaugh M, Swartz S, Lannutti J. Curvature in solid oxide fuel cells. J Power Sources 2004;138(1-2):145-155.

[39] Talebi T, Sarrafi MH, Haji M, Raissi B, Maghsoudipour A. Investigation on microstructures of NiO–YSZ composite and Ni–YSZ cermet for SOFCs. Int J Hydrogen Energy 2010;35(17):9440-9447.

[40] Suzuki T, Hasan Z, Funahashi Y, Yamaguchi T, Fujishiro Y, Awano M. Impact of anode microstructure on solid oxide fuel cells. Science 2009;325(5942):852-855.

[41] Basu RN, Sharma AD, Dutta A, Mukhopadyay J. Processing of high-performance anode-supported planar solid oxide fuel cell. Int J Hydrogen Energy 2008;33(20):5748-5754.

[42] Yoon KJ, Ye G, Gopalan S, Pal UB. Cost-effective single step cofiring process for manufacturing solid oxide fuel cells using HSC^{TM} anode. J Fuel Cell Sci Technol 2010;7(2): 210101–210105.

[43] Corbin SF, Apté PS. Engineered porosity via tape casting, lamination and the percolation of pyrolyzable particulates. J Am Ceram Soc 1999;82(7):1693-1701.

[44] Sanson A, Pinasco P, Roncari E. Influence of pore formers on slurry composition and microstructure of tape cast supporting anodes for SOFCs. J Eur Ceramic Soc 2008;28(6):1221-1226.

[45] Zaghib K, Song X, Guerfi A, Rioux R, Kinoshita K. Purification process of natural graphite as anode for Li-ion batteries: chemical versus thermal. J Power Sources 2003;119-121(1):8-15.

[46] Hupp TR, Lewis IC, Criscione JM, Reddy RL, Fulgenzi CF, Page DJ, Fisher FF, Dzermajko AJ, Hedge JB. Graphite, artificial. In: Kirk-Othmer Encyclopedia of chemical technology, Vol.12, New York: John Wiley & Sons, Inc.; 2003 (Online Version), pp. 713-771.

[47] Ruiz-Morales JC, Canales-Vázquez J, Peña Martínez J, Marrero-López D, Irvine JTS, Núñez P. Microstructural optimisation of materials for SOFC applications using PMMA microspheres. J Mater Chem 2006;16(6):540–542.

[48] Funahashi Y, Shimamori T, Suzuki T, Fujishiro Y, Awano M. Fabrication and characterization of components for cube shaped micro tubular SOFC bundle. J Power Sources 2007;163(2):731-736.

[49] Jung SW, Lu C, He HP, Ahn KY, Gorte RJ, Vohs JM. Influence of composition and Cu impregnation method on the performance of Cu/CeO_2/YSZ SOFC anodes. J Power Sources 2006;154(1):42-50.

[50] Fujii S, Minami H, Okubo M. Production of poly(methyl methacrylate) particles by dispersion polymerization with mercaptopropyl terminated poly(dimethylsiloxane) stabilizer in supercritical carbon dioxide. Colloid Polym Sci 2004;282(6):569-574.

[51] Jiang SP, Chan SH. A review of anode materials development in solid oxide fuel cells. J Mater Sci 2004;39(14):4405-4439.

[52] Zhu WZ, Deevi SC. A review on the status of anode materials for solid oxide fuel cells. Mater Sci Eng A 2003;362(1-2):228-239.

[53] Lee JH, Heo JW, Lee DS, Kim J, Kim GH, Lee HW, et al. Solid State Ionics 2003;158(3-4):225-232.

[54] Sarikaya A, Petrovsky V, Dogan F. Effect of microstructural evolution on the electrochemical properties of high performance SOFCs. In: ECS Transactions, The Electrochemical Society, Pennington, 2012 (in press).

[55] Barfod R, Hagen A, Ramousse S, Hendriksen PV, Mogensen M. Break down of losses in thin electrolyte SOFCs. Fuel Cells 2006;6(2):141-145.

[56] Primdahl S, Mogensen M. Oxidation of hydrogen on Ni/yttria-stabilized zirconia cermet anodes. J Electrochem Soc 1997;144(10):3409-3419.

[57] Primdahl S, Mogensen M. Gas diffusion impedance in characterization of solid oxide fuel cell anodes. J Electrochem Soc 1999;146(8):2827-2833.

[58] Lee J-J, Moon H, Park H-G, Yoon D-I, Hyun S-H. Applications of nano-composite materials for improving the performance of anode-supported electrolytes of SOFCs. Int J Hydrogen Energy 2010;35(2):738-744.

[59] Primdahl S, Mogensen M. Gas conversion impedance: A test geometry effect in characterization of solid oxide fuel cell anodes. J Electrochem Soc 1998;145(7):2431-2438.

Figures:

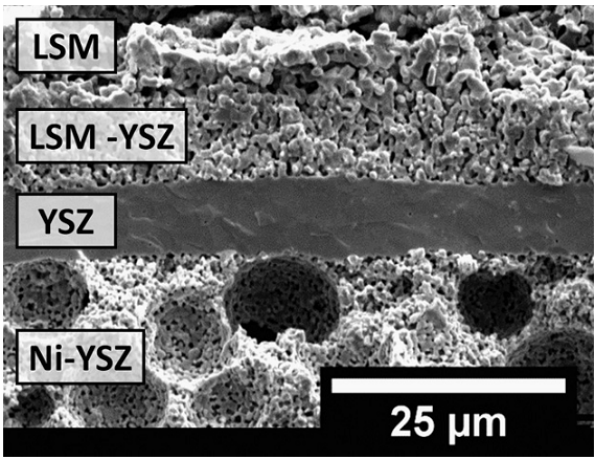

Figure 1. Scanning electron micrograph of the cross sectional fracture surface of an anode supported planar SOFC.

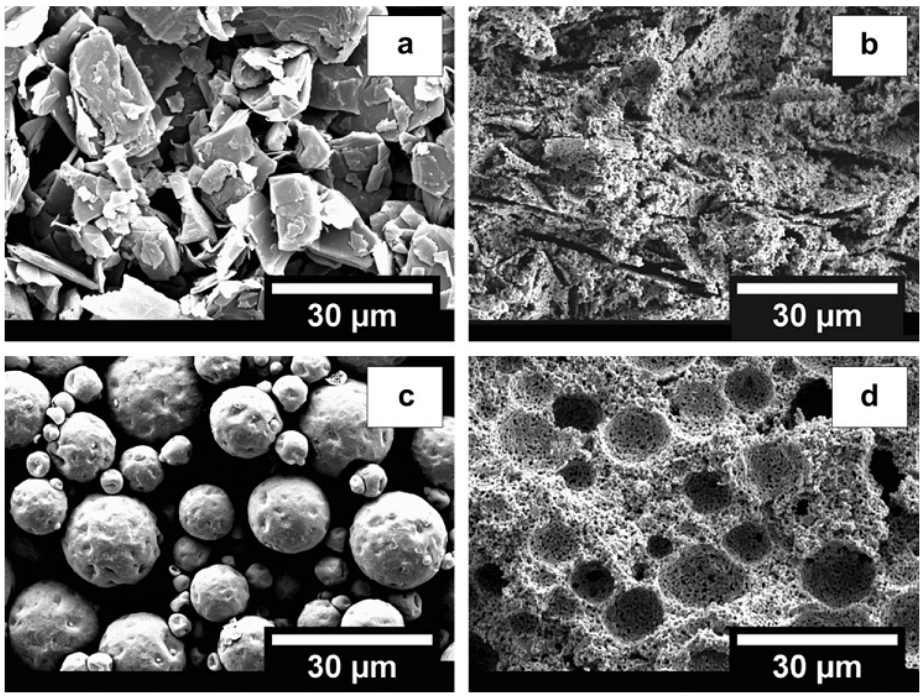

Figure 2. Scanning electron micrographs of the flake graphite (a) and PMMA (c) particles and the sintered porous anode microstructures of cell A (b) and cell B (d) they formed upon reduction, respectively.

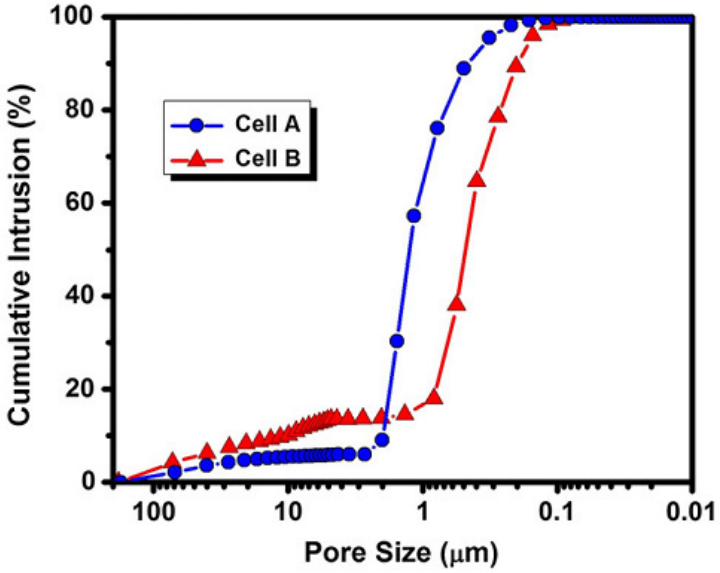

Figure 3. Cumulative intruded volume of Hg as a function of pore size in reduced anodes of the cell A and the cell B.

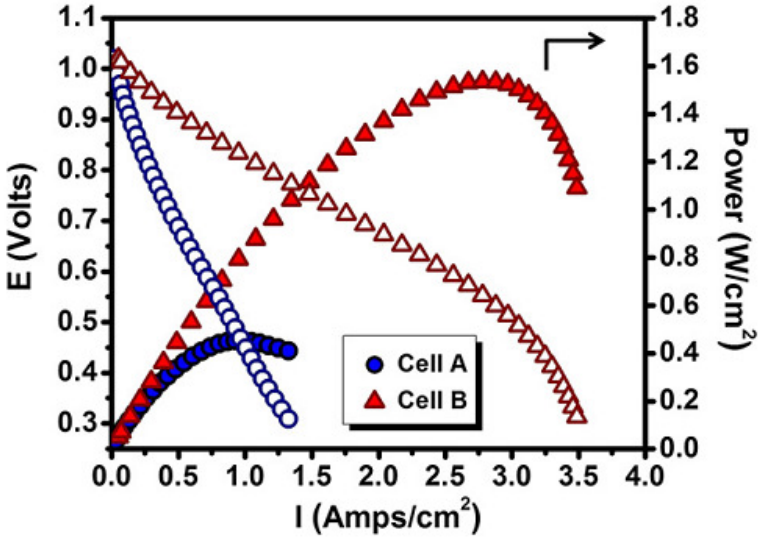

Figure 4. Voltage and power density of the cell A and the cell B as functions of current density at 800^{o}C.

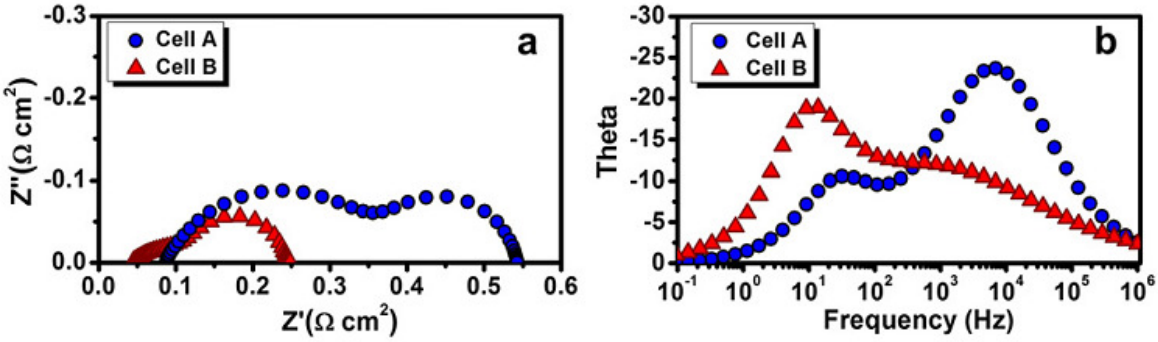

Figure 5. Cole-Cole (a) and Bode (b) plots calculated from the impedance spectra of the cell A and the cell B measured at 0.5V and 800^{o}C.

Tables:

Table 1. Compositions of the green anode tapes.

Cell	Pore Former	YSZ		NiO		Dispersant		Binder		Plasticizer		Pore Former	
	Type	wt%	vol%	wt%	vol%	wt%	vol%	wt%	vol%	wt%	vol%	wt%	vol%
Cell A	Flake Graphite	23.4	11.4	40.2	17	0.3	0.7	11	29.5	5.5	15.9	19.6	25.3
Cell B	PMMA	27.4	11.4	47	17	0.3	0.7	12.8	29.5	6.4	15.9	6.1	25.3

APPENDIX C

ANALYSIS OF THE HIGH TEMPERATURE STABILITY OF SILVER BASED POROUS COMPOSITES

ANALYSIS OF THE HIGH TEMPERATURE STABILITY OF SILVER BASED POROUS COMPOSITES

1. Introduction

Ag based composites have been highly attractive materials for current collection (i.e. electrical contact) applications in electronic devices due to their substantial electrical conductivity. Ag has the highest electrical conductivity among metals and it introduces its superior properties to it composites. These properties include oxygen conductivity, ductility and lightweight with respect to other non-oxidizing metal options (e.g. Pt, Ag and Pd). However, the use of Ag is limited at elevated temperatures (<550^{o}C) due to its relatively low melting point (962^{o}C). Thus, the use of Ag is restricted in high temperature electrical applications such as solid oxide fuel cells and oxygen sensors.

Recently, it was reported that the stability of porous Ag composites can be improved by addition of oxide particles and also by infiltration of nanostructured oxide layers. This study aims a further understanding of the stabilization mechanisms retarding the densification of porous Ag matrix and also limiting coarsening of its particles. Powder based mixtures various particle size ratios were investigated at a composition (20 vol % YSZ : 80 vol% Ag) near the previously identified percolation threshold (25 vol% YSZ : 75 vol% Ag) of the Ag particles. The investigations were extended to nanostructured coatings of the same compositions (Ag-YSZ) at elevated temperatures (i.e. 900^{o}C) and detailed analysis of the Ag-YSZ interfaces for possible formation of phases and diffusion of Ag under operating polarization conditions.

2. Experimental

Powder based mixtures of Ag with various sizes of yttria-stabilized zirconia (YSZ) particles were prepared with identical amounts of a polymeric vehicle for screen-printing. Electrodes of the desired compositions were applied on YSZ electrolytes in symmetrical configuration to investigate the microstructural changes using the previously developed electrochemical analysis method based on electrochemical impedance spectroscopy.

The study was extended to the infiltration of the identical YSZ nanostructured coatings into the porous Ag matrices (pure Ag and Ag-YSZ) to investigate the effects of the nanostructured oxides on the microstructural stability and electrochemical properties at temperatures up to 900^{o}C in air.

Further characterization of the microstructures was performed using transmission electron microscopy techniques. Electrodes under various polarization resistances and current flows were also investigated on identical samples to determine the possible diffusion of Ag through grain or grain boundary of the YSZ electrolyte. Detailed analyses were performed on the interfaces of samples prepared by focused ion-beam lift-out method.

3. Results and discussion

As it is shown in Figure 1, the characteristic relaxation frequency of the polarization arc shifted through lower frequencies with time and the polarization resistance increased significantly with the Ag composites incorporated with nano size (d_{50} = 25 nm) and coarse (d_{50} = 2 μm) YSZ particles at the same volumetric solid loading (20 vol% YSZ –

80 vol% Ag). On the other hand, the same Ag configuration with the intermediate size (d_{50} = 0.3 μm) YSZ particles did not demonstrate a considerable shift. Its polarization resistance increased from 0.175 Ohm cm^2 to 0.275 Ohm cm^2 while the other compositions exhibited colossal change, several degrees of order higher polarization resistances due to microstructural degradation at 800^oC. Moreover, the expected resistance of the electrolyte (0.25 Ohm cm^2) could not be achieved with the Ag based composites with nano size and coarse YSZ particles. The measured ohmic resistances (the high frequency x-axis intercept of the Cole-Cole plots) were 0.6 Ohm cm^2 and 0.574 Ohm cm^2 for Ag- nano YSZ and Ag- coarse YSZ, respectively. It suggests that the degradation in their microstructures also affected their contact behavior adversely while the expected ohmic resistance 0.25 Ohm cm^2 was measured with the Ag-intermediate YSZ composite electrode. It suggests that the stable microstructure of the Ag-intermediate YSZ composite maintained the stable contact at the Ag-YSZ interface.

The change in the microstructure of the Ag-YSZ composites was clearly seen as an exaggerated coarsening as shown in Figure 2. Although all different sizes of YSZ particles limited the densification of the Ag matrix at the measurement temperature for extended time, nano size YSZ and coarse YSZ could not retard the coarsening of Ag particles.

Even though this composite configuration does not fit to the conventional percolation theories due to the kinetic component, coarsening and densifying Ag, the initial packing and coordination were calculated to model the initial dispersion of the constituent particles. As a result it was predicted that ~ 2000 nano size YSZ particles cover each Ag particle (d_{50} = 0.5 μm) while 250 Ag particles (d_{50} = 0.5 μm) cover each coarse YSZ

particle (d_{50} = 2 μm). As a result, the coarse YSZ could not eliminate the initial grain growth of the Ag particles as seen in Figure 2. Although coverage by nano-size YSZ particles would be expected to limit both densification and coarsening, the percolation of the Ag particles at this loading led to the coarsening due to the non-uniform particle size distribution of the Ag particles. While most of the Ag particles were encapsulated with nano-size YSZ particles, the larger Ag particles resulted in coarsening by merging the adjacent smaller Ag particles as seen in Figure 2. In the case of intermediate size YSZ particles (d_{50} = 0.3 μm), the ratio of the number of YSZ/Ag particles was close to unity (~1.15). Thus, the Ag particles at the threshold of their percolation were in 1 to 1 interaction with YSZ particles at a similar size. It yielded the highest stability achieved with powder based Ag composites during this investigation.

Electrodes based on partially sintered Ag and the powder based mixture of the same Ag particles with 20 vol% YSZ particles were infiltrated with a polymeric YSZ precursor to investigate the effect of the nanostructured YSZ coatings on the high temperature stability of Ag based composites. As it is shown in Figure 3 the electrodes without initial YSZ particles dispersed in the Ag matrix could not be stabilized while the YSZ infiltrated powder based Ag-YSZ composite reached a stable microstructure after 500 h at 900^{o}C. It suggests that the incorporation of initial YSZ particles improve the stability of the composites based on infiltration of oxide layers.

The analyses of the impedance spectra demonstrated that there was a significant improvement in the polarization resistance in the course of the first 10 hours. However, polarization arcs with relatively low characteristic frequencies arose with the partially sintered Ag as shown in Figure 4. It suggests that the composite layer was not stable

although it was encapsulated by a nanostructured YSZ layer and densification took place. It yielded concentration polarization at low frequencies as it retards the transport of air through closing pores.

Ex-situ analysis of the measured YSZ infiltrated partially sintered Ag electrodes indicated that the higher amounts of YSZ infiltration improved the stability of the Ag matrix as shown in Figure 5. However, it was not sufficient to stop the movement of the Ag particles at 900^{o}C which is relatively close to their melting temperature (962^{o}C).

On the other hand, the stability of the powder based Ag-20 vol% YSZ infiltrated with the same amount of YSZ (60x) demonstrated impressive stability as it preserved its initial microstructure after measurements at 900^{o}C for 1 month as shown in Figure 6. A higher magnification analysis of the final microstructure showed that the infiltrated nanostructured YSZ coating was not damaged and maintained its continuous coverage (Figure 7) while it was cracked in the partially sintered Ag based electrodes (Figure 5). It demonstrated that the combination of powder based initial Ag-YSZ composites with infiltration of nanostructured YSZ coatings may allow microstructural and electrochemical stability of Ag based electrodes at temperatures as high as 900^{o}C.

Another major concern in the high temperature electrical applications of Ag based composites has been the diffusion and/or electromigration of Ag through insulating oxide substrates. Since an electrical short would be catastrophic for the operation of solid oxide fuel cells, the diffusion of Ag through the YSZ microstructure was investigated. Identical powder based Ag- 20vol% YSZ samples were prepared an treated with anodic and cathodic polarizations (100 mV), as well as current flow (1 Amp/cm^{2}) at 800^{o}C for 1

month in air. The specimens of electrolyte-electrode interfaces of each configuration were prepared by focused ion-beam lift out technique as shown in Figure 8.

The investigations on the electrochemically treated samples demonstrated that the Ag did not diffuse into the YSZ substrate as no Ag was detected in the grains or at the grain boundaries. Moreover, no phase formation was detected at the Ag-YSZ interface. An example of the TEM analyses is shown in Figure 9 for Ag- 20 vol% YSZ after cathodic treatments.

4. Conclusions

A strong correlation was observed between the stability of the power based Ag-YSZ composites and the size ratio of the component particles. The ratio obtained for intermediate size YSZ particles incorporated to the standard Ag allowed significant improvement in the microstructural stability and electrochemical performance of the Ag-YSZ composites.

The addition of the infiltrated nanostructured YSZ coatings on the partially sintered Ag and Ag-YSZ composite led to increasing the possible operating temperatures of the Ag based composites. Although partially sintered pure Ag exhibited a continuous degradation trend, the results are encouraging by means of improving the stability of a low temperature metal, Ag, with coatings of nanostructured oxides.

The stability achieved with the combination of nanostructured YSZ coating with the powder based Ag-YSZ composite layers suggest that the Ag based composites can be employed for solid oxide fuel cell applications as a combined cathode and current collector layer at 900^{o}C.

The results of the diffusion analysis at the Ag-YSZ interface of developed Ag-YSZ composites under different electrical conditions allowed a further fundamental insight. Investigations on the high temperature interactions of the constituent phases demonstrated that the diffusion of Ag through the surface, YSZ grain boundary and grain does not take place under the given experimental conditions. Although further studies are required, the initial findings deserve their novelty as the known practical operating conditions of Ag based composites were extended and the temperature limitations were elevated near their melting temperature.

Figures:

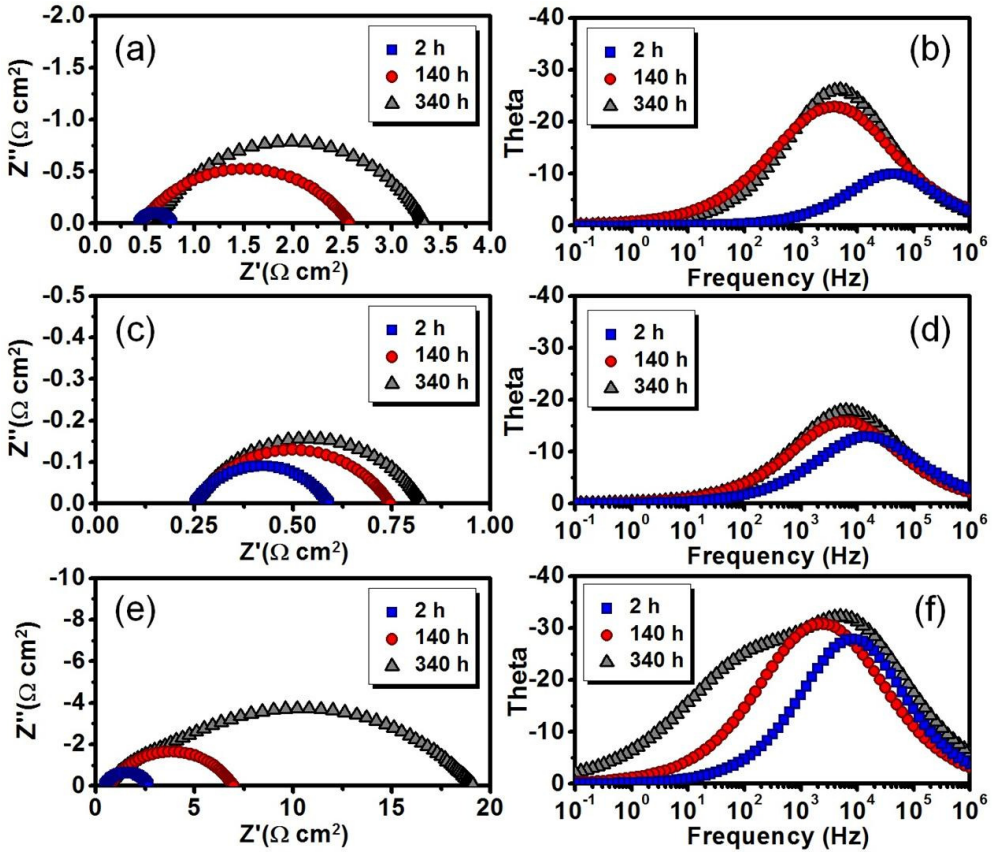

Figure 1. Cole-cole (a, c, e) and bode plots (b, d, f) calculated using the measured impedance spectra of powder based Ag-YSZ composite electrodes at 800^{o}C in air. Initial Ag particle size (0.5 µm) was identical with all composite electrodes and YSZ particle size was varied from 25 nm (a, b), to 0.3 µm (c, d) and 2 µm (e, f).

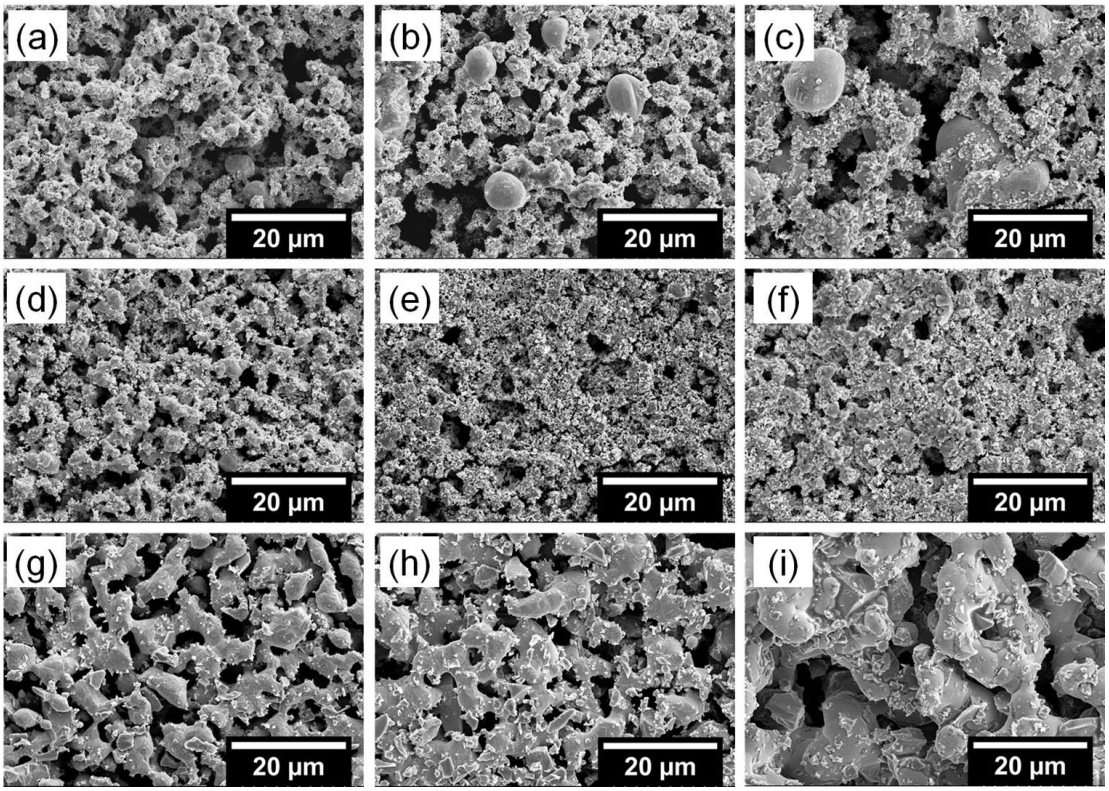

Figure 2. Scanning electron micrographs of the Ag-YSZ composites after measurements at 800^{o}C for various durations (a, d, g were captured after 2 hours, b, e, h were captured after 140 hours and c, f, i were captured after 340 hours). Note that a, b, c are the microstructures of Ag with nano size YSZ after measurements; d, e, f are the microstructures of Ag with intermediate size YSZ; g, h, i are with coarse YSZ at the same (20 vol%) loading.

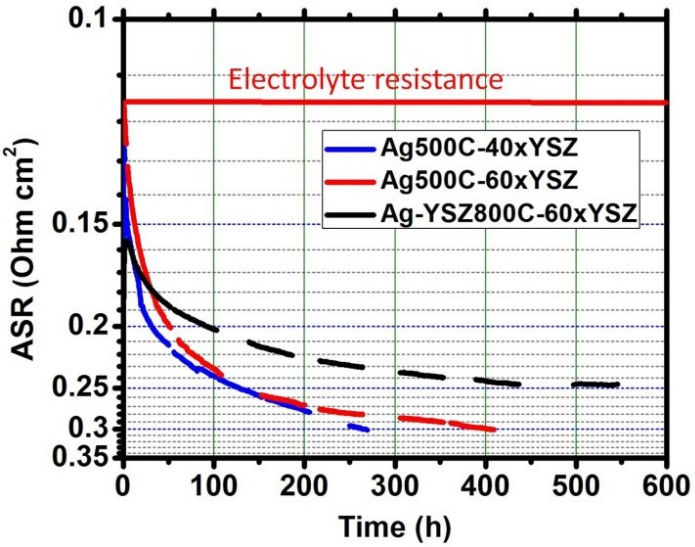

Figure 3. Comparison of the change in the electrochemical polarization resistances of YSZ infiltrated partially sintered Ag and powder based porous Ag-YSZ composites at 900^{o}C.

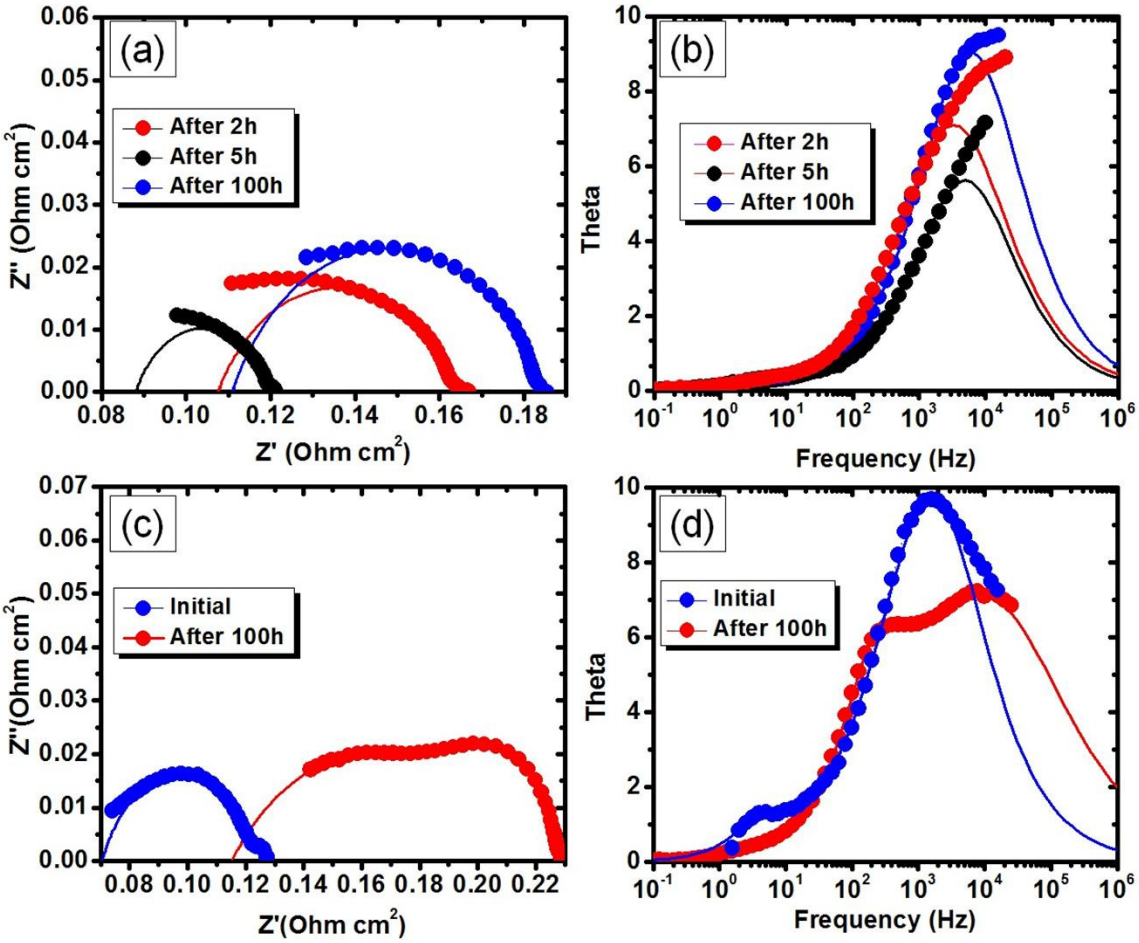

Figure 4. Comparison of the change of the Cole-Cole (a, c) and Bode plots (b, d) of YSZ infiltrated partially sintered Ag and powder based porous Ag-YSZ composites at 900^{o}C. Note that a and b were measured with YSZ infiltrated powder based Ag-YSZ electrode while c and d were measured with 60 times YSZ infiltrated partially sintered Ag.

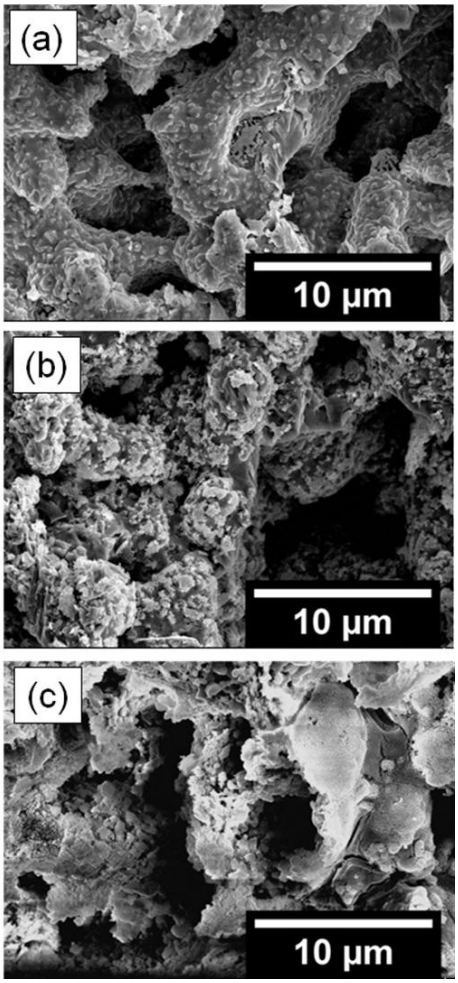

Figure 5. Comparison of partially sintered porous Ag electrodes infiltrated with YSZ for 40 (a), 60 (b) and 80 times (c). The images were captured on electrodes after measurements at 900^{o}C for 1 month.

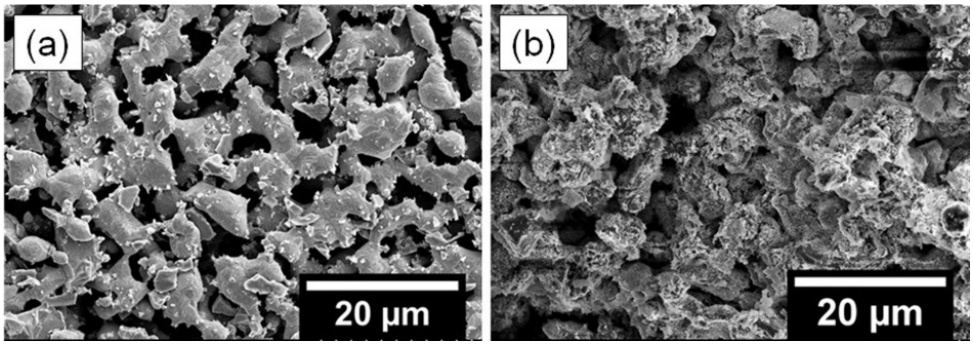

Figure 6. Microstructure of YSZ infiltrated powder based Ag-20 vol% YSZ electrode after measurements for 2 hours (a) and 1 month (b) at 900^{o}C in air.

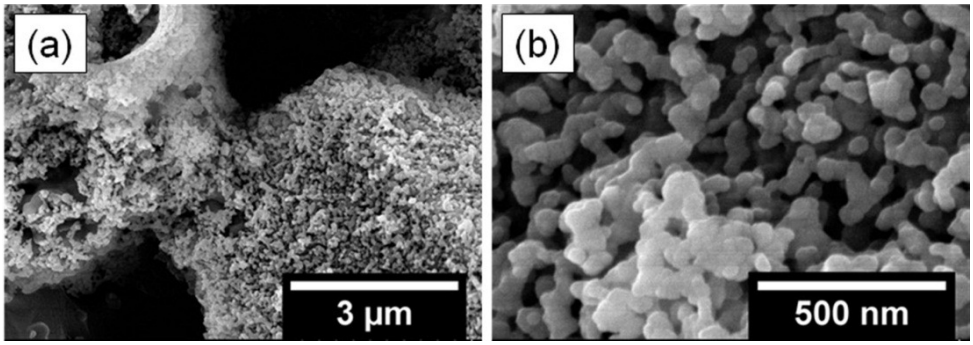

Figure 7. Microstructure of the continuous nanostructured YSZ coverage on the inner surface of porous powder based Ag-YSZ electrode after measurements at 900^{o}C for 1 month.

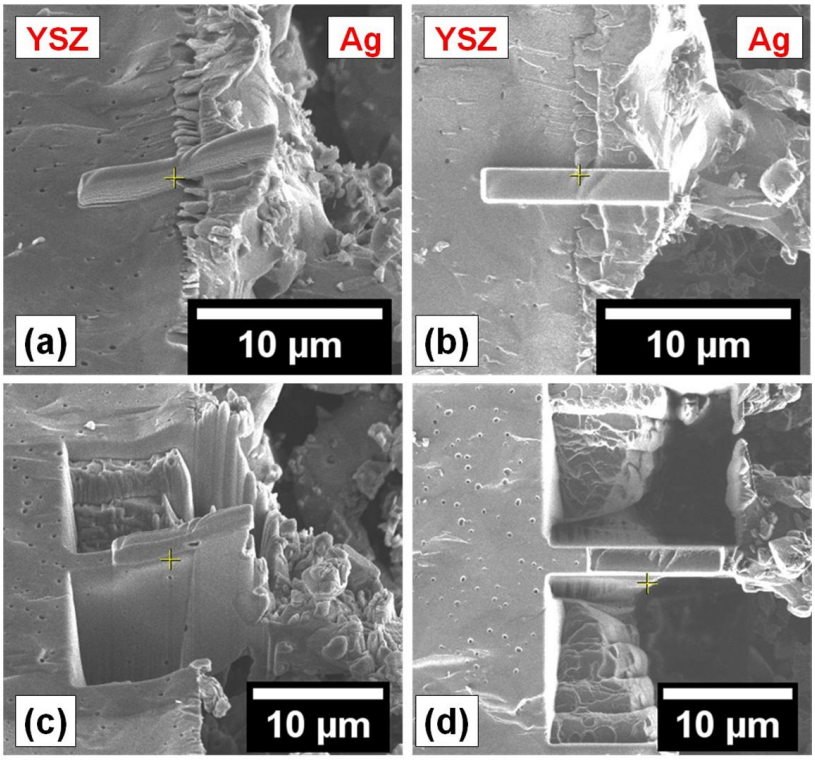

Figure 8. Trenching of the Ag-YSZ interface using focused ion-beam technique for TEM sample preparation. Images in a and b are different perspectives of the determined area for trenching. Images in c and d are different perspectives of the same area after trenching prior to lift-out of the TEM specimen.

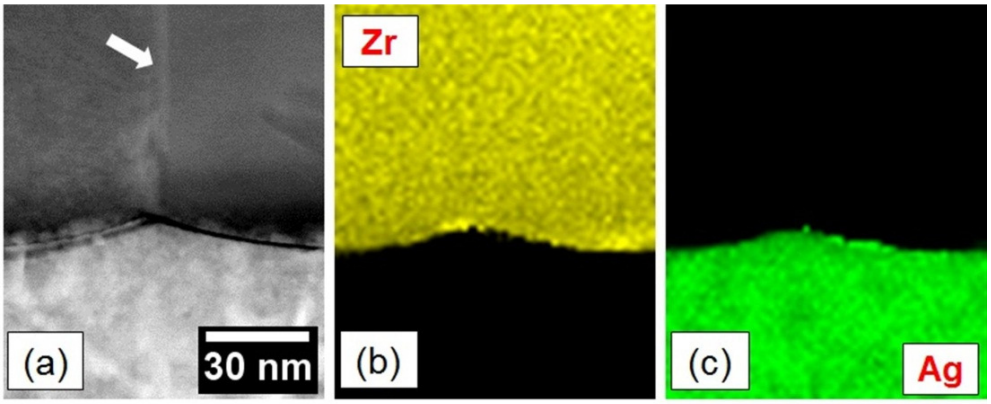

Figure 9. Compositional analysis of the Ag electrode – YSZ electrolyte interface with TEM-EDX after treatments with cathodic polarization and current flow. Note that the arrow indicates the boundary of the YSZ grains.

REFERENCES

1. E. Riensche, E. Achenbach, D. Froning, M. R. Haines, W. K. Heidug, A. Lokurlu *et al*, "Clean Combined Cycle SOFC Power Plant - Cell Modelling and Process Analysis," *J. Power Sources*, **86** [1–2] 404-410 (2000).

2. M. Santin, A. Traverso, L. Magistri, A. F. Massardo, "Thermoeconomic Analysis of SOFC–GT Hybrid Systems Fed by Liquid Fuels," *Energy*, **35** 1077-1083 (2010).

3. E. D. Wachsman, K. T. Lee, "Lowering the Temperature of Solid Oxide Fuel Cells," *Science*, **334** [6058] 935-939 (2011).

4. A. Atkinson, S. Barnett, R. J. Gorte, J. T. Irvine, A. J. McEvoy, M. Mogensen, *et al*, "Advanced Anodes for High-Temperature Fuel Cells," *Nat. Mater.*, **3** [1] 17-27 (2004).

5. A. L. Dicks, "Advances in Catalysts for Internal Reforming in High Temperature Fuel Cells," *J. Power Sources*, **71** [1–2] 111-122 (1998).

6. G. Pepermans, J. Driesen, D. Haeseldonckx, R. Belmans, W. D'haeseleer, "Distributed Generation: Definition, Benefits and Issues," *Energ. Policy*, **33** [6] 787-798 (2005).

7. C. Stiller, B. Thorud, O. Bolland, R. Kandepu, L. Imsland, "Control Strategy for a Solid Oxide Fuel Cell and Gas Turbine Hybrid System," *J. Power Sources*, **158** [1] 303-315 (2006).

8. M. C. Williams, J. P. Strakey, S. C. Singhal, "U.S. Distributed Generation Fuel Cell Program," *J. Power Sources*, **131** [1-2] 79-85 (2004).

9. J. M. Gordon, M. Huleihil, "General Performance Characteristics of Real Heat Engines," *J. Appl. Phys.*, **72** [3] 829-837 (1992).

10. J. Larminie, A. Dicks, *Fuel Cell Systems Explained*, John Wiley & Sons, Ltd., p. 54 (2000).

11. C. Wang, M. H. Nehrir, "A Physically Based Dynamic Model for Solid, Oxide Fuel Cells," *IEEE Trans. Energy Convers.*, **22** [4] 887 – 897 (2007).

12. A. V. Virkar, J. Chen, C. W. Tanner, J-W. Kim, "The Role of Electrode Microstructure on Activation and Concentration Polarization in Solid Oxide Fuel Cells," *Solid State Ionics*, **131** [1-2] 189-198 (2000).

13. H. Chan, Z. T. Xia, "Polarization Effects in Electrolyte/Electrode-Supported Solid Oxide Fuel Cells," *J. Appl. Electrochem.*, 32 [3] 339-347 (2002).

14. S. H. Chan, K. A. Khor, Z. T. Xia, "A Complete Polarization Model of a Solid Oxide Fuel Cell and Its Sensitivity to the Change of Cell Component Thickness," *J. Power Sources*, **93** [1-2] 130-140 (2001).

15. W. Zhu, D. Ding, C. Xia, "Enhancement in Three-Phase Boundary of SOFC Electrodes by an Ion Impregnation Method: A Modeling Comparison," *Electrochem. Solid-State Lett.*, **11** [6] B83-B86 (2008).

16. D. Beckel, A. Bieberle-Hutter, A. Harvey, A. Infortuna, U. P. Muecke, M. Prestat, J. L. M. Rupp, L. J. Gauckler, "Thin Films for Micro Solid Oxide Fuel Cells," *J. Power Sources*, **173** [1] 325-345 (2007).

17. S. P. S. Badwal, "Zirconia-Based Solid Electrolytes: Microstructure, Stability and Ionic Conductivity," *Solid State Ionics*, **52** [1-3] 23-32 (1992).

18. A. J. McEvoy, "Thin SOFC Electrolytes and Their Interfaces-: A Near-Term Research Strategy," *Solid State Ionics*, **132** [3-4] 159-165 (2000).

19. X. J. Chen, K. A. Khor, S. H. Chan, L. G. Yu, "Influence of Microstructure on the Ionic Conductivity of Yttria-Stabilized Zirconia Electrolyte," *Mater. Sci. Eng. A.*, **335** [1-2] 246-252 (2002).

20. J. Drennan, G. Auchterlonie, "Microstructural Aspects of Oxygen Ion Conduction in Solids," *Solid State Ionics*, **134** [1-2] 75-87 (2000).

21. A. K. Sahu, A. Ghosh and A. K. Suri, "Characterization of Porous Lanthanum Strontium Manganite (LSM) and Development of Yttria Stabilized Zirconia (YSZ) Coating," *Ceram. Int.*, **35** [6] 2493-2497 (2009).

22. J. P. P. Huijsmans, F. P. F. van Berkel, G. M. Christie, "Intermediate Temperature SOFC – A Promise for the 21st Century," *J. Power Sources*, **71** [1-2] 107-110 (1998).

23. O. Yamamoto, "Solid Oxide Fuel Cells: Fundamental Aspects and Prospects," *Electrochim. Acta*, **45** [15-16] 2423-2435 (2000).

24. H. S. Song, W. H. Kim, S. H. Hyun, J. Moon, "Influence of Starting Particulate Materials on Microstructural Evolution and Electrochemical Activity of LSM-YSZ Composite Cathode for SOFC," *J. Electroceramics*,**17** [2-4] 759-764 (2006).

25. Y-K. Lee, J-Y. Kim, Y-K. Lee, I. Kim, H-S. Moon, J-W. Park, C. P. Jacobson, S. J. Visco, "Conditioning Effects on $La_{1-x}Sr_xMnO_3$-Yttria Stabilized Zirconia Electrodes for Thin-Film Solid Oxide Fuel Cells," *J. Power Sources*, **115** [2] 219-228 (2003).

26. M. Mogensen, K. V. Jensen, M. J. Jorgensen, S. Primdahl, "Progress in Understanding SOFC Electrodes," *Solid State Ionics*, **150** [1-2] 123-129 (2002).

27. J. H. Yu, G. W. Park, S. Lee, S. K. Woo, "Microstructural Effects on the Electrical and Mechanical Properties of Ni-YSZ Cermet for SOFC Anode," *J. Power Sources*, **163** [2] 926-932 (2007).

28. S. T. Aruna, M. Muthuraman, K. C. Patil, "Synthesis and Properties of Ni-YSZ Cermet: Anode Material for Solid Oxide Fuel Cells," *Solid State Ionics*, **11** [1-2] 45-51 (1998).

29. T. Tsai, S. A. Barnett, "Effect of LSM-YSZ Cathode on Thin-Electrolyte Solid Oxide Fuel Cell Performance," *Solid State Ionics*, **93** [3-4] 207-217 (1997).

30. M. J. Jorgensen, S. Primdahl, C. Bagger, M. Mogensen, "Effect of Sintering Temperature on Microstructure and Performance of LSM-YSZ Composite Cathodes," *Solid State Ionics*, **139** [1-2] 1-11 (2001).

31. S-H. Lee, G. L. Messing, M. Awano, "Sintering Arches for Cosintering Camber-Free SOFC Multilayers," *J. Am. Ceram. Soc.*, **91** [2] 421-427 (2008).

32. W. Li, K. Hasinska, M. Seabaugh, S. Swartz, J. Lannutti, "Curvature in Solid Oxide Fuel Cells," *J. Power Sources*, **138** [1-2] 145-155 (2004).

33. M. J. Jorgensen, S. Primdahl, M. Mogensen, "Characterization of Composite SOFC Cathodes Using Electrochemical Impedance Spectroscopy," *Electrochim. Acta,* **44** [24] 4195-4201 (1999).

34. P. Holtappels, C. Bagger, "Fabrication and Performance of Advanced Multi-layer SOFC Cathodes," *J. Eur. Ceram. Soc.*, **22** [1] 41-48 (2002).

35. K. Sasaki, J-P. Wurth, R. Gschwend, M. Godickemeier, L. J. Gauckler, "Microstructure-Property Relations of Solid Oxide Fuel Cell Cathodes and Current Collectors: Cathodic Polarization and Ohmic Resistance," *J. Electrochem. Soc.*, **143** [2] 530-543 (1996).

36. S. P. Simner, M. D. Anderson, L. R. Pederson, J. W. Stevenson, "Performance Variability of La(Sr)O_3 SOFC Cathode with Pt, Ag, and Au Current Collectors," *J. Electrochem. Soc.*, **152** [9] A1851-A1859 (2005).

37. Z. Yang, G. Xia, P. Singh, J. W. Stevenson, "Electrical Contacts Between Cathodes and Metallic Interconnects in Solid Oxide Fuel Cells," *J. Power Sources*, **155** [2] 246-252 (2006).

38. S. P. Simner, M. D. Anderson, J. E. Coleman, J. W. Stevenson, "Performance of a Novel La(Sr)Fe(Co)O_3-Ag SOFC Cathode," *J. Power Sources*, **161** [1] 115-122 (2006).

39. L. T. Wilkinson, J. H. Zhu, "Ag-Perovskite Composite Materials for SOFC Cathode-Interconnect Contact," *J. Electrochem. Soc.*, **156** [8] B905-B912 (2009).

40. W. Z. Zhu, S. C. Deevi, "Development of Interconnect Materials for Solid Oxide Fuel Cells," *Mater. Sci. Eng., A*, **348** [1-2] 227-243 (2003).

41. H. Yokokawa, T. Horita, N. Sakai, K. Yamaji, M. E. Brito, Y-P. Xiong, H. Kishimoto, "Thermodynamic Considerations on Cr Poisoning in SOFC Cathodes," *Solid State Ionics*, **177** [35-36] 3193-3198 (2006).

42. S. C. Paulson, V. I. Birss, "Chromium Poisoning of LSM-YSZ SOFC Cathodes: 1. Detailed Study of the Distribution of Chromium Species at a Porous, Single-Phase Cathode," *J. Electrochem. Soc.*, **151** [11] A1961-A1968 (2004).

43. M. Camaratta, E. Wachsman, "Silver-Bismuth Oxide Cathodes for IT-SOFCs; Part 1-Microstructural Instability," *Solid State Ionics*, **178** [19-20] 1242-1247 (2007).

VITA

Ayhan Sarikaya was born on December 3, 1984 in Yozgat, Turkey. He received his Bachelor of Science Degree in Metallurgical and Materials Engineering from Istanbul Technical University in Spring 2008 after several co-ops and internships at international industrial companies and research institutes including CERN in Geneva, Switzerland and Helmholtz Zentrum-Berlin, Berlin, Germany. Right after the graduation he started pursuing his Ph.D. in Fall 2008 under the supervision of Dr. Fatih Dogan in Missouri University of Science and Technology (formely University of Missouri – Rolla) in Rolla, Missouri, U.S.A. His doctoral work was focused on the analysis of the microstructure – electrochemical performance relationships in solid oxide fuel cells.